

STRUCTURE AND PROPERTIES OF TI-NI-AU
SHAPE MEMORY ALLOYS

by

TODD BUTLER

MARK L. WEAVER, COMMITTEE CHAIR
GREGORY B. THOMPSON
YUEBIN GUO

A THESIS

Submitted in partial fulfillment of the requirements for the degree of
Master of Science in the Department of Metallurgical and
Materials Engineering in the Graduate School of
The University of Alabama

TUSCALOOSA, ALABAMA

2013

Copyright Todd Micheal Butler 2013
ALL RIGHTS RESERVED

ABSTRACT

Ternary Ti-Ni-X based alloys, where X = Pt, Pd, Hf, Au or Zr, show promise as high temperature shape memory alloys (HTSMAs). In comparison to binary Ni-Ti alloys, some hypo-stoichiometric versions of these ternary compositions exhibit higher transformation temperatures and better mechanical stability due to the formation of nano-scale precipitates. In this study, a $\text{Ti}_{49}\text{Ni}_{26}\text{Au}_{25}$ (at.%) alloy was solution annealed at 1050°C for 3 hours and isothermally aged at 400°C and 550°C . A specimen was also annealed at 1050°C for 3 hours and furnace cooled. Ageing resulted in a very high peak micro-hardness for both temperatures. The structures and chemistries of the phases formed during ageing were characterized by wavelength dispersive x-ray spectroscopy (WDS), scanning electron microscopy (SEM), energy dispersive x-ray spectroscopy (EDS), transmission electron microscopy (TEM), three-dimensional atom probe tomography (3DAP), x-ray diffraction (XRD), and differential scanning calorimetry (DSC). It was found that ageing at both 400°C and 550°C resulted in the formation of two different precipitates. First, two variants of a $(\text{Au,Ni})_4\text{Ti}_3$ type phase form with SADPs similar to tetragonal $D1_a$. The proposed orientation relationships with the matrix are the following: $[001]_{D1a} \parallel [100]_{B2}$ with $(011)_{B2} \parallel (310)_{D1a}$ and $[00\bar{1}]_{D1a} \parallel [100]_{B2}$ with $\{011\}_{B2} \parallel (310)_{D1a}$. It is then postulated that the (Au,Ni)-rich phase creates local Ti-rich regions that promote the precipitation of two $\text{Ti}_2(\text{Ni,Au})$ variants with tetragonal ($I4/mmm$) type symmetry. Their proposed orientation relationships with the matrix are the following: $[100]_{\text{Ti}_2(\text{Ni,Au})} \parallel [100]_{B2}$ with $(001)_{B2} \parallel (001)_{\text{Ti}_2(\text{Ni,Au})}$ and $(001)_{B2} \parallel (100)_{\text{Ti}_2(\text{Ni,Au})}$. The combination of both phases appears to inhibit martensitic transformation by stabilizing the high temperature austenite phase, as evident

by no transformation peaks in the aged specimens via DSC. However, it is interesting to note that the as-cast and 1050°C furnace cooled specimens did exhibit martensitic transformation with M_s values of approximately 135° and 160°C, respectively. Such behavior is thought to be attributed to their microstructure, which both appeared to consist mainly of $(\text{Au,Ni})_4\text{Ti}_3$ platelets, as evident via SEM. This ultimately increases the Ti concentration in the matrix and raises the transformation temperatures.

Two precipitate buttons with target compositions (at %) of 66.00 Ti – 3.50 Ni – 30.50 Au ($\text{Ti}_2(\text{Ni,Au})$) and 41.70 Ti – 27.40 Ni – 30.90 Au ($(\text{Au,Ni})_4\text{Ti}_3$) were also heat treated at 550°C for 96 hours. The structures and chemistries of the phases formed during ageing were characterized by scanning electron microscopy (SEM), energy dispersive x-ray spectroscopy (EDS), and x-ray diffraction (XRD). It was found that the as-cast Ti-rich button consisted of a Ti_3Au phase and a Ti-Ni-Au B2 phase with small Ti-rich platelets, as evident via SEM. Ageing at 550°C for 96 hours promoted precipitate growth in the B2 regions. The crystallography of the additional Ti-rich platelets was found to fit well with $I4/mmm$ symmetry, as evident via XRD. The as-cast (Au,Ni)-rich button consisted of a Au_2Ti phase and a Ti-Ni-Au B2 phase with additional (Au,Ni)-rich platelets, as evident via SEM. Ageing at 550°C for 96 hours promoted the growth of the (Au,Ni)-rich platelets. The crystallography of the (Au,Ni)-rich platelets appeared to fit well with the proposed peak locations for $(\text{Au,Ni})_4\text{Ti}_3$, as evident via XRD.

LIST OF ABBREVIATIONS AND SYMBOLS

Abbreviations:

3DAP	Three dimensional atom probe tomography
A _s	Austenite start temperature
A _f	Austenite finish temperature
at %	Atomic percent
BF	Bright Field
BSE	Backscattered Electron
DSC	Differential scanning calorimetry
EDS	Energy dispersive spectroscopy
EPMA	Electron Microprobe
FIB	Focused ion beam
HAADF	High angle annular dark field
HTSMA	High temperature shape memory alloy
M _s	Martensite start temperature
M _f	Martensite finish temperature
SADP	Selected Area Diffraction Pattern
SEM	Scanning electron microscopy
SMA	Shape memory alloy
STEM	Scanning Transmission Electron Microscopy
TEM	Transmission Electron Microscopy

WDS Wavelength Dispersive Spectroscopy

wt % Weight percent

XRD X-ray diffraction

Symbols:

Au25	Ti ₄₉ Ni ₂₆ Au ₂₅ Alloy designation
Au 4:3	(Au,Ni) ₄ Ti ₃ designation
B2	Ti-Ni-Au Austenite Parent Phase (Ordered CsCl Structure)
D1 _a	Tetragonal structure (I 4/m)
Ti 2:1	Ti ₂ (Ni,Au) designation

ACKNOWLEDGEMENTS

I would like to thank my advisor Dr. Mark L. Weaver, for his consistent aid and instruction throughout the course of this project. I would also like to thank Ron Noebe and Glenn Bigelow for synthesizing this alloy at the NASA Glenn Research Center. I also appreciate the valuable input from my committee members Dr. Yuebin Guo and Dr. Gregory B. Thompson.

Thanks to Johnny Goodwin, Rich Martens, and Robert Holler for their assistance with instrument operation in the Central Analytical Facility (CAF). Without their help, this project would not have been possible. I would also like to thank my fellow classmates, as their valuable discussions shaped this project in many ways. Also, this thesis would not have been possible without the love and support of my family and friends.

CONTENTS

ABSTRACT.....	ii
LIST OF ABBREVIATIONS AND SYMBOLS	iv
<i>Abbreviations:</i>	vi
<i>Symbols:</i>	vi
ACKNOWLEDGEMENTS.....	vii
CONTENTS.....	viii
LIST OF TABLES	xi
LIST OF FIGURES	xii
CHAPTER 1: INTRODUCTION	1
CHAPTER 2: REVIEW OF SHAPE MEMORY ALLOYS.....	2
2.1 <i>The Shape Memory Effect and Superelasticity</i>	2
2.2 <i>Ni-Ti-based SMAs</i>	5
2.3 <i>Ni-Ti-based HTSMAs</i>	7
2.3.1 <i>Ni-Ti-Au HTSMAs</i>	8
CHAPTER 3: EXPERIMENTAL METHODS	10
3.1 <i>EPMA-WDS</i>	10
3.2 <i>Heat Treatments</i>	11
3.3 <i>Vickers Microhardness</i>	12
3.4 <i>Scanning Electron Microscopy - EDS</i>	12
3.5 <i>Transmission Electron Microscopy</i>	12

3.6 X-ray Diffraction.....	14
3.7 3D Atom Probe Tomography.....	14
3.8 Differential Scanning Calorimetry	15
CHAPTER 4: CHARACTERIZATION OF AU25 ALLOY	16
4.1 As-Cast Microstructure.....	16
4.2 1050°C Annealed Microstructure.....	18
4.3 400°C and 550°C Heat Treated Microstructure and Properties.....	20
4.3.1 Vickers Hardness Ageing Curves.....	21
4.3.2 Microstructures as Evident in SEM.....	22
4.3.3 Microstructures as Evident in TEM.....	25
4.3.4 Atom Probe Tomography Results	35
4.3.5 XRD Results	45
4.3.6 DSC Results	48
4.4 1050°C Furnace Cooled Microstructure and Properties.....	50
CHAPTER 5: CHARACTERIZATION OF TI 2:1 AND AU 4:3 ALLOYS	55
5.1 Ti 2:1 Alloy	55
5.2 Au 4:3 Alloy	59
CHAPTER 6: DISCUSSION	64
6.1 Au25 Alloy.....	64
6.1.1 Ti ₂ (Ni,Au) Phase	64
6.1.2 (Au,Ni) ₄ Ti ₃ Phase	67
6.1.3 Proposed Precipitation Mechanism.....	71
6.1.4 Transformation Behavior and Hardness	73

<i>6.2 Ti 2:1 Alloy</i>	75
<i>6.3 Au 4:3 Alloy</i>	75
CHAPTER 7: CONCLUSIONS AND FUTURE WORK.....	79
REFERENCES	84
APPENDIX.....	88

LIST OF TABLES

Table 4-1	EMP-WDS Point Scans of Au25 As-Cast Specimens.....	16
Table 4-2	TEM-EDS Composition Values for Bright (BS) and Dark (DS) Precipitates	32
Table 4-3	Average 3DAP and EMP-WDS Bulk Au25 Compositions for 1050°C/3hrs sample.	36
Table 4-4	Average 3DAP and EMP-WDS Bulk Au25 Compositions 400°C/48hrs.	37
Table 4-5	Average Precipitate and Matrix Compositions from a 400°C/48hrs Reconstruction Centered of a 46.30 at % Ti Iso-surface	38
Table 4-6	Average Precipitate and Matrix Composition from a 400°C/48hrs Reconstruction Centered on a 23.25 at % Ni Iso-surface.	40
Table 4-7	Average 3DAP and EMP-WDS Bulk Au25 Compositions for 400°C/168hrs	43
Table 4-8	Average Precipitate and Matrix Composition from a 400°C/48hrs Reconstruction Centered on a 46.30 at % Ti Iso-surface.....	44
Table 4-9	Average Precipitate and Matrix Composition from a 400°C/168hrs Reconstruction Centered on a 24.30 at % Ni Iso-surface.	44
Table 5-1	Average SEM-EDS and Target Compositions of Ti 2:1 Alloy.....	55
Table 5-2	Average SEM-EDS and Target Compositions of Au 4:3 Alloy.....	60

LIST OF FIGURES

Figure 2-1	Simplistic view of martensitic transformation showing austenite to martensite and the reverse transformation. Adapted from reference [16].....	3
Figure 2-2	Schematic of martensitic transformation with temperatures of interest (A) and corresponding free energy schematic of martensitic transformation (B). Adapted from references [5,16].....	4
Figure 2-3	Diagram of the shape memory effect (SME) and superelasticity (SE) dependent on stress and temperature. Adapted from reference [16].....	5
Figure 2-4	Binary Ti-Ni Phase Diagram. Adapted from reference [4].....	6
Figure 2-5	Three possible transformation paths for Ti-Ni SMAs. Adapted from reference [4].	6
Figure 2-6	Ti-Au binary phase diagram. Adapted from reference [25].....	9
Figure 4-1	Backscattered electron (BSE) images of the Au25 as-cast microstructure in low magnification (A) and high magnification (B)..	17
Figure 4-2	Backscattered electron image of the Au25 1050°C heat treated specimen..	18
Figure 4-3	X-ray diffraction spectra of the Au25 as-cast and solution annealed specimens with B2 peaks identified.	19
Figure 4-4	TEM BF image and SADP taken from the 1050°C/3hrs Au25 sample in the $\langle 011 \rangle_{B2}$ direction (A) and SADPs collected from the $\langle 100 \rangle_{B2}$ direction (B) and $\langle 111 \rangle_{B2}$ direction (C). The labels are the B2 cubic indices..	20
Figure 4-5	Hardness ageing curves for the Au25 solution annealed specimen at 400°C and 550°C.	22
Figure 4-6	BSE images of the Au25 400°C heat treated alloy showing the under-aged (A), peak-aged (B), and over-aged cases (C) and (D).....	23
Figure 4-7	BSE image of the Au25 alloy aged 400°C/1000hrs.	24
Figure 4-8	BSE images of the Au25 550°C heat treated alloy showing the under-aged (A), peak-aged (B), low magnification over-aged (C), and high magnification over-aged (D).....	25

Figure 4-9	TEM BF image and SADP taken from the 400°C/48hrs Au25 sample in the <100> _{B2} direction (A) and SADPs collected from the <110> _{B2} (B) and <111> _{B2} directions (C). The labels are the B2 cubic indices.....	26
Figure 4-10	TEM BF image and inset SADP (A) and higher magnification BF image (B) taken from the 400°C/48hrs Au25 sample down the <115> _{B2} direction..	27
Figure 4-11	TEM BF image (A) and SADP (B) taken from the 400°C/168hrs Au25 foil down the <100> _{B2} direction. The labels in (B) are the B2 cubic indices. The label “P” in (A) indicates platelet.....	28
Figure 4-12	TEM BF image (A) and higher magnification BF image (B) taken from the 400°C/1000hrs Au25 foil down the <100> _{B2} direction. Arrows indicate large platelets (A) and Moire patterns (B).....	29
Figure 4-13	STEM-HAADF image (A) and higher magnification STEM-HAADF image (B) taken from the 400°C/1000hrs Au25 foil just off the <100> _{B2} direction. The label “P” indicates platelet.....	30
Figure 4-14	STEM-HAADF images of 400°C/1000hrs foil (A) and 550°C/96hrs foil (B). The label “P” indicates platelet.....	31
Figure 4-15	STEM-HAADF images of 550°C/96hrs foil with EDS point scan locations labeled. The label “BS” indicates bright spot and “DS” indicates dark spot.....	32
Figure 4-16	STEM-HAADF images of 550°C/192hrs foil showing oblique angle of dark plate. The label “P” indicates platelet.....	33
Figure 4-17	SADPs of 550°C/192hrs foil showing two zones from a dark platelet with their corresponding α and β tilts (A) and (C). The [071] and [-27-1] Ti ₂ Ag (I4/mmm) simulated SADPs are shown in (B) and (D), respectively..	34
Figure 4-18	3DAP reconstruction ion map of 1050°C/3hrs Au25 specimen (A) and SE micrograph of the actual tip geometry with tip-shank fitting emphasized (B).....	36
Figure 4-19	3DAP 24.95 at % Au iso-surface (A) and 26.43 at % Ni iso-surface (B) of the 1050°C Au25 specimen.	37
Figure 4-20	Concentration gradient from 400°C/48hrs 3DAP data reconstruction centered on 46.30 at % Ti. The sides corresponding to precipitate and matrix are labeled.....	38
Figure 4-21	400°C/48hrs 3DAP reconstruction depicting a 29.09 at % Ni precipitate surface (A) and a 24.91 at % Ni Matrix surface (B)..	39
Figure 4-22	Concentration gradient from 400°C/48hrs 3DAP data reconstruction centered on 23.25 at % Ni. The sides corresponding to precipitate and matrix are labeled.....	40

Figure 4-23 400°C/48hrs 3DAP reconstruction depicting a 20.40 at % Ni precipitate surface (A) and polygon filtered image with a large platelet emphasized (B). Arrows signify the two particular platelets discussed in the text.....	41
Figure 4-24 400°C/48hrs 3DAP reconstruction depicting polygon filtered image consisting of a 20.40 at % Ni precipitate surface (A) with alternate side view (B).....	42
Figure 4-25 1-D cylindrical concentration profile through a Ti ₂ (Ni,Au) platelet. Regions of matrix and platelet composition are labeled. The profile is taken normal to the largest surface area of the platelet.....	42
Figure 4-26 Concentration gradient from 400°C/168hrs 3DAP data reconstruction centered on 46.80 at % Ti. The sides corresponding to precipitate and matrix are labeled.....	43
Figure 4-27 400°C/168hrs 3DAP reconstruction depicting a 21.25 at % Ni precipitate surface (A) with 1000 polygon filtered image (B). Arrows indicate two large platelets.....	45
Figure 4-28 XRD spectra of the 400°C heat treated Au25 specimens using Cu-K α radiation. The B2 matrix and Ti ₂ Pd (I4/mmm) peaks are identified.....	46
Figure 4-29 XRD spectra of the 550°C heat treated Au25 specimens using Cu-K α radiation. The B2 matrix and relevant Ti ₂ Pd (I4/mmm) peaks are identified.....	47
Figure 4-30 XRD spectra of the 400°C and 550°C heat treated Au25 specimens using Cu-K α radiation. The peaks thought to be correlated to (Au,Ni) ₄ Ti ₃ are labeled.....	47
Figure 4-31 Several DSC cycles of Au25 as-cast specimen from -90 to 300 °C. T _m and T _A labels represent martensitic transformation temperature and austenitic transformation temperature, respectively.....	48
Figure 4-32 DSC cycles of 400°C peak and over-aged Au25 specimens from -90 to 300 °C..	49
Figure 4-33 DSC cycles of 550°C peak and over-aged Au25 specimens from -90 to 300 °C..	50
Figure 4-34 BSE images of the Au25 1050°C furnace cooled specimen with increasing magnification (A), (B), (C), (D), respectively.....	51
Figure 4-35 XRD spectra of the 1050°C furnace cooled and 550°C peak-aged Au25 specimens using Cu-K α radiation. Labels are indicative of the B2 matrix phase, the Ti ₂ Pd phase (analogous to the proposed Ti ₂ (Ni,Au) type), and peaks thought to be associated with the (Au,Ni) ₄ Ti ₃ phase.....	53
Figure 4-36 Several DSC cycles of Au25 furnace cooled specimen from -90 to 300 °C. T _m and T _A labels represent martensitic transformation temperature and austenitic transformation temperature, respectively.....	54

Figure 5-1 BSE images of the Ti 2:1 as-cast specimen with increasing magnification (A), (B), (C), (D), respectively..	56
Figure 5-2 BSE images of the Ti 2:1 96 hr 550°C specimen with increasing magnification (A), (B), (C), (D), respectively..	57
Figure 5-3 XRD spectra of the as-cast and 550°C/96hr Ti 2:1 specimens using Cu-K α radiation. Labels are indicative of the B2 phase, the Ti ₂ Pd phase (analogous to proposed Ti ₂ (Ni,Au) type), and Ti ₃ Au phase..	59
Figure 5-4 BSE images of the Au 4:3 as-cast specimen with increasing magnification (A), (B), (C), (D), respectively..	61
Figure 5-5 BSE images of the Au 4:3 550°C 96 hr specimen with increasing magnification (A), (B), (C), (D), respectively..	62
Figure 5-6 XRD spectra of the as-cast and 550°C/96hr Au 4:3 specimens using Cu-K α radiation. Labels are indicative of the B2 phase, the Au ₂ Ti phase, and peaks thought to associate with (Au,Ni) ₄ Ti ₃	63
Figure 6-1 TEM bright field of Ti _{51.2} Pd ₂₇ Ni _{21.8} heat treated for 1 hr at 773 K (A) and SADP down the [100] _{B2} direction showing additional Ti ₂ Pd streaking (B). Labels “A” and “B” show two platelet variants. Adapted from reference [45].	64
Figure 6-2 Simulated SADPs with weighted reciprocal lattice for the two Ti ₂ Pd variants [200] _{Ti2Pd} (A) and [020] _{Ti2Pd} (B). The indices in (A) and (B) correlate to Ti ₂ Pd. (C) depicts the two variants stacked atop of a [100] oriented B2 phase, as shown with red spots and weighted reciprocal lattice. The labels in (C) denote cubic B2 indices. Lastly, (D) shows a SADP section from the Au25 400°C 168 hr sample down the <100> _{B2} direction. Arrows in (D) point out streaks between superlattice and main reflections.....	65
Figure 6-3 SADP in Cu-Ti alloy showing two variants of D1 _a structure down [001] _{FCC} with FCC indices (A) and SADP in Au-Ti alloy depicting same two variants of D1 _a structure down [001] _{FCC} with FCC indices (B). Adapted from references [46,47].	67
Figure 6-4 TEM-BF image of Au25 aged 650°C/48hrs oriented down the [100] _{B2} (B) with corresponding SADPs from regions (A), (C), and (D). Indices in (D) represent cubic B2. Indices in (A) and (C) correspond to [001] oriented D1 _a type structure. (C) depicts in red one D1 _a variant oriented [001] _{D1a} . (A) depicts two stacked D1 _a variants. ..	68
Figure 6-5 Simulated SADPs with weighted reciprocal lattice for two D1 _a variants (A) and (B), respectively, with [001] _{D1a} [100] _{B2} . The indices in (A) and (B) correlate to D1 _a structure. (C) depicts the two variants stacked atop of a [100] oriented B2 matrix, as shown with red spots. In (C) both D1 _a variants are labeled. Lastly, (D) shows a SADP from the Au25 400°C/168hrssample down the [100] _{B2} direction. ..	70

Figure 6-6 Simulated SADPs with weighted reciprocal lattice for two D1a variants (Green), two tetragonal I4/mmm variants (open circles), and B2 matrix (Red) (A). The same phases are then stacked on a $\langle 100 \rangle_{B2}$ SADP from the **Au25** 400°C 168hr specimen..... 71

Figure 6-7 Simulated SADPs with weighted reciprocal lattice for two D1a variants, two tetragonal I4/mmm variants, and [110] oriented B2 matrix. The simulations are then compared to a $[110]_{B2}$ SADP from the **Au25** 400°C 168hr specimen. Specific areas of comparison are circled in the simulation and corresponding locations in the experimental SADP. 72

Figure 6-8 Simulated SADPs with weighted reciprocal lattice for two D1a variants, two tetragonal I4/mmm variants, and [111] oriented B2 matrix. The simulations are then compared to a $[111]_{B2}$ SADP from the **Au25** 400°C 168hr specimen. Interestingly, the asymmetry of the two circled pairs of dots is also viewed in the experimental SADP showing asymmetric angular measurements..... 72

Figure 6-9 XRD spectra of the 400°C/168hrs and 550°C/96hrs **Au25** specimens using Cu-K α radiation. Labels are indicative of a B2 phase, a Ti₂Pd (I4/mmm) phase, a Au₄Ti (D1_a) phase, and peaks previously thought to associate with (Au,Ni)₄Ti₃..... 73

Figure 6-10 Proposed precipitation mechanism of (Au,Ni)₄Ti₃ and Ti₂(Ni,Au) in the Au25 alloy from the initial as-cast state (A) to further aged state (B). Adapted from reference [48] 75

CHAPTER 1: INTRODUCTION

Ti-Ni based shape memory alloys (SMAs) are currently used in a variety of applications such as heat-recoverable couplings and heat-shrink fasteners [1]. They also serve prominently in the medical field as new-age, surgery enhancing paraphernalia [2]. However, SMAs are limited by their inherent ability to only exhibit shape memory characteristics through martensitic transformation up to about 100°C [3-7]. This makes them unsuitable for higher temperature applications. However, NASA has been developing high temperature shape memory alloys (HTSMAs) for adaptive chevrons on exhaust nozzles to mitigate transport aircraft noise, as well as other high temperature aerospace applications [8]. Ti-Ni-based alloys with ternary additions of Pt, Pd, Hf, Zr, or Au have all shown to increase the martensitic transformation temperature [3,5-7,9-12]. In terms of the binary SMA cases, Ti-Pt, Ti-Pd, and Ti-Au exhibit some of the highest martensitic transformation temperatures, ranging from 400°C to 700°C depending on the stoichiometry and heat treatment [3,13,14]. Interestingly, there have been few studies done on the Ti-Ni-Au ternary alloy system. This research aims to gain an understanding of the phase equilibria and transformation behavior on the Ni-rich side of the Ti-Ni-Au system. The results will enhance the fundamental knowledge of Ti-Ni-based SMAs and aid in the challenge of custom tailoring HTSMAs for commercialization.

CHAPTER 2: REVIEW OF SHAPE MEMORY ALLOYS

2.1 The Shape Memory Effect and Superelasticity

Shape memory alloys (SMAs) are a unique class of materials that exhibit recoverability to a “remembered” shape after being deformed at low temperatures and heated through a transformation temperature [3,4,7]. This phenomenon is known as the shape memory effect and was discovered in the Ti-Ni system by Buhler et al. in 1963 [3,4,15]. For the purpose of this review, discussions will be focused toward metallic SMAs, specifically Ti-Ni-based alloys.

In order to fully appreciate SMAs, one must understand how such alloys elastically accommodate large amounts of strain. All SMAs exhibit martensitic transformation. This is a diffusionless transformation in solids that requires a slight shuffling of atoms by small interatomic distances, often characterized by shear-like movements [3,16]. Typically, the parent phase (high temperature austenite) transforms to a lower symmetry, product phase (low temperature martensite) without varying composition. A simplified example of this transformation mechanism is depicted in Figure 2-1. When the temperature reaches a critical value, the martensite start temperature (M_s), martensite begins to form via shear-like mechanisms and completes at the martensite finish temperature (M_f). However, if there is an increase in temperature, the martensite phase becomes unstable causing austenite to reform at the austenite start temperature (A_s) and finish at the austenite finish temperature (A_f). Interestingly, it is quite common to have multiple variants termed correspondence variants of martensite, which tend to form crystallographic twins to reduce energy and accommodate stress [3,16].

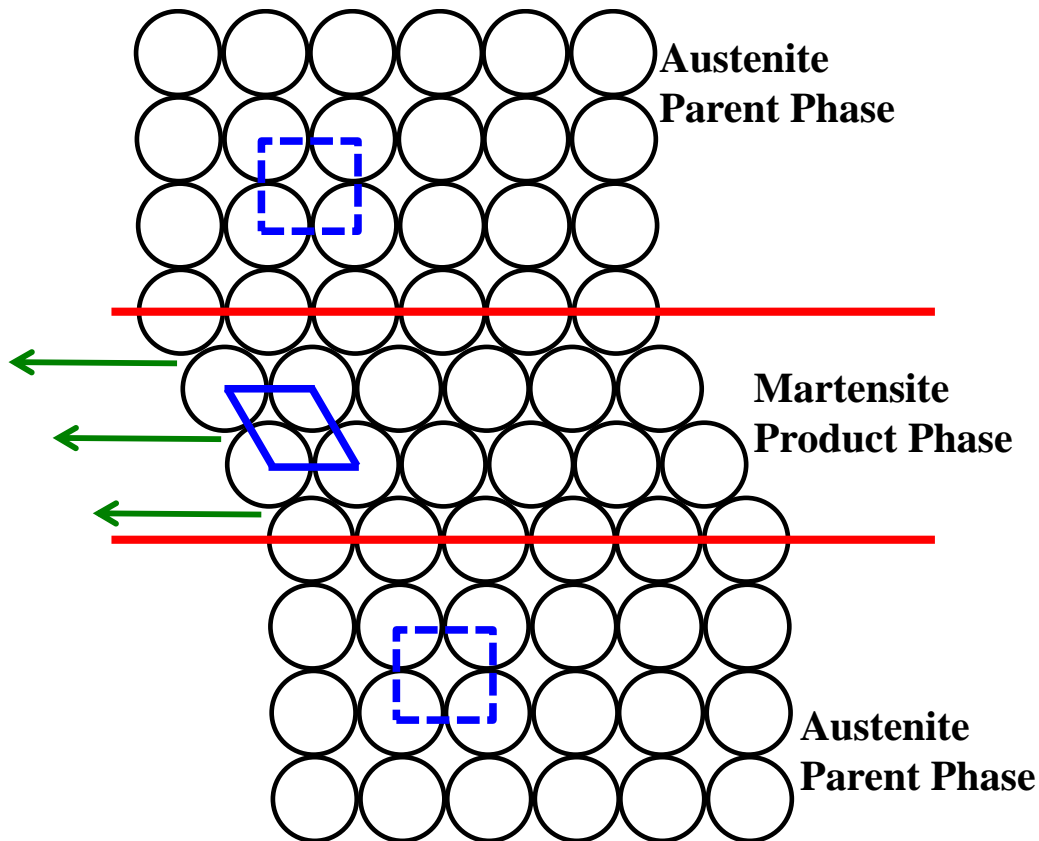


Figure 2-1 Simplistic view of martensitic transformation showing austenite to martensite and the reverse transformation. Adapted from reference [16].

A schematic view of martensitic transformation in terms of property change and temperature is depicted in Figure 2-2 (A). Notice upon heating austenite begins to form at A_s and finishes at A_f . Similarly, the reverse transformation occurs the same way with M_s and M_f . The corresponding Gibbs free energy curve of both the austenite and martensite phases, with respect to temperature, is shown in Figure 2-2 (B). It is important to note that once the temperature is shifted from the equilibrium temperature (T_0), one phase becomes dominant with a lower free energy. Also, in order to form martensite, supercooling is necessary, denoted by ΔT_{quench} in Figure 2-2 (B) [16].

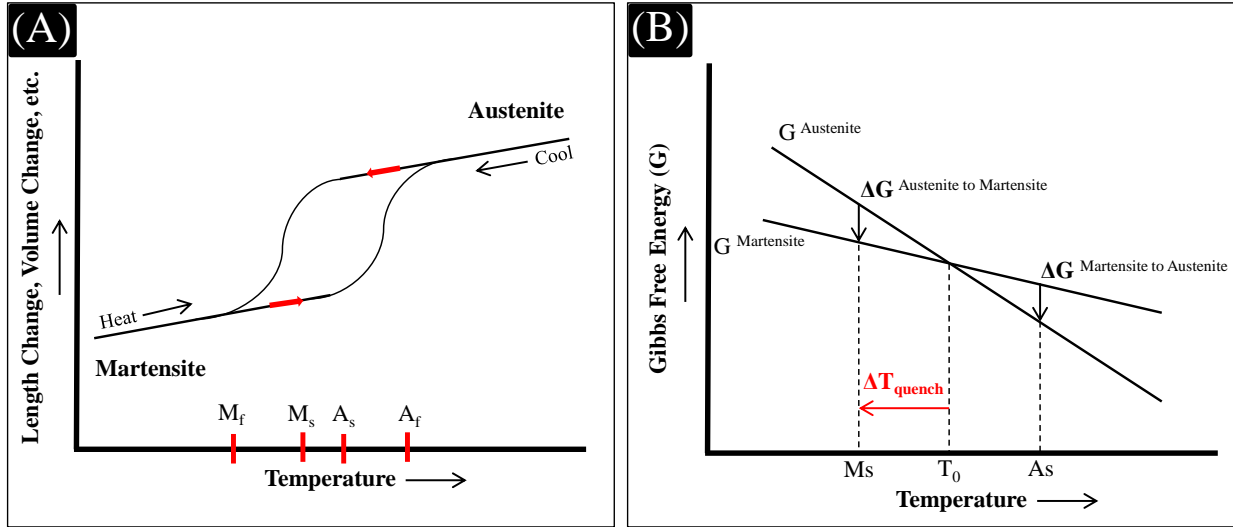


Figure 2-2 Schematic of martensitic transformation with temperatures of interest (A) and corresponding free energy schematic of martensitic transformation (B). Adapted from references [5,16].

The martensitic transformation is typically categorized as thermoelastic or non-thermoelastic [3,16]. This gives rise to a thermal transformation hysteresis, as evident in Figure 2-2 (A). Systems with a small hysteresis are considered thermoelastic and accommodate transformation strains elastically. They require small driving forces for the formation of austenite, upon heating, or martensite, upon cooling [16]. Systems that are non-thermoelastic traditionally exhibit a large transformation hysteresis and require high driving forces for martensite and austenite formation [5]. However, SMAs typically follow thermoelastic behavior since they exhibit reversible transformations [3,16]. In this sense, permanent defects are not introduced during states of stress. Instead, the presence of martensite twins aids in elastically accommodating stress. If the stress is too large, as to induce plastic deformation, then that portion is non-recoverable via the shape memory effect.

Similar to the shape memory effect, SMAs can also exhibit superelasticity. This phenomenon occurs when a sample is loaded at a temperature above A_f . This creates a stress

induced martensite to accommodate the strain [3,5,16]. However, this martensite is not stable at this temperature under normal conditions. Therefore, upon unloading, the stress induced martensite undergoes the reverse transformation back to austenite. This “elastic” stress accommodation at high temperatures is termed superelasticity. Both the shape memory effect and superelasticity are shown schematically with stress and temperature in Figure 2-3. The shape memory effect occurs up to A_s , with specific loading conditions. Both the shape memory effect and superelasticity (SE) can occur between A_s and A_f , but SE is dominant in this region [16]. Furthermore, only SE is active between A_f and M_d . However, at temperatures above M_d , plastic deformation will occur and cannot be completely recovered.

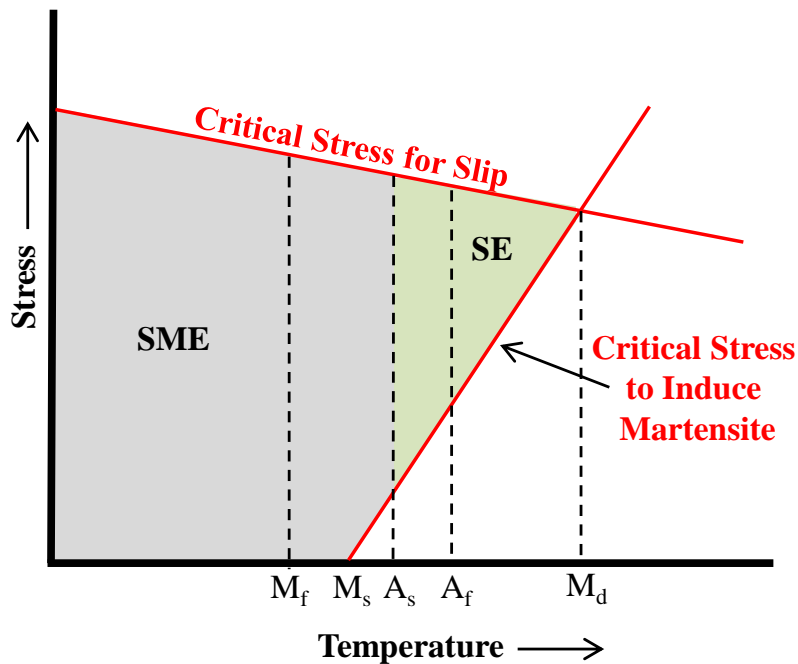


Figure 2-3 Diagram of the shape memory effect (SME) and superelasticity (SE) dependent on stress and temperature. Adapted from reference [16].

2.2 Ni-Ti-based SMAs

Ti-Ni-based alloys are the most commercially applicable SMAs due to their favorable mechanical properties, work output, and recoverable strain [3,4]. The binary Ti-Ni phase

diagram is shown in Figure 2-4. At high temperatures and near equiatomic compositions, the Ti-Ni system forms an austenite phase with an ordered B2 (CsCl) structure. It is important to note that above 1090°C the ordered B2 phase transitions to BCC [4]. Upon cooling, the B2 phase transforms via one of three possible mechanisms, as shown in Figure 2-5. The transformation paths are limited due to the ordered nature of the transition [17]. The austenite phase can transform directly to a B19' monoclinic martensite, which is typical of solution treated Ti-Ni alloys [4]. The B2 phase can also transform via R phase (Trigonal), typical of aged Ti-Ni alloys and Ti-Ni-Fe alloys [4]. Lastly, the austenite can form a B19 (orthorhombic) martensite. It is important to note that composition and heat treatment determine the final stable phase [4].

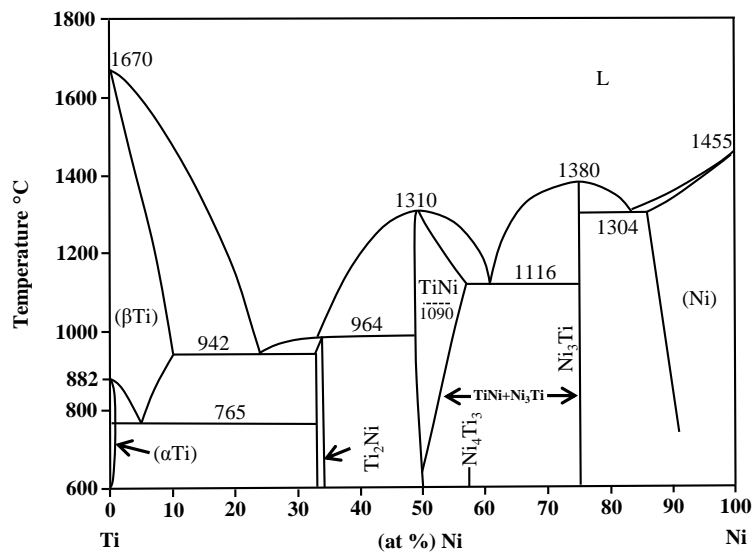


Figure 2-4 Binary Ti-Ni Phase Diagram. Adapted from reference [4].

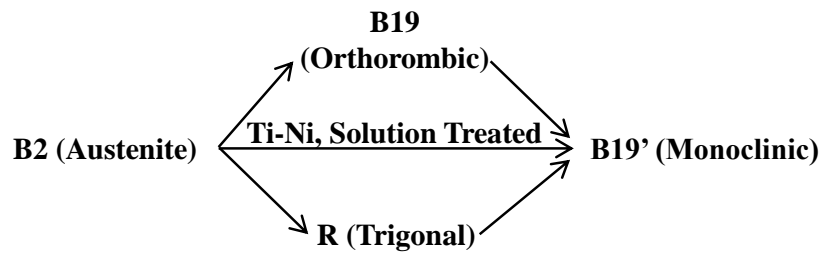


Figure 2-5 Three possible transformation paths for Ti-Ni SMAs. Adapted from reference [4].

The Ni-rich side of Ti-Ni SMAs has been the most extensively studied [3-6,18]. This is due to the larger solubility of Ni in the B2 phase, which is known to promote Ni-rich precipitation with various heat treatments [3,4,16]. It was ultimately found that this Ni-rich precipitation was metastable and could transform via the following mechanism [4]:



Numerous heat treatment regimens were utilized to determine conditions for producing one or a combination of the above phases [4]. In terms of shape memory properties, the Ni_4Ti_3 phase is quite important because it has the potential to strengthen the microstructure through precipitate hardening, while at the same time raise the martensitic transformation temperature [3,4,9]. The temperature change stems from the concentration of Ni in the B2 phase. It is well known that increasing the Ni concentration in solution treated, Ti-Ni SMAs results in a dramatic decrease in martensitic transformation temperature [3,4,16]. However, heat treatments can promote Ni-rich precipitation, which strengthen the alloy and create a Ti-rich matrix. This ultimately increases the transformation temperature, but is limited due to the low solubility of excess Ti in the B2 phase [4].

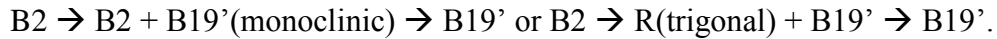
2.3 Ni-Ti-based High Temperature Shape Memory Alloys (HTSMAs)

A new hybrid of SMAs, termed high temperature shape memory alloys (HTSMAs), has emerged due to the need for materials that are functional at higher temperatures. Traditional Ni-Ti-based SMAs are limited to roughly 100°C, since they are not operable above this temperature [3,4,6,18]. However, ternary alloying of Ni-Ti SMAs with elements such as Pt, Pd, Hf, Au or Zr has shown promise in increasing transformation temperatures and promoting better mechanical stability [3,5-7,9-12,18].

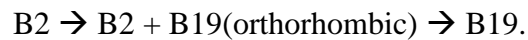
2.3.1 Ni-Ti-Au HTSMAs

Specific to this thesis, it is known that Pt, Pd, and Au all share an affinity to sit on Ni lattice sites within the ordered B2 phase [19,20]. Consequently, much work has been done on the Ti-Ni-Pd and Ti-Ni-Pt alloys [5,21-23]. In both cases, complicated precipitate structures were found [22,23]. However, there is minimal literature on the Ti-Ni-Au system, even though the binary Ti-Au SMA has one of the highest transformation temperatures [3,13,14].

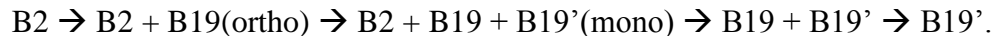
The binary Ti-Au phase diagram is shown in Figure 2-6. Similar to Ti-Ni SMAs, the Ti-Au system forms an ordered B2 (CsCl) structure, near equiatomic concentrations at high temperatures. The martensitic transformation paths of Ti-Ni-Au alloys were studied by Sivokha and Khachin [24]. Three transformation mechanisms were found via XRD depending on the Au concentration. For alloys with < 8 at % Au, the transformation sequence was [24]:



The low Au concentration alloys follow the mechanisms found in the binary Ti-Ni system. At ≥ 20 at % Au, the transformation sequence terminates at an orthorhombic martensite [24]:



Lastly, for intermediate concentrations of Au (9-15 at % Au), the transformation is much more complicated [24]:



These results are consistent with the findings of Declairieux et al. who studied an equiatomic $Ti_{50}Au_{50}$ SMA [13]. Within this regime, the orthorhombic martensite is expected [24]. XRD results of the equiatomic Ti-Au alloy indicated a B19 martensite with lattice parameters: $a = 2.994 \text{ \AA}$, $b = 4.636 \text{ \AA}$, and $c = 4.887 \text{ \AA}$ [13]. In terms of thermal analysis, the $Ti_{50}Au_{50}$ alloy exhibited transformation peaks near 600°C , indicating great potential for high temperature

applications [13]. These results are also consistent with the earlier work of Donkersloot and Van Vucht on near equiatomic Ti-Au, Pd-Ti, and Ti-Pt alloys [14].

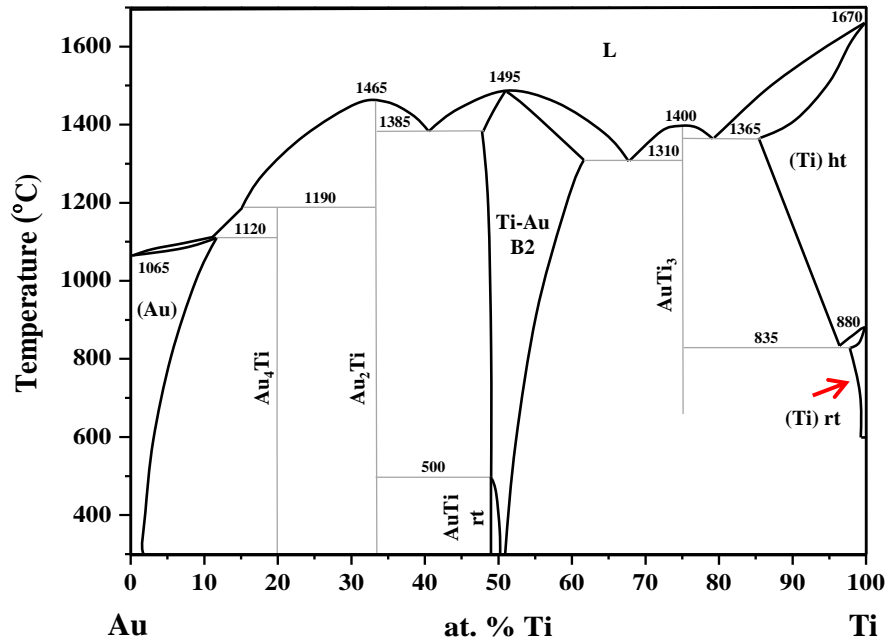


Figure 2-6 Ti-Au binary phase diagram. Adapted from reference [25].

One issue hindering the Ti-Au alloy is cyclic stability. The work of Wu and Wayman revealed that the Ti-Au alloy had problems with thermal-cycling and fracture due to poor ductility [26]. Ni additions were found to help ductility, but fracture was still evident [26]. Therefore, it may be possible to custom tailor a Ti-Ni-Au alloy with high transformation temperatures and good cyclic stability.

This study is pivotal, since little is known about the microstructures and processing relationships in the Ti-Ni-Au system. There is also no available ternary phase diagram for this alloy system. This thesis is presented to aid in these scientific gaps within the Ti-Ni-Au system. Specifically, the (Ni,Au) rich side of the Ti-Ni-Au alloy will be addressed. The microstructural evolution with heat treatments will be characterized and related back to shape memory properties.

CHAPTER 3: EXPERIMENTAL METHODS

Three alloys were investigated with various amounts of Ti, Ni, and Au. The target compositions of each alloy are summarized in Table 3-1. The **Au25** alloy was fabricated by NASA Glenn Research Center (GRC) via non-consumable arc melting under argon atmosphere. The **Ti 2:1** and **Au 4:3** alloys were also fabricated via arc melting under inert atmosphere at the University of Alabama. Each alloy was re-melted at least five times to ensure homogeneity. Specimens were cut from the bulk buttons via low-speed diamond saw and prepared with standard metallographic techniques.

Table 3-1 Target Alloy Compositions (at %)

Alloy Designation	Ti	Ni	Au
Au25	49.00	26.00	25.00
Ti 2:1	66.00	3.50	30.50
Au 4:3	41.70	27.40	30.90

3.1 Microprobe-WDS

Electron Microprobe Analysis utilizing wavelength dispersive x-ray spectroscopy (EPMA-WDS) was performed on the **Au25** alloy to determine average compositional chemistry. Experiments were done using a JEOL-8600 EMP with an accelerating voltage of 15 kV. A series of 15 point scans were taken on two as-cast **Au25** specimens for a total of 30 data points. Since the target composition of the **Au25** alloy was $\text{Ti}_{49}\text{Ni}_{26}\text{Au}_{25}$, each point scan was standardized via three sample standards with similar concentrations of Ti, Ni, and Au. Ni and Au concentrations were measured with LiF crystals, while Ti was measured using a PETJ crystal.

3.2 Heat Treatments

All three of the alloys were subjected to heat treatment. A large section of the **Au25** alloy button was cut via low-speed diamond saw, wrapped in tantalum foil, and encapsulated in an evacuated quartz tube backfilled with Ar to a pressure of ≈ 600 torr (This is to reduce oxidation and create an inert heating environment). It was then solution treated at 1050°C in a Thermolyne 21100 tube furnace for three hours followed by water quenching. During quenching, the quartz tube was broken to ensure fast cooling. Samples were then cut from the solution treated **Au25** specimen via low-speed diamond saw and subjected to further isothermal ageing at 400°C and 550°C .

For ageing, the **Au25** solution treated specimens were also wrapped in tantalum foil and placed in a Thermolyne 21100 tube furnace. The furnace was evacuated via roughing pump and purged with argon three times. The samples were then aged under dynamic argon flow. The 400°C heat treatment consisted of isothermal ageing for 5 min, 15 min, 30 min, 1 hr, 2 hrs, 4 hrs, 10 hrs, 24 hrs, 48 hrs, 72 hrs, 96 hrs, 120 hrs, 168hrs, and 1000 hrs with each step followed by water quenching. The 550°C heat treatment regime was abbreviated and consisted of isothermal ageing for 1hr, 10 hrs, 24 hrs, 48 hrs, 96 hrs, 168hrs, and 192 hrs with each step followed by water quenching. Another section was also cut from the as-cast **Au25** alloy and wrapped in tantalum foil. This specimen was encapsulated in a quartz tube following the methods described above and annealed at 1050°C for 3 hrs followed by furnace cooling.

The **Ti 2:1** and **Au 4:3** alloys were not solution annealed, but were also subjected to isothermal ageing at 550°C . One specimen from each was cut via low-speed diamond saw and wrapped in tantalum foil. Both samples were then placed in a Thermolyne 21100 tube furnace

and isothermally aged at 550°C for 96 hrs under dynamic argon flow, followed by water quenching.

3.3 Vickers Microhardness

To accompany the ageing regimes of the **Au25** alloy, Vickers hardness measurements were taken at each stage of the 400°C and 550°C heat treatments. Samples were hot mounted and polished via standard metallographic techniques to a 2400 grit finish. A series of 10 indents were taken with a Vickers hardness tester under a 1kgf load and 15 sec hold time. The average of these indents was used to develop age hardening curves.

3.4 Scanning Electron Microscopy –EDS

All specimens were examined in a JEOL-7000 FE scanning electron microscope (SEM) equipped with an Oxford Instruments silicon drift EDS system. Imaging was done at a working distance of 10mm and an accelerating voltage between 20-30 kV. All images were taken in the backscattered electron (BSE) mode to improve atomic number contrast (Z) of phases present. Energy dispersive spectroscopy (EDS) was also performed when appropriate at an accelerating voltage of 20 kV. For EDS scans, spot size was varied in order to achieve ideal dead times of less than 10%. All SEM-EDS data is based on a minimum of 3 point or area scans. All SEM samples were hot mounted in PolyfastTM and prepared via standard metallographic techniques to a 1µm diamond slurry finish.

3.5 Transmission Electron Microscopy

Specimens for transmission electron microscopy (TEM) were prepared by two different methods. The mechanical method involves cutting thin specimens from samples of interest via low-speed diamond saw. The thin sections are then adhered to holding blocks and ground down to a thickness of \approx 150-200 microns with a series of SiC grinding papers and water. Three

millimeter disks are then cut out using a slurry-drill with a diamond tipped, copper cutting bit and SiC water slurry. Each disk is then adhered with superglue to a micron leveling block and manually ground down to a thickness of ≈ 100 microns or less with 1200 grit SiC paper and water. Then, each disk is dimpled with a series of diamond slurries ($9\mu\text{m} / 3\mu\text{m}$) and finished with a $0.05\ \mu\text{m}$ colloidal silica suspension. Finally, each disk is placed in a Gatan Model 691 Precision Ion Polishing System (PIPS), first at 8 degrees and $\approx 4\text{keV}$ with rotation for initial perforation, then 7 degrees at 1keV with rotation for final thinning. This preparation method allows for the production of large surface area for examination via TEM. The focused ion beam (FIB) in-situ lift-out method for TEM foil preparation was also used for some specimens [27].

All TEM specimens were examined in an FEI Tecnai F-20 200 kV transmission electron microscope (TEM), equipped with a CCD camera for scanning transmission electron microscopy (STEM), an EDAX EDS system, and a high angle annular dark field detector (HAADF). In all cases, an FEI double-tilt holder was used to allow tilting to specific zone axes. Bright field images and selected area diffraction patterns (SADPs) were collected on film with appropriate exposure times. Film development followed standard techniques and all micrographs were digitized via a backlit scanner. STEM images were collected via a digital CCD camera. All TEM-EDS data was analyzed using the ES VisionTM Analysis software with thickness correction [28].

Crystal MakerTM and Single CrystalTM software were used to create unit cell crystals and theoretical selected area electron diffraction patterns (SADPs) for phases of interest [29,30]. They were also used in conjunction with stereographic projections to develop phase orientation relationships. This software suite was quite useful in determining the crystal structures and symmetry of nano-scaled precipitation.

3.6 X-ray Diffraction

X-ray diffraction was done on all samples in order to identify the phases that were present and for comparison with TEM and SEM findings. Spectra were collected on a Phillips X'Pert MPD XRD with Cu-K α radiation ($\lambda = 0.154056$ nm). Bulk specimens were mechanically ground with SiC grinding paper and water to a 2400 grit finish. All scans were run from $2\theta = 20^\circ$ - 110° at an operating condition of 45 kV and 40 mA. In order to minimize orientation effects of bulk materials, several different orientations were examined for each sample of interest.

3.7 3D Atom Probe Tomography

Several of the **Au25** 400°C heat treated alloys were examined in a CAMECA Local Electrode Atom Probe (LEAP). All tips were fabricated in an FEI Quanta 3D Dual Beam (FIB-SEM). Specimens were prepared into needle-like tips on pre-fabricated Si posts via the in-situ lift-out technique of preparing atom probe specimens [31]. To minimize contamination, finished tips were subjected to a low kV Ga ion cleaning at 5kV and .23nA, followed by immediately placing them into the LEAP under high vacuum.

Samples were run in both voltage and laser-assisted voltage modes. However, best results were obtained in laser-assisted mode. This is hypothesized to be the result of the large evaporation field difference of Ti and Ni in comparison to Au. Optimal run parameters were as follows: laser-assisted mode, 40 K temperature, 0.5 nJ laser energy, 250 kHz pulse frequency, 0.5 % evaporation rate, and soft-turn on / free running mode. These parameters resulted in multiple data sets with golden hits > 70 % and ion counts in excess of 10 million ions. These two criteria were the minimum factors required for further consideration and data reconstruction analysis. It is important to note that most voltage runs resulted in immediate tip fracture upon turn on near ~ 5500 volts.

Atom probe data was reconstructed via Cameca's Integrated Visualization and Analysis Software (IVASTM) [32]. Tips were fitted via tip-shank-profile from a high resolution micrograph of the tip geometry taken in the FIB. This ensures a better reconstruction fit in comparison to simply using the voltage curve approximation. Iso-concentration surface analysis was employed to aid in determining the compositional chemistries of phases present.

3.8 Differential Scanning Calorimetry

Differential scanning calorimetry was also performed on select **Au25** alloy specimens using a TA Instruments Q200 DSC equipped with a refrigerated cooling system. Run parameters consisted of cycles from -90°C to 300°C, with a temperature change rate of 10°C / min. Most specimens were taken through four cycles, but those with no evident transformation peaks were stopped after the first or second cycle.

CHAPTER 4: CHARACTERIZATION OF AU25 ALLOY

4.1 As-Cast Microstructure

The compositional chemistry of the **Au25** alloy was verified via electron microprobe-WDS at an accelerating voltage of 15 kV. Two as-cast specimens from the bulk button were analyzed, each with a series of 15 standardized point scans. The results are indicated in Table 4-1. The numerical average of all point scans for each specimen revealed an average composition consistent with the target composition of $Ti_{49}Ni_{26}Au_{25}$.

Table 4-1 EMP-WDS Point Scans on **Au25** As-Cast Specimens

Au25 As-Cast Specimen #1				Au25 As-Cast Specimen #2			
Spectra	Au (at %)	Ni (at %)	Ti (at %)	Spectra	Au (at %)	Ni (at %)	Ti (at %)
1	24.87	26.16	48.97	16	24.84	26.15	49.01
2	24.78	26.13	49.09	17	24.72	26.47	48.81
3	25.07	26.07	48.86	18	25.08	26.09	48.83
4	24.78	26.72	48.50	19	24.42	26.53	49.04
5	24.73	26.09	49.19	20	24.35	26.65	49.00
6	24.48	26.98	48.54	21	24.33	26.29	49.38
7	25.13	26.89	47.98	22	24.30	26.90	48.79
8	24.45	27.54	48.01	23	24.60	26.51	48.89
9	24.86	26.29	48.85	24	24.03	26.08	49.89
10	24.73	26.71	48.57	25	24.46	26.54	49.00
11	24.91	26.24	48.85	26	24.20	26.63	49.17
12	24.75	26.70	48.56	27	24.30	26.62	49.08
13	24.80	26.32	48.87	28	24.61	25.15	50.24
14	24.68	26.31	49.01	29	24.65	26.19	49.16
15	24.62	26.39	48.99	30	24.45	26.14	49.41
Average	24.78	26.50	48.72	Average	24.49	26.33	49.18
Error ±	0.18	0.41	0.36	Error ±	0.27	0.41	0.41

The microstructure of the as-cast **Au25** alloy was investigated via scanning electron microscopy (SEM), shown in Figure 4-1. Alloy and phase chemistries were determined using EDS. BSE imaging of the as-cast specimen revealed a rich microstructure consisting of bright alternating platelets. This suggests precipitates that are most likely (Au,Ni) rich in comparison to the matrix based on atomic number contrast, since Au has a preference for occupying the Ni lattice sites [20]. However, a compositional difference between the matrix and platelets was not detected via EDS. It is hypothesized that the alternating platelet precipitates may be reminiscent of the Ni_4Ti_3 or Ni_3Ti type precipitation found in the binary Ni-rich, NiTi alloys [3,4].

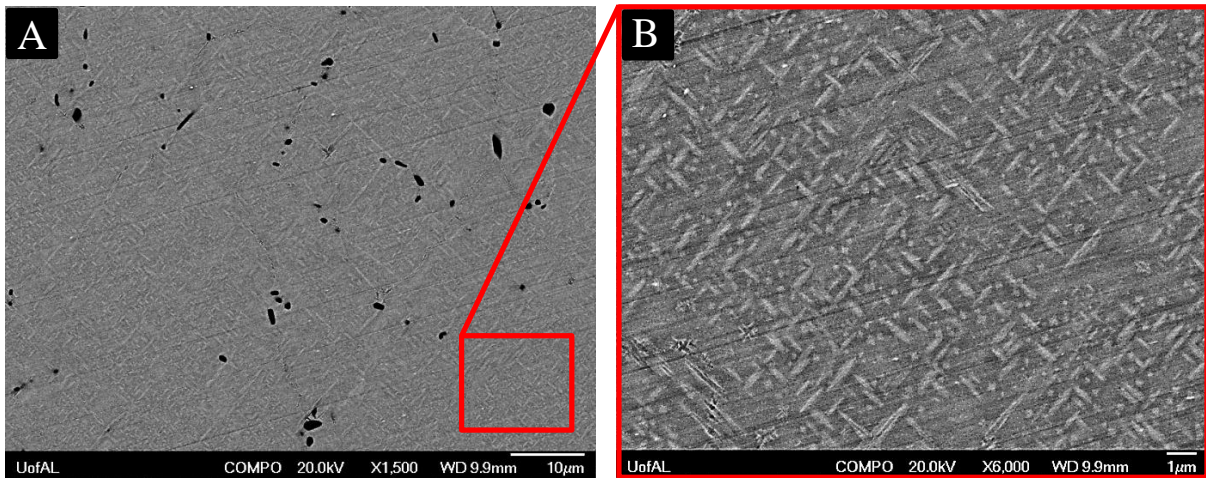


Figure 4-1 Backscattered electron (BSE) images of the **Au25** as-cast microstructure in low magnification (A) and high magnification (B).

BSE imaging also revealed dark phases (low Z) all dispersed throughout the as-cast specimen. EDS at 20 kV revealed that the dark phases had an average composition (atomic %) of 14.27 O – 52.48 Ti – 32.58 (Ni, Au). This correlates well with the stoichiometric Ti_4N_2O inclusions observed in similar alloys [4,5,33]. However, in this case, it is proposed that Au substitutes for Ni to form $Ti_4(Ni,Au)_2O$. This structure was later verified via transmission electron microscopy (TEM) utilizing selected area diffraction patterns (SADPs).

4.2 1050°C Annealed Microstructure

A large portion of the **Au25** as-cast button was solution treated at 1050°C for 3 hrs followed by water quenching. This is to promote a solid solution, ordered, Ni-Ti-Au B2 structure. The solution treated specimen was investigated via BSE imaging, as shown in Figure 4-2. BSE imaging of the solution treated **Au25** specimen revealed little to no contrast in addition to the matrix. This suggests that near-full solid solution was attained. However, the $\text{Ti}_4(\text{Ni,Au})_2\text{O}$ type oxide inclusions were still present and verified via EDS.

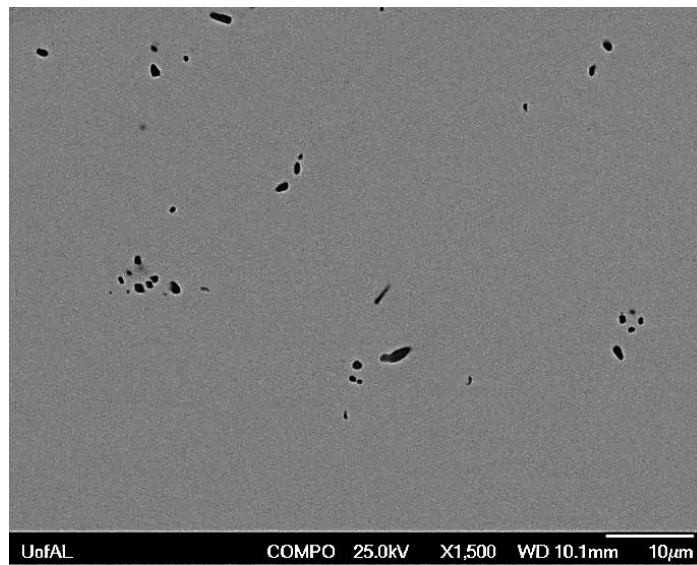


Figure 4-2 Backscattered electron image of the **Au25** 1050°C heat treated specimen.

In order to examine the crystallographic transition from the as-cast state to the solution annealed state, XRD was used. The results are presented in Figure 4-3. It is important to note that each scan was taken from a bulk specimen, so it was necessary to choose spectra from multiple orientations that exhibited optimal peak ratios. X-ray diffraction revealed that a Ni-Ti-Au B2 phase with a structure (Pm-3m) was formed. There did not appear to be any residual as-cast peaks in the solution treated spectra. However, it is possible that a small fraction of residual

phases may occupy the matrix due to inefficiencies in quenching rates following heat treatment [5].

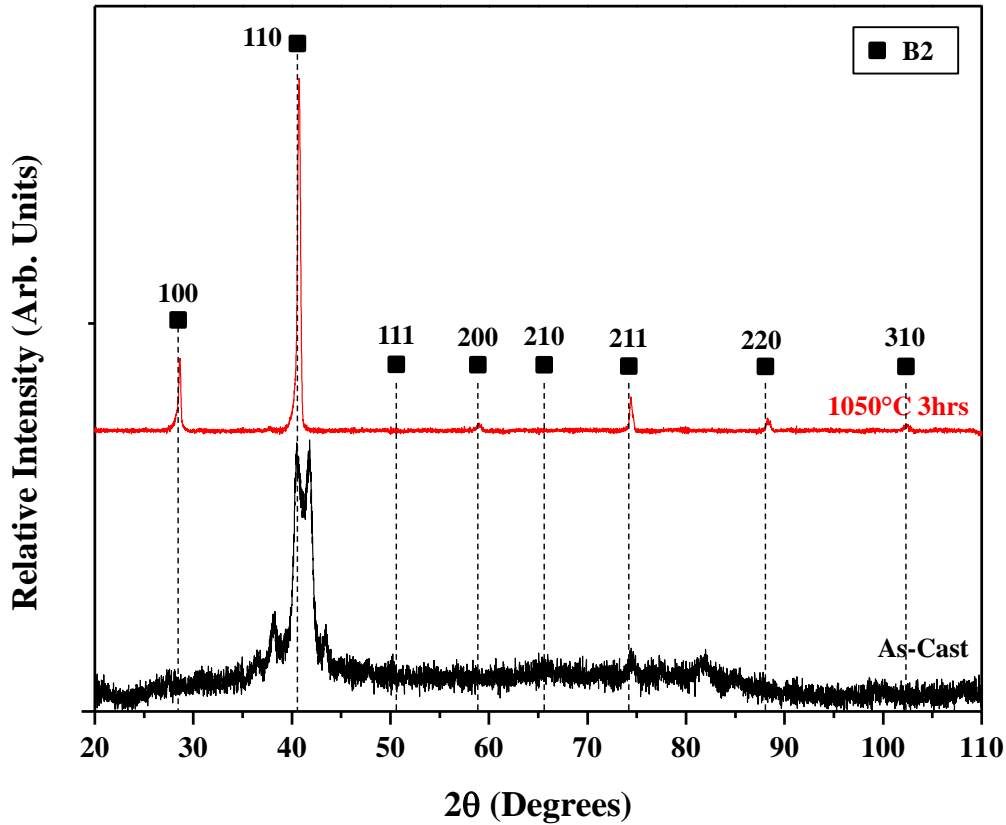


Figure 4-3 X-ray diffraction spectra of the Au25 as-cast and solution annealed specimens with B2 peaks identified.

Transmission electron microscopy (TEM) was also used to examine the microstructure of the 1050°C solution treated **Au25** specimen. Bright field (BF) images and selected area diffraction patterns (SADPs) were taken of the three primary B2 zone axes, as shown in Figure 4-4. See appendix for additional BF images of the 1050°C **Au25** specimen. The BF images revealed no precipitate contrast. However, SADPs down each of the primary B2 cubic zone axes revealed additional, faint spots other than the B2 matrix, signifying a small amount of nano-scaled precipitates. These spots were not prominent enough to characterize and tended to show

up best down the $\langle 100 \rangle_{B2}$ zone axis, Figure 4-4 (B). There were also superlattice reflections in the SADPs, most clearly visible in Figure 4-4 (A), suggesting the ordering of the B2 phase. This relates to the change in structure factors when following a transition from a body-centered to primitive bravais lattice upon ordering. However, it is important to note that additional superlattice-like spots within diffraction patterns may also arise from complex, dynamical electron scattering phenomenon occurring within the specimen [34].

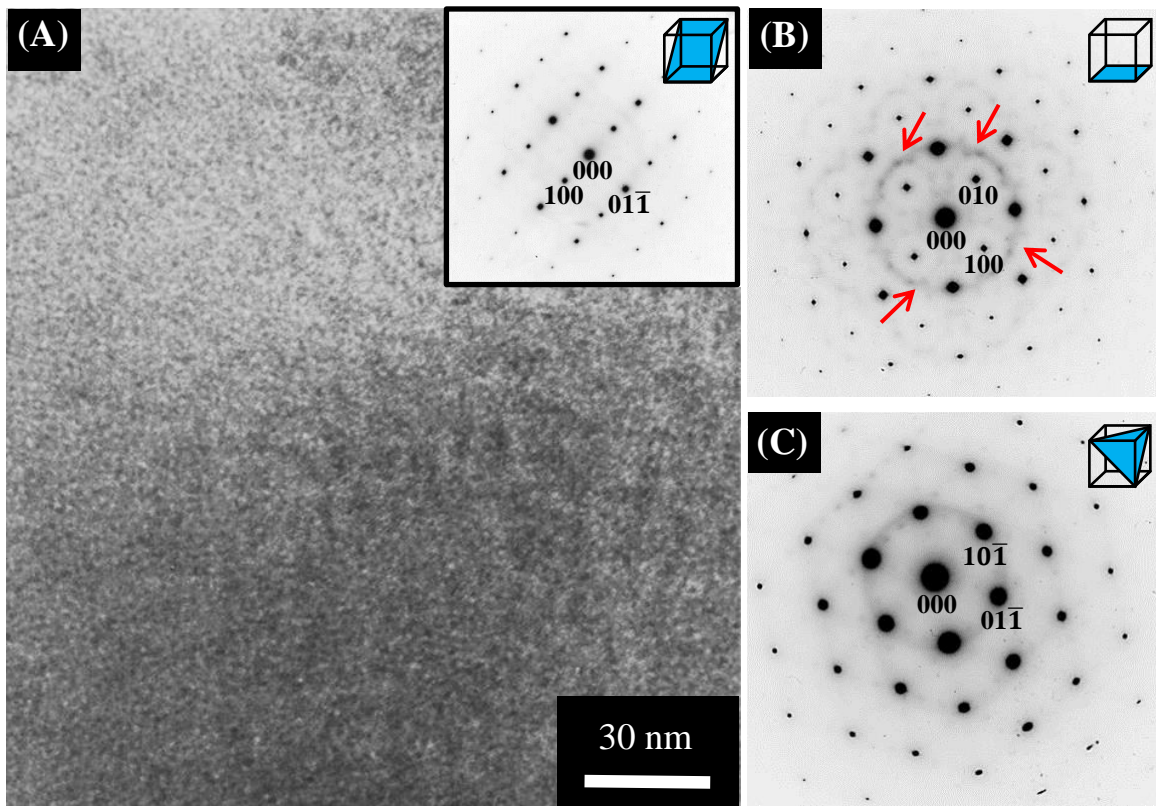


Figure 4-4 TEM BF image and SADP taken from the 1050°C solution treated **Au25** sample in the $\langle 011 \rangle_{B2}$ direction (A) and SADPs collected from the $\langle 100 \rangle_{B2}$ direction (B) and $\langle 111 \rangle_{B2}$ direction (C). The labels are the B2 cubic indices.

4.3 400°C and 550°C Heat Treated Microstructure and Properties

The **Au25** alloy was solution annealed at 1050°C and water quenched in order to form a super saturated, solid solution, B2 structure. Further ageing at 400°C and 550°C was done to produce finely-dispersed, nano-scale precipitates. This methodology has been shown to

improve structural properties like hardness, increase martensitic transformation temperatures, and also improve shape memory behavior with similar alloy systems [3-5,9,13,35]. All results of the **Au25** 400°C and 550°C heat treatments are closely related and will be addressed simultaneously.

4.3.1 Vickers Hardness Ageing Curves

Hardness ageing curves were experimentally determined for the **Au25** alloy at 400°C and 550°C. Each step of the isothermal 400°C heat treatment was followed by water quenching and Vickers hardness testing. An abbreviated isothermal heat treatment at 550°C was also done followed by water quenching and Vickers hardness testing for each step. The resulting hardness ageing curves for both temperatures are depicted in Figure 4-5. It is interesting to note the high hardness for both heat treatments, achieved at 48 hrs for the 400°C and 96 hrs for the 550°C. This indicates great precipitation hardenability, as described in sections 4.3.2 and 4.3.3. Both heat treatments also tend to follow the same trend for most of the data points. It is proposed that the growth kinetics at 400°C are too slow to achieve a true peak hardness. This is evident by the apparent plateau of the 400°C hardness curve out to 1000 hrs, Figure 4-5.

4.3.2 Microstructures as Evident in SEM

The microstructural evolution during the 400°C and 550°C heat treatments was examined via scanning electron microscopy (SEM). The main premise was to survey the phases present. Therefore, all imaging was done in backscattered electron (BSE) mode in order to utilize atomic number (Z) contrast to identify additional species present within the matrix. A series of specimens from both temperature regimes were selected as candidates for further analysis to elucidate the microstructural evolution around the peak hardness state. These specimens include

under-aged, peak-aged, and over-aged cases, with respect to hardness. The results for the 400°C heat treatment are shown in Figure 4-6.

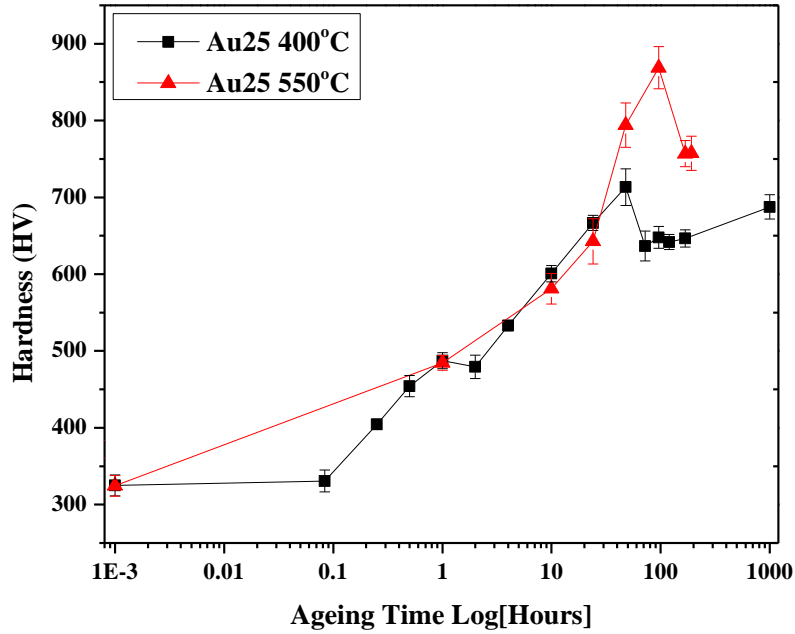


Figure 4-5 Hardness ageing curves for the Au25 solution annealed specimen at 400°C and 550°C.

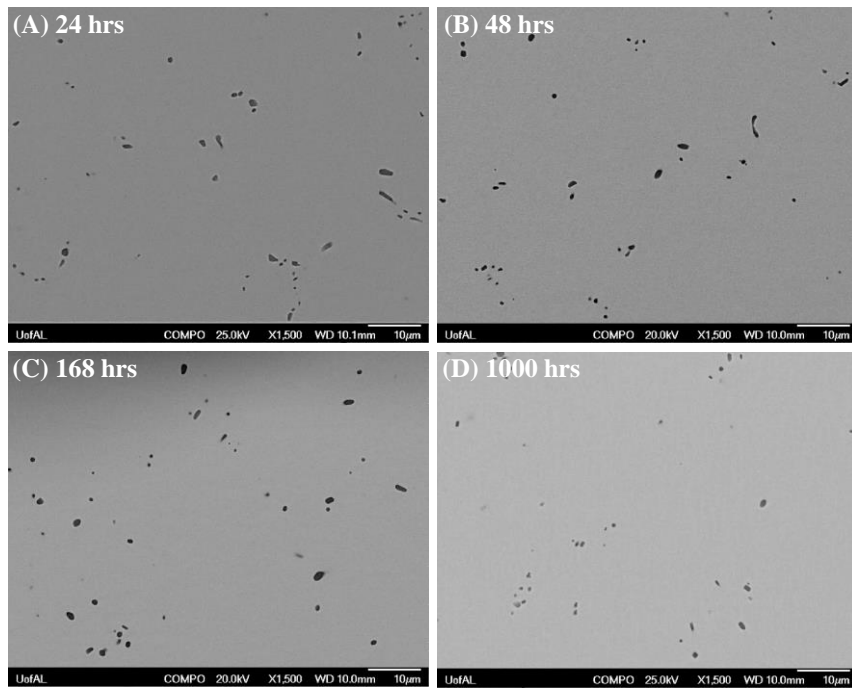


Figure 4-6 BSE images of the Au25 400°C heat treated alloy showing the under-aged (A), peak-aged (B), and over-aged cases (C) and (D).

Aside from oxide inclusions, as described in the previous section, the BSE images revealed no precipitate contrast in the matrix. This may suggest that any precipitation occurring throughout the heat treatment at 400°C is of the nano-scale. Higher magnification imaging was also attempted on all noted cases. However, even at 400°C/1000hrs there was little no to precipitate contrast detected.

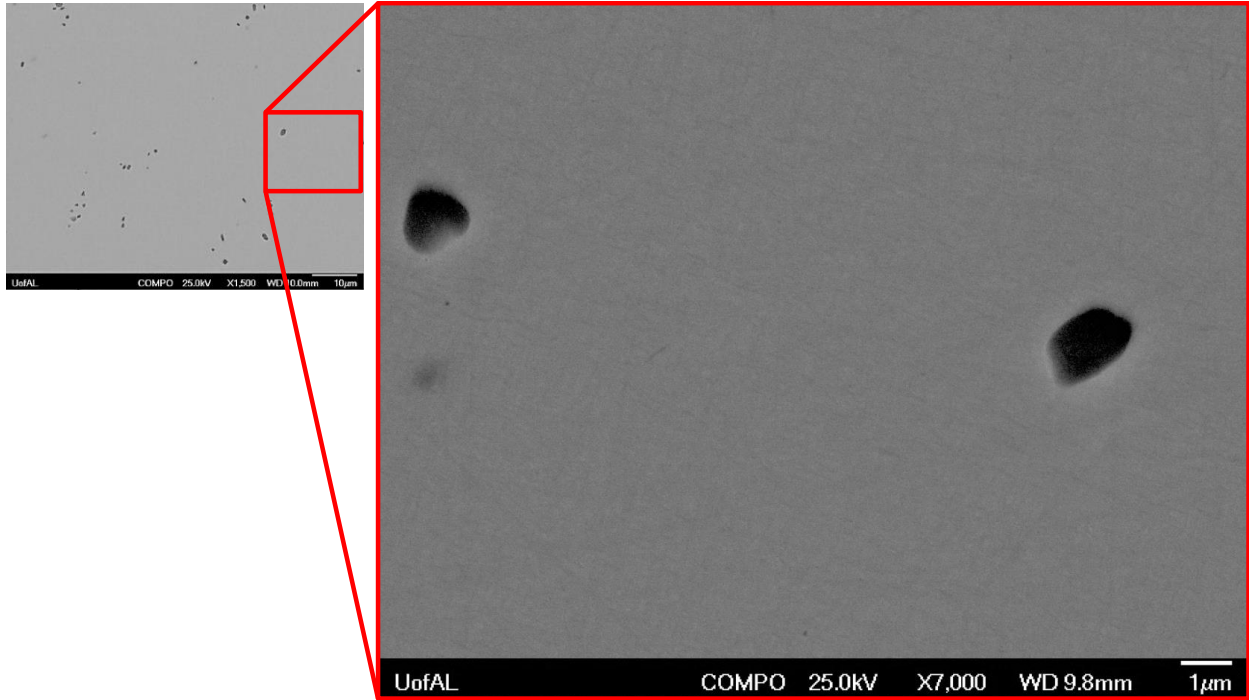


Figure 4-7 BSE image of the **Au25** alloy aged 1050°C/3hrs + 400°C/1000hrs.

The same methodology was applied to the 550°C heat treated samples. However, as shown in Figure 4-8, there was a clear evolution of microstructure. The microstructure consisted of a matrix with a high density of fine-scale, precipitates. As is shown in Figure 4-8 (D), BSE imaging of the (1050°C/3hrs + 550°C/192hrs) specimen revealed two variants of alternating dark platelets that appear orthogonal to each other. It is hypothesized that these phases are Ti-rich since they are much darker in comparison to the matrix. Additional, smaller precipitates also appeared to populate the matrix. However, the contrast of the fine-scale precipitates was hard to

distinguish via SEM. EDS was attempted on all constituent phases at an accelerating voltage of 20 kV, but was unsuccessful since each point scan returned bulk target composition values with little variation between scans. Therefore, transmission electron microscopy (TEM) was used to further characterize the microstructures of select 400°C and 550° aged specimens.

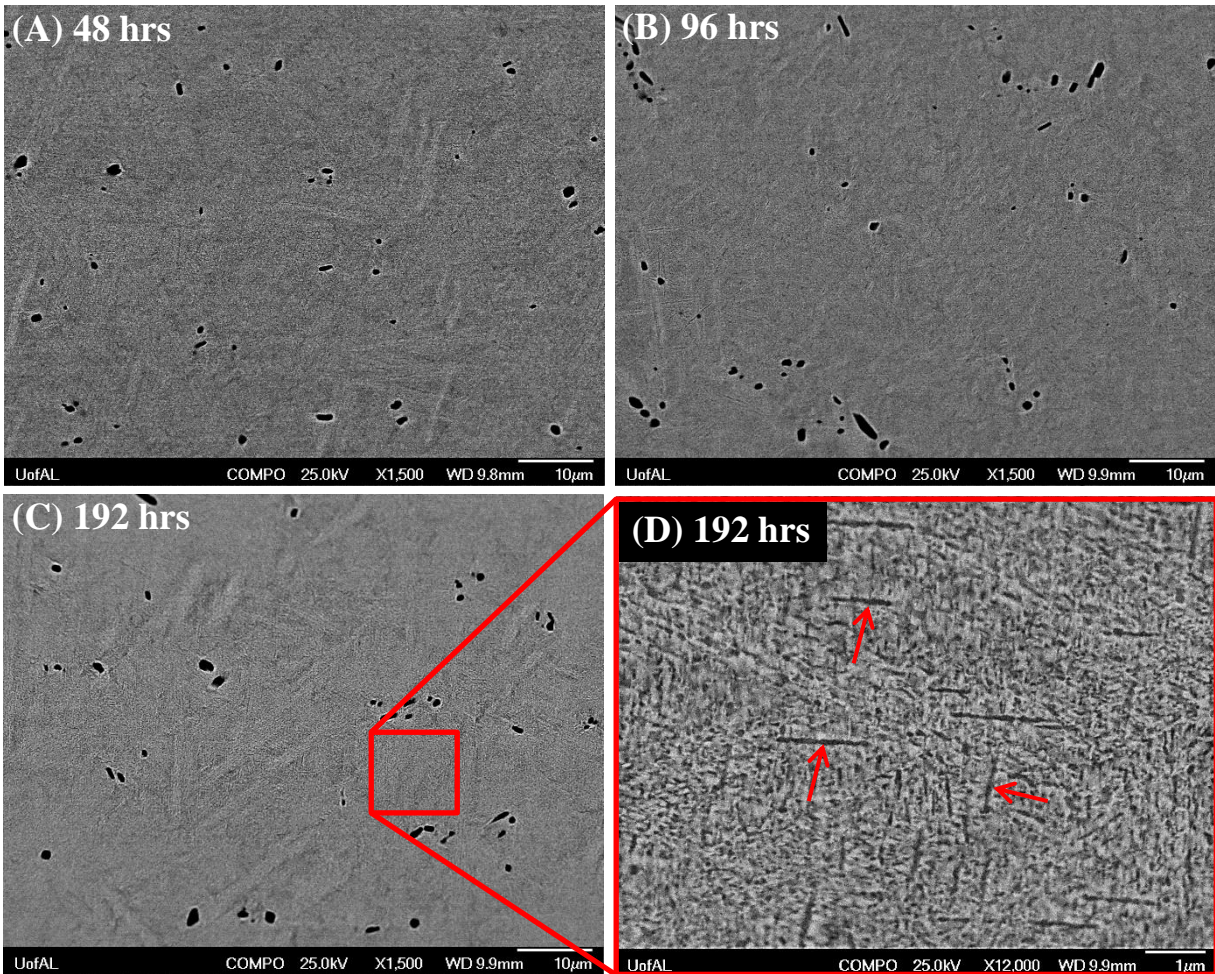


Figure 4-8 BSE images of the **Au₂₅** 550°C heat treated alloy showing the under-aged (A), peak-aged (B), low magnification over-aged (C), and high magnification over-aged (D).

4.3.3 Microstructures as Evident in TEM

TEM foils from several **Au₂₅** specimens aged at 400°C and 550°C were made. BF images and SADPs taken of the **Au₂₅** alloy aged (1050°C/3hrs + 400°C/48hrs), are shown in

Figure 4-9. See appendix for additional BF images. This alloy is considered to be “peak-aged” based upon the 400°C hardness ageing curve. It is interesting to note that there was an increase in precipitation contrast within the BF images down each of the major cubic B2 zones, see appendix. The SADPs were similar to the patterns taken from the 1050°C annealed sample, Figure 4-4. However, the precipitate spots were much more prominent, indicating precipitate growth during ageing.

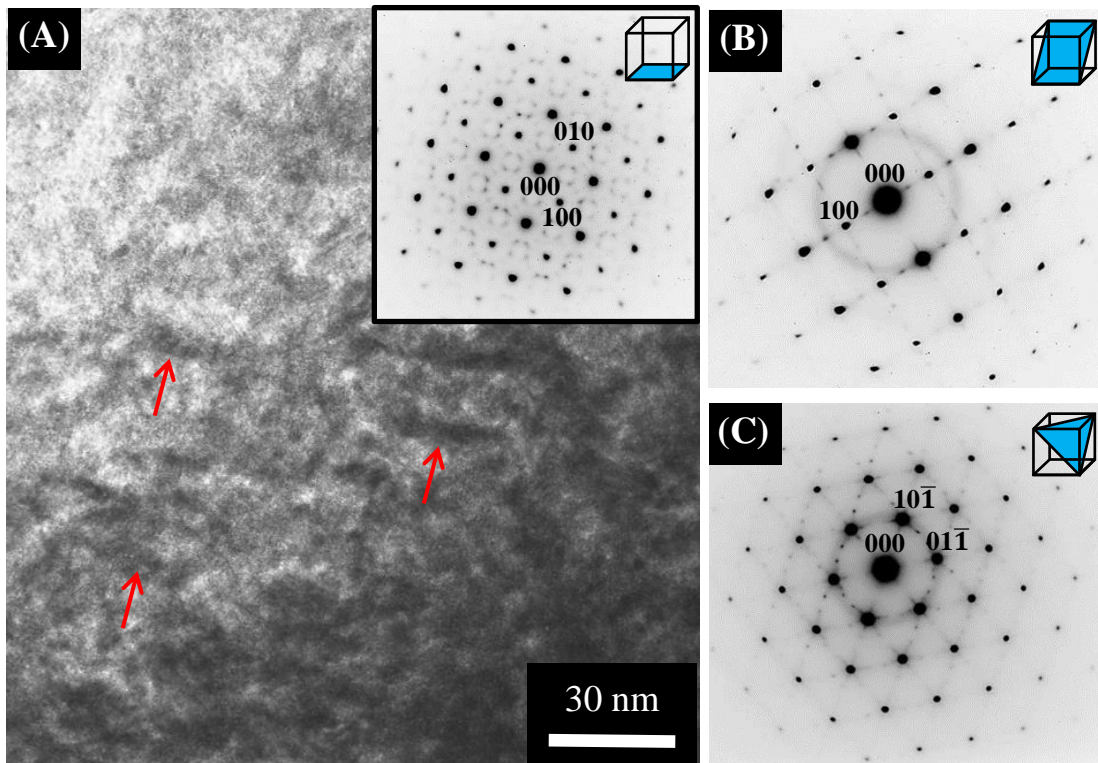


Figure 4-9 TEM BF image and SADP taken from the 1050°C/3hrs + 400°C/48hrs **Au25** sample in the $\langle 100 \rangle_{B2}$ direction (A) and SADPs collected from the $\langle 110 \rangle_{B2}$, (B) and $\langle 111 \rangle_{B2}$ directions (C). The labels are the B2 cubic indices.

For an alternative view of the precipitate morphology, BF imaging was also done on the (1050°C/3hrs + 400°C/48hrs) sample down the $\langle 115 \rangle_{B2}$ direction. This minor zone axis yielded better precipitate contrast in the matrix, as shown in Figure 4-10. The TEM BF imaging clearly revealed lenticular, nano-scale precipitates within the matrix. This precipitate phase appears to

be less than 30 nm in length and less than 12 nm in width. As was the case with the 1050°C/3hr SADPs, the precipitate spots in the (1050°C/3hrs + 400°C/48hrs) specimen were also too faint to fully characterize. Therefore, the 400°C over-aged cases were examined. The idea was to coarsen the precipitate phase so that its identity in the SADPs would be more distinguishable.

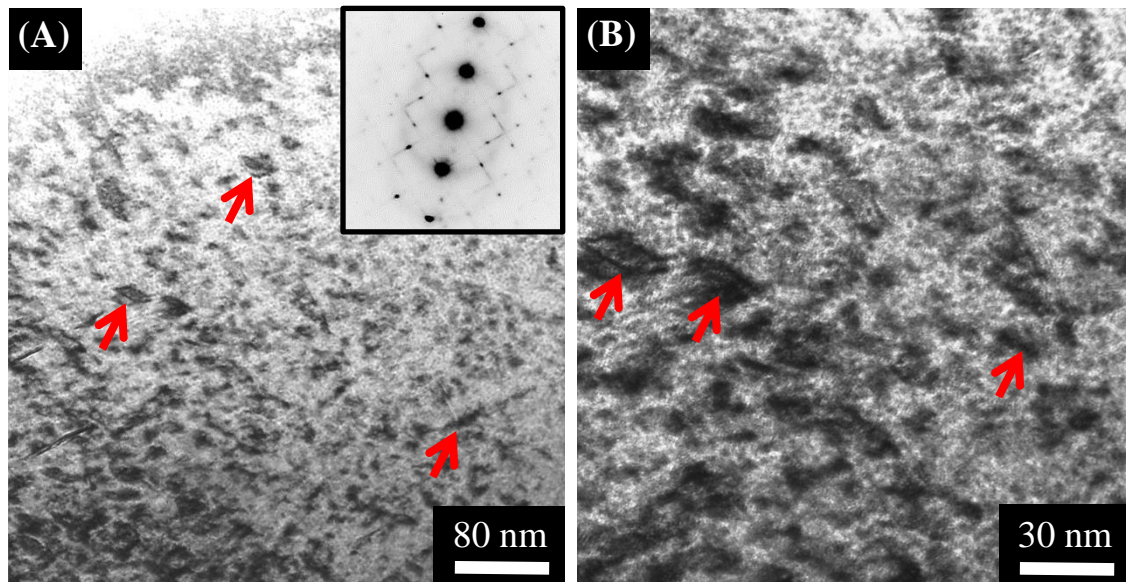


Figure 4-10 TEM BF image and inset SADP (A) and higher magnification BF image (B) taken from the 1050°C/3hrs + 400°C/48hrs **Au₂₅** sample down the $\langle 115 \rangle_{B_2}$ direction.

TEM foils of the (1050°C/3hrs + 400°C/168hrs) and (1050°C/3hrs + 400°C/1000hrs) samples were also made. BF imaging and SADPs of the 168 hr 400°C foil revealed similar and more prominent precipitation, as shown in Figure 4-11. The BF micrograph in Figure 4-11 (A) clearly reveals the presence of two different precipitate phases. The first phase, a series of orthogonal alternating platelets, is analogous to the precipitation found in the BSE imaging performed on the (1050°C/3hrs + 550°C/192hrs) sample, Figure 4-8. The platelets also appear to have a habit plane parallel to the $\langle 100 \rangle_{B_2}$ direction. The second phase is similar to the precipitation found in the 1050°C/3hrs and (1050°C/3hrs + 400°C/48hrs) specimens, Figures 4-4

and 4-9, respectively. It is hypothesized that initially, the smaller precipitate forms first and then the larger platelet variants are promoted during further ageing. This is consistent with the later appearance of platelets in the BF images and SADPs. It is very interesting to note that the SADPs of the (1050°C/3hrs + 400°C/168hrs) foil appear to be uniquely different than the phases found in similar SMA alloys like the HAN in Ni-Ti-Hf alloys and P-Phase in Ni-Ti-Pd alloys [21,22,36], show in Figure 4-11.

The presence of precipitate spots and streaks in the $\langle 100 \rangle_{B2}$ SADP is consistent with the notion of having two different precipitates since each has its own shape factor that exhibits a particular signature in SAD [34]. The streaks are analogous to the platelet orientation and an apparent habit plane that is parallel to the $\langle 100 \rangle_{B2}$ direction. Thus, it is proposed that all other spots not associated with the B2 matrix are correlated to the finely-dispersed, nano-scale precipitation.

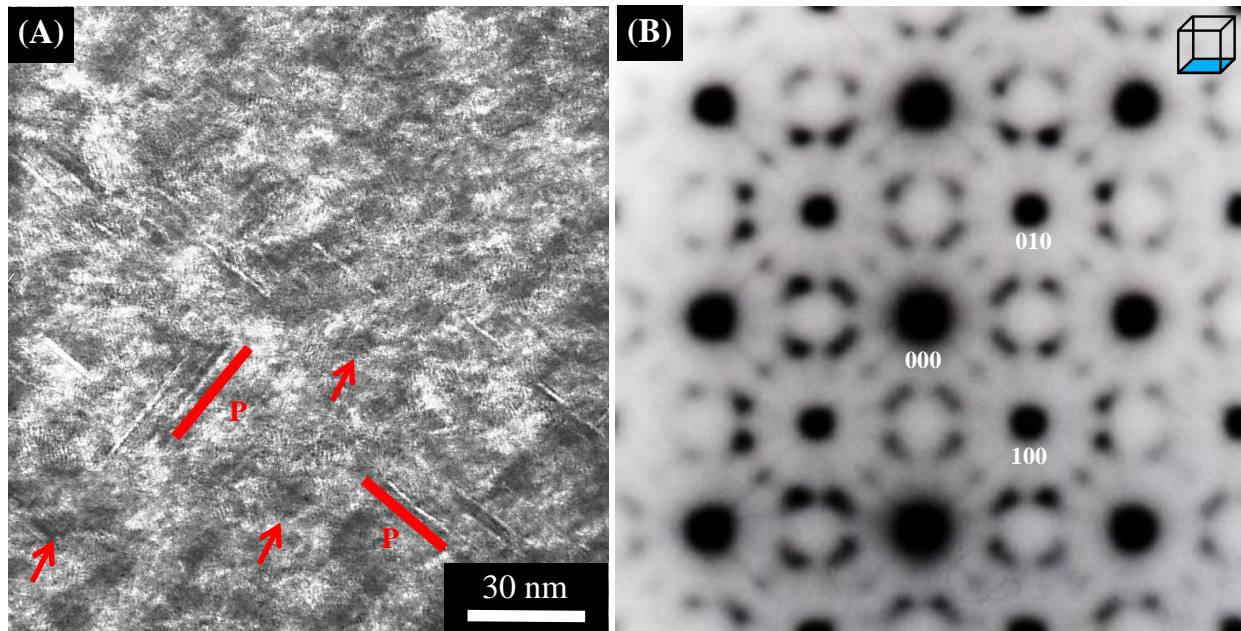


Figure 4-11 TEM BF image (A) and SADP (B) taken from the 1050°C/3hrs + 400°C/168hrs **Au25** foil down the $\langle 100 \rangle_{B2}$ direction. The labels in (B) are the B2 cubic indices. The label “P” in (A) indicates platelet. Arrows point out other PPTs.

In order to try and coarsen the precipitate phases, ageing at 400°C was taken out to 1000 hrs. A TEM foil of the (1050°C/3hrs + 400°C/1000hrs) sample was prepared. BF imaging, shown in Figure 4-12, reveals that the two platelet variants coarsened considerably, yet the smaller precipitate phase did not. This may suggest that the formation and further coarsening of the platelets occurs at the expense of the smaller phase. Identified in Figure 4-12 (B) are Moire patterns that are thought to have generated due to the interaction of the small precipitate structure with the matrix [34].

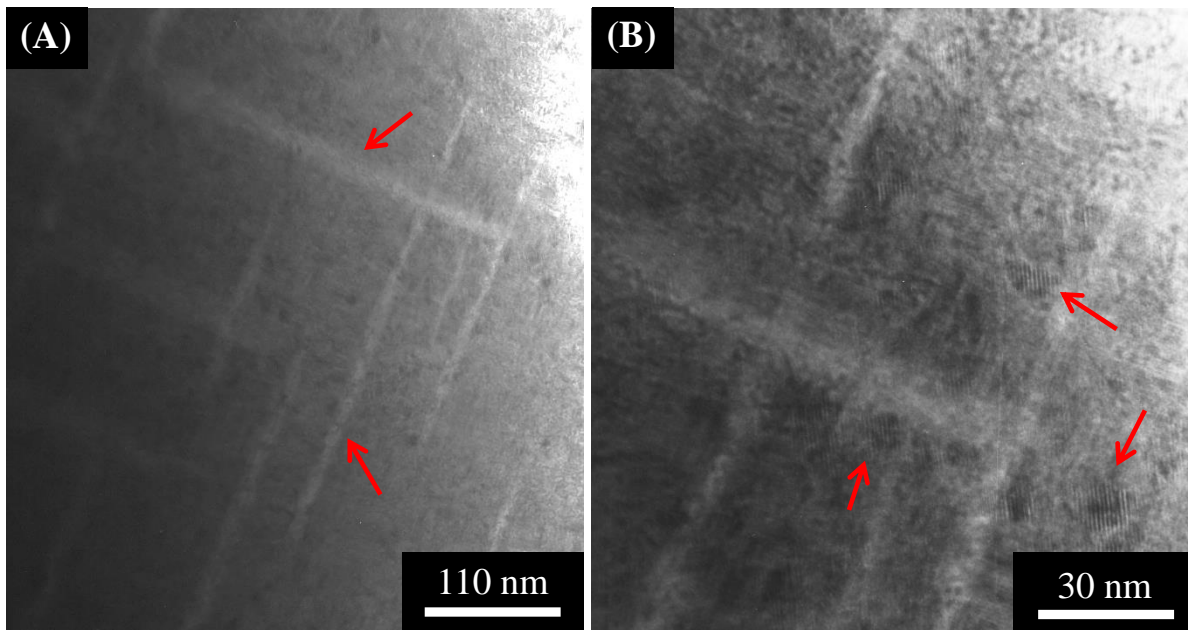


Figure 4-12 TEM BF image (A) and higher magnification BF image (B) taken from the 400°C 1000 hr **Au₂₅** foil down the $\langle 100 \rangle_{B_2}$ direction. Arrows indicate large platelets (A) and Moire patterns (B).

Scanning transmission electron microscopy (STEM) was performed on the (1050°C/3hrs + 400°C/1000hrs) sample using a high angle annular dark field (HAADF) detector to augment atomic (Z) contrast [34]. As shown in Figure 4-13, the 1000hrs sample consisted of heavily coarsened plates that appear chemically dark. This correlates to the BSE imaging of the 550°C

heat treated samples. A closer examination, Figure 4-13 (B), reveals a matrix with two variants of a bright phase. This bright phase is hypothesized to be the unidentified, nano-scale phase mentioned at short ageing times. The brighter contrast of the nano-scale phase suggests that it is rich in (Au,Ni) in comparison to the large plates and matrix. TEM-EDS was unsuccessful in determining the chemical composition of either of the phases due to the small size of the bright phase and orientation of the dark phase.

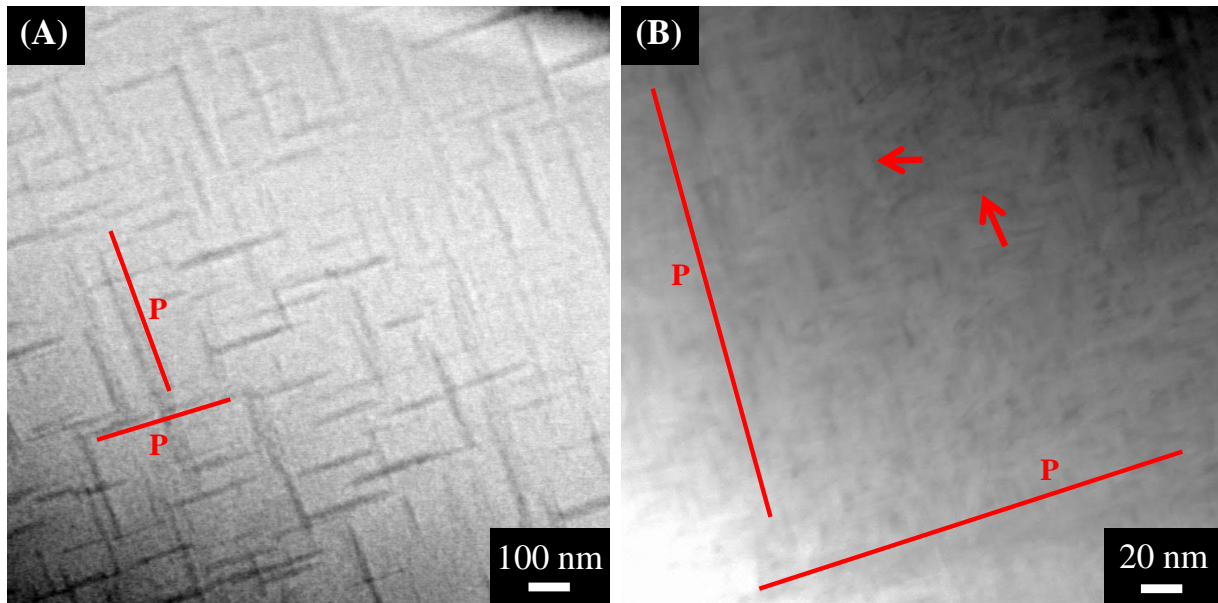


Figure 4-13 STEM-HAADF image (A) and higher magnification STEM-HAADF image (B) taken from the 1050°C/3hrs + 400°C/1000hrs **Au₂₅** foil just off the $\langle 100 \rangle_{B2}$ direction. The label “P” indicates platelet. Arrows point out PPTs.

STEM-HAADF imaging was also done on the (1050°C/3hrs + 550°C/96hrs) “peak-aged sample”. The results were quite similar to the 400°C foils, but the microstructure had coarsened, as shown in Figure 4-14. It is important to note that there was a large variation in dark platelet size in the 96 hr 550°C foil. The image depicted in Figure 4-14 (B) shows only one variant of moderately size platelets. However, the rest of the foil contained both variants and much coarser platelets. This may explain the difference in hardening behavior of the 400°C and 550°C aged samples, which will be addressed in more detail in the discussion section. The two bright

precipitate variants looked quite similar to the (1050°C/3hrs + 400°C/1000hrs) foil microstructure, shown in Figure 4-14 (A). However, the bright phase in the (1050°C/3hrs + 550°C/96hrs) foil had coarsened to about five times the size. The morphology and close-packing of the bright precipitate phase made diffraction ineffective in characterizing the crystallography. Therefore, TEM-EDS was used to obtain the compositional chemistry of both phases.

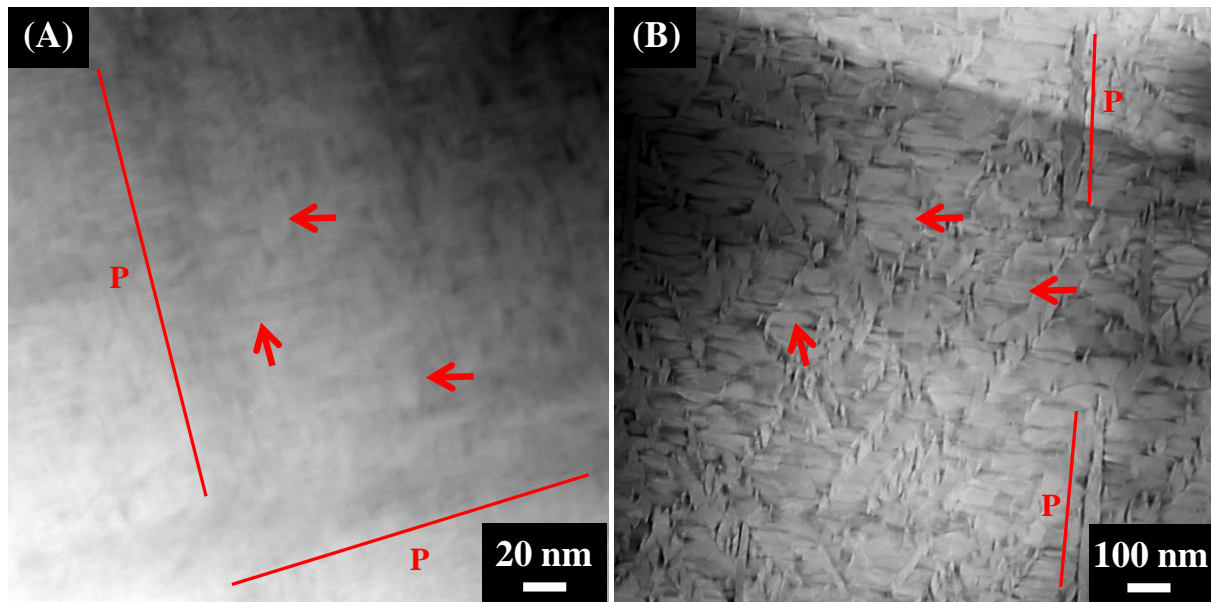


Figure 4-14 STEM-HAADF images of 1050°C/3hrs + 400°C/1000hrs foil (A) and 1050°C/3hrs + 550°C/96hrs foil (B). The label “P” indicates platelet. Arrows indicate small PPTs.

Four points from different bright precipitates and 2 points from a dark platelet were analyzed, shown in Figure 4-15. Compositional results are presented in Table 4-2. Results of the TEM-EDS revealed that the dark platelet had an average composition similar to a stoichiometry of Ti_2Au with a small amount of Ni substituting for Au. This is interesting, since the Ti-Au binary phase diagram does not contain a Ti_2Au phase, only a Ti_3Au phase [37,38]. However, it is well known that Ti_2X type phases can form in the Ti-Cu and Ti-Ag binary systems, where Cu and Ag share a similar valance with Au. The TEM-EDS results of the bright

precipitation reveals a stoichiometry near $(\text{Au,Ni})_4\text{Ti}_3$, which is similar to the Ni_4Ti_3 type precipitation found in Ni-rich, Ni-Ti binary alloys and proposed in the as-cast microstructure [3-5]. However, there is no reference for a Au_4Ti_3 phase in the binary Ti-Au system.

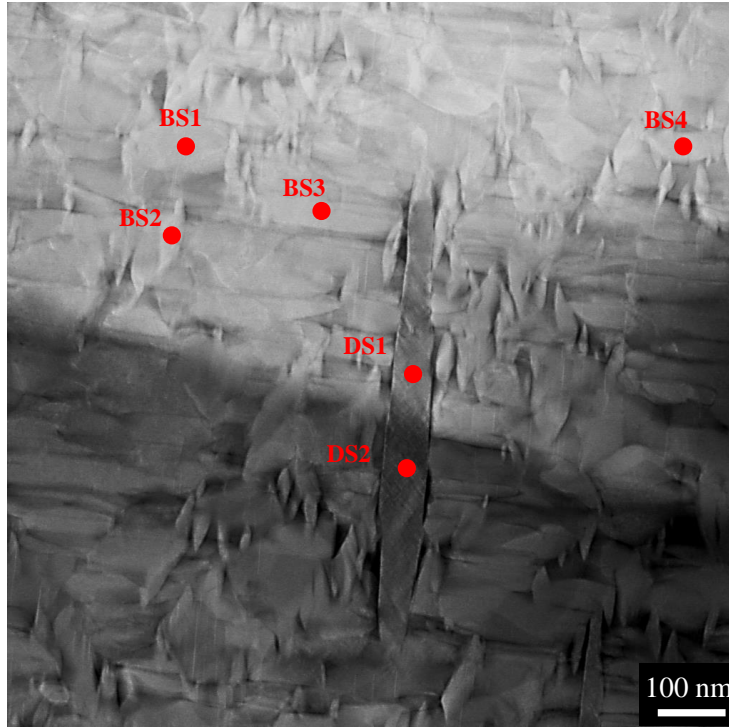


Figure 4-15 STEM-HAADF images of 96 hr 550°C foil with EDS point scan locations labeled. The label “BS” indicates bright spot and “DS” indicates dark spot.

Table 4-2 TEM-EDS Composition Values for Bright (BS) and Dark (DS) Precipitates

Region	Ti K (at %)	Ni K (at %)	Au L (at %)
BS1	41.66	24.05	34.29
BS2	41.15	24.91	33.94
BS3	41.56	25.33	33.11
BS4	40.93	25.32	33.75
DS1	66.32	0.47	33.21
DS2	64.93	1.10	33.98

Further STEM-HAADF imaging was done on the (1050°C/3hrs + 550°C/192hrs) sample. The microstructure was similar to the (1050°C/3hrs + 550°C/96hrs) foil, but further coarsening of the $(\text{Au,Ni})_4\text{Ti}_3$ type precipitates occurred. There was also a larger variation in dark platelet

size. TEM-EDS of both the dark and bright precipitates resulted in compositions consistent with those from the 550°C/96hrs sample. Again, the dark platelets shared a $Ti_2(Au,Ni)$ type stoichiometry while the bright precipitates resembled a $(Au,Ni)_4Ti_3$ type.

The (1050°C/3hrs + 550°C/192hrs) foil also contained several $Ti_2(Au,Ni)$ type platelets at oblique angles, which allowed for selected area electron diffraction. Therefore, a dark platelet was selected and the composition was verified via TEM-EDS. The composition was consistent with previous results with a value of 64.93 at % Ti – 0.99 at % Ni – 34.07 at % Au, which again correlates to the $Ti_2(Ni,Au)$. This particular platelet is shown in Figure 4-16. SADPs were then taken at two zone axes of the dark platelet. In order to compare with similar phases, Ti_2Ag , with lattice parameters $a = 0.295$ nm and $c = 1.185$ nm, was created in Crystal MakerTM and electron diffraction patterns were simulated and referenced via Single CrystalTM [29,30,39]. It is important to note that Ti_2Cu and Ti_2Ag both exhibit a tetragonal symmetry with $I4/mmm$ space group [39-42]. Thus, it is hypothesized that the $Ti_2(Ni,Au)$ type platelets may also have this symmetry.

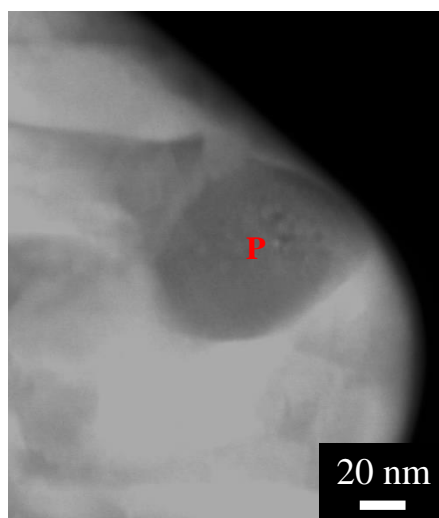


Figure 4-16 STEM-HAADF images of 1050°C/3hrs + 550°C/192hrs foil showing oblique angle of dark plate. The label “P” indicates platelet.

For each of the two platelet zone axes, the corresponding experimental α and β tilts were recorded. The SADPs are shown in Figure 4-17 along with their respective matching zone from the simulated Ti_2Ag (I4/mmm) electron diffraction patterns. The two experimental SADPs were matched to simulated electron diffraction patterns from a Ti_2Ag (I4/mmm) crystal. Zone 1, Figure 4-17 (A), matched well to $[071]_{\text{Ti}_2\text{Ag}}$, with an experimental α and β tilt of -3.42° and -3.46° , respectively. Zone 2, Figure 4-17 (C), matched closely to $[-27-1]_{\text{Ti}_2\text{Ag}}$, with an experimental α and β tilt of -14.02° and -21.83° , respectively. The experimental angle between Zone 1 and Zone 2 was calculated to be 21.21° . This is quite similar to the calculated theoretical angle between the $[071]_{\text{Ti}_2\text{Ag}}$ and $[-27-1]_{\text{Ti}_2\text{Ag}}$ of 22.52° . The small deviation in angle may be due to the difference in lattice parameters when considering Au with some solubility of Ni, in comparison to pure Ag. Changes of the c/a ratio in the tetragonal unit cell can cause variations in the angles between specific directions.

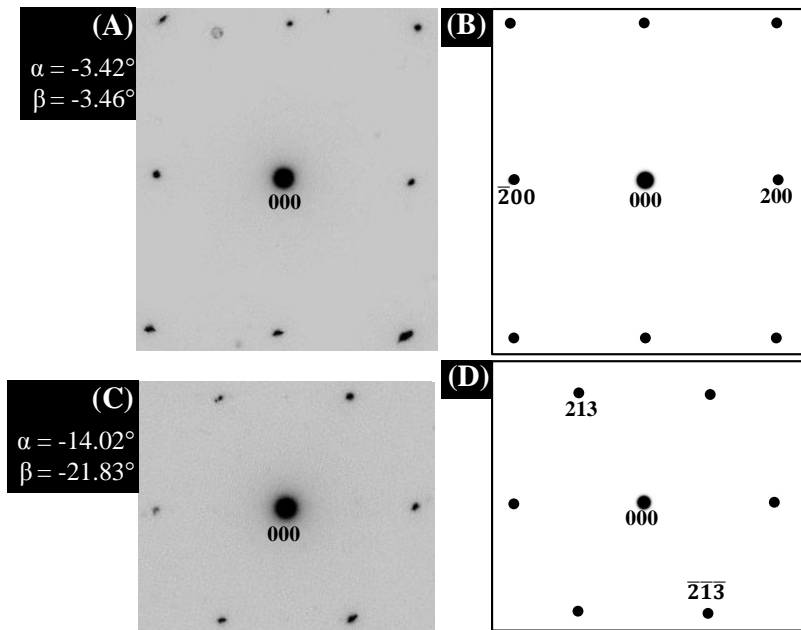


Figure 4-17 SADPs of (1050°C/3hrs + 550°C/192hrs) foil showing two zones from a dark platelet with their corresponding α and β tilts (A) and (C). The $[071]$ and $[-27-1]$ Ti_2Ag (I4/mmm) simulated SADPs are shown in (B) and (D), respectively.

4.3.4 Atom Probe Tomography Results

Three dimensional atom probe tomography (3DAP) was used to verify the compositional chemistry of precipitation in the **Au25** alloy. Atom probe tips of select 400°C aged conditions were fabricated via in-situ lift-out method of preparing atom probe samples [31]. The specific specimens examined were the (1050°C/3hrs + 400°C/48hrs) peak aged and (1050°C/3hrs + 400°C/168hrs) over-aged cases. As a reference, the 1050°C/3hrs solution annealed case was also analyzed. The results that follow will be presented by data sets from each ageing condition that are representative of all collected data of that kind. It is important to note that all data that was reconstructed and analyzed met the criterion of greater than 10 million ions and greater than 70 % golden hits.

Each tip was analyzed via iso-concentration surface, aka “iso-surface”, analysis. An iso-surface of a particular element allows the user to view a three dimensional representation of a given concentration. IVASTM software then allows the user to vary the surface composition while displaying the 3D result in real time [32]. It also has the ability to fit this iso-surface between large compositional gradients within a specific volume. In other words, users can set an interface at the compositional gradient between the matrix and any precipitation in order to calculate the compositions of either phase. This methodology was employed in an effort to capture and obtain both precipitate compositions.

The data reconstructions of the 1050°C/3hrs solution annealed specimen revealed an experimentally ranged bulk composition consistent with that predicted via EMP-WDS, as shown in Table 4-3. The color code denoted in Table 4-3 will be followed throughout the rest of this proceeding. Ti is associated with black, Ni with green, and Au with red. This will aid in distinguishing constituent elements during 3DAP analysis.

Table 4-3 3DAP and EMP-WDS Bulk **Au25** Compositions for 1050°C/3hrs sample

Element	Ranged Composition (at %)	EMP-WDS Composition (at %)	Color Code
Ti	48.62 ± 0.03	48.94 ± 0.23	
Ni	26.43 ± 0.03	26.42 ± 0.41	
Au	24.95 ± 0.02	24.64 ± 0.38	

All reconstructions were performed using a tip-shank fitting technique, as shown in Figure 4-18. Tip volumes were typically on the order of 80 nm³ or less, as shown in Figure 4-18 (A). SE micrographs of each tip were fitted within IVASTM by setting markers down the tip shank to allow the software to estimate tip shank angle and profile for reconstructions, Figure 4-18 (B). Iso-concentration surface analysis did not reveal any distinct compositional gradients within the tip volume. This would suggest that no precipitation was captured in the 1050°C/3hrs tips.

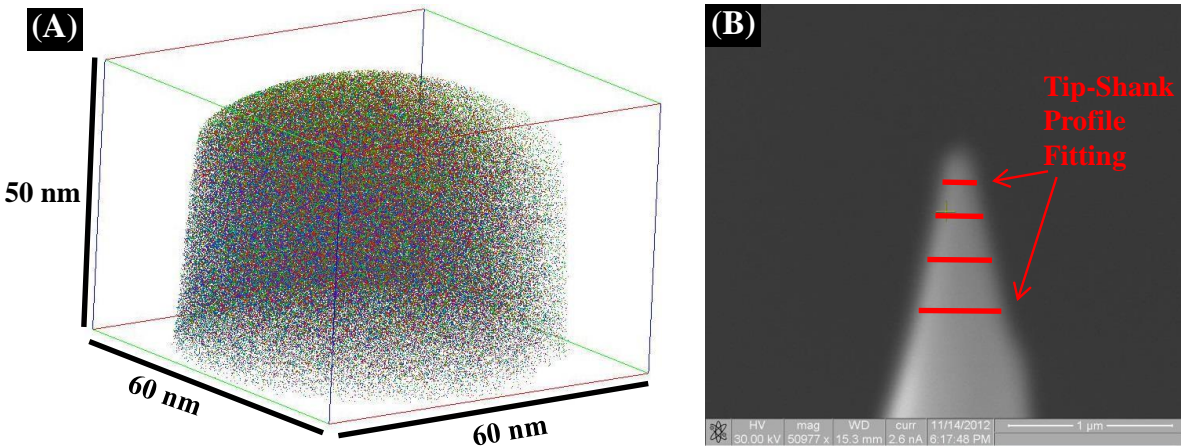


Figure 4-18 3DAP reconstruction ion map of 1050°C/3hrs **Au25** specimen (A) and SE micrograph of the actual tip geometry with tip-shank fitting emphasized (B).

The homogeneity of the tip volume is depicted in Figure 4-19, where a 24.95 at % Au iso-surface (A) and a 26.43 at % Ni iso-surface (B) are shown. These two iso-surfaces represent the bulk composition of both Au and Ni. Even though precipitation was not found in the 1050°C/3hr **Au25** tips, ranged bulk compositions were consistent with EMP-WDS results.

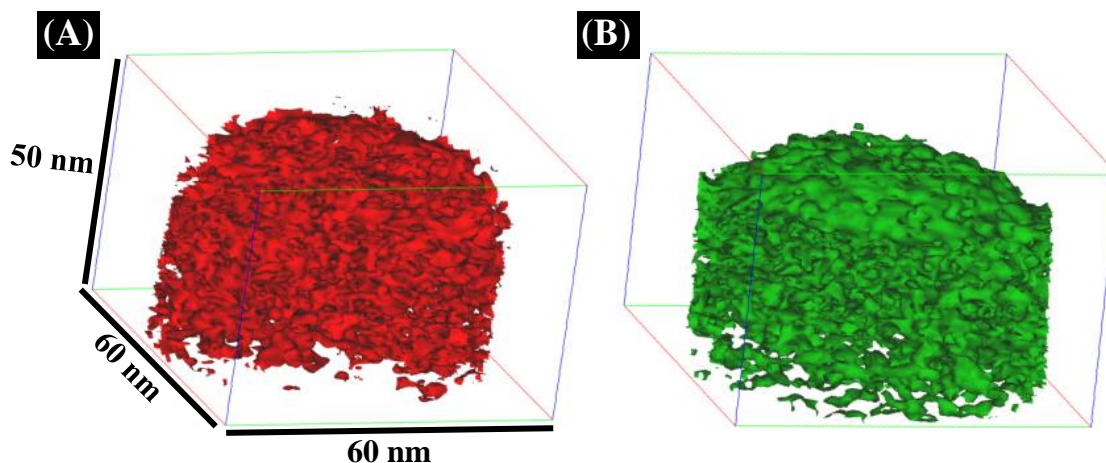


Figure 4-19 3DAP 24.95 at % Au iso-surface (A) and 26.43 at % Ni iso-surface (B) of the 1050°C/3hr **Au25** specimen.

Atom probe reconstructions of the (1050°C/3hrs + 400°C/48hrs) tips were also fitted with SE images via tip-shank profile fitting. The ranged compositions were consistent with the WDS average composition, as shown in Table 4-4. Compositional phase analysis was carried out with a Ti iso-concentration surface. A concentration gradient within the tip volume was found and a 46.30 at % Ti iso-surface was fitted to the gradient center, shown in Figure 4-20. Again, this allows for computation of the average composition on either side of the concentration gradient. However, it is at the discretion of the user to decide which region constitutes matrix and which is precipitate. For this particular concentration gradient, the low side (precipitate) and high side (matrix) compositions were computed, shown in Table 4-5.

Table 4-4 Average 3DAP and EMP-WDS Bulk **Au25** Compositions aged 400°C/48hrs

Element	Ranged Composition (at %)	EMP-WDS Composition (at %)	Color Code
Ti	48.48 ± 0.02	48.94 ± 0.23	Black
Ni	26.25 ± 0.03	26.42 ± 0.41	Green
Au	25.27 ± 0.03	24.64 ± 0.38	Red

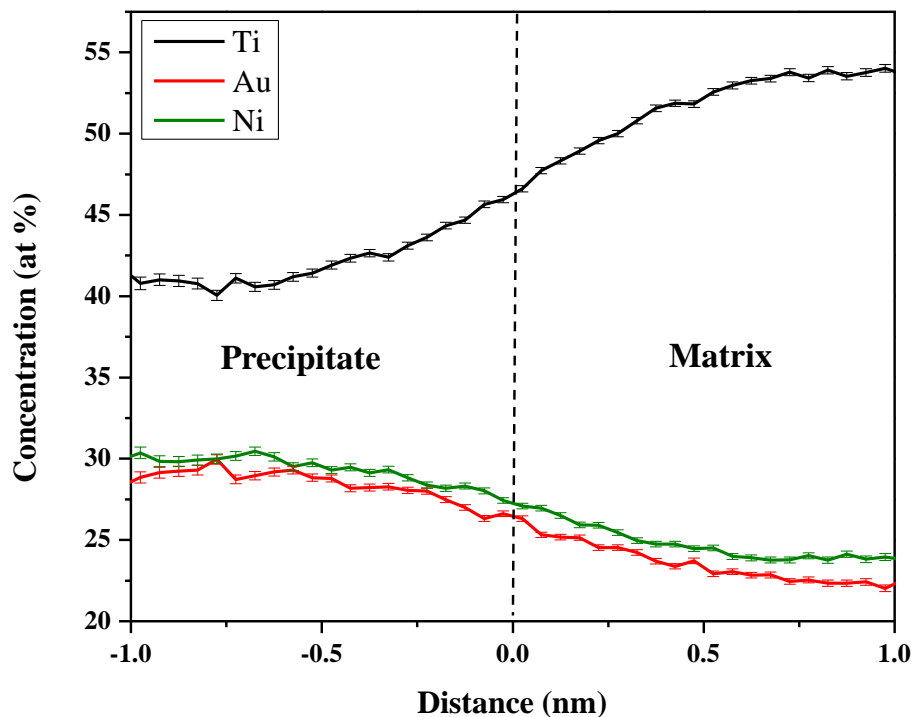


Figure 4-20 Concentration gradient from 1050°C/3hrs + 400°C/48hrs 3DAP data reconstruction centered on 46.30 at % Ti. The sides corresponding to precipitate and matrix are labeled.

Table 4-5 Average Precipitate and Matrix Composition from a 48 hr 400°C Reconstruction Centered on a 46.30 at % Ti Iso-surface.

Region	Ti (at %)	Ni (at %)	Au (at %)
Precipitate	42.68 ± 0.49	29.09 ± 0.47	28.23 ± 0.29
Matrix	51.93 ± 0.05	24.91 ± 0.04	23.15 ± 0.03

The left side of the concentration gradient was considered precipitation because it had a composition consistent with the $(\text{Au,Ni})_4\text{Ti}_3$ stoichiometry found via TEM-EDS. However, it is interesting to note that 3DAP results indicate nearly equal amounts of Au and Ni in the $(\text{Au,Ni})_4\text{Ti}_3$ phase, but TEM-EDS results revealed a slightly Au-rich phase. The matrix phase was Ti-rich, which is what would be expected locally around a Au/Ni-rich phase.

In order to visualize the $(\text{Au,Ni})_4\text{Ti}_3$ precipitates, Ni iso-surfaces were created using both the concentration of Ni in the precipitation and the concentration of Ni in the matrix, shown in Figure 4-21. The 29.09 at % Ni precipitate surface clearly depicts small precipitates that are consistent in morphology and size to TEM results, Figure 4-21 (A). In contrast, the 24.91 at % Ni matrix surface depicts a more homogeneous distribution, which would be expected of the matrix phase in this case, Figure 4-21 (B).

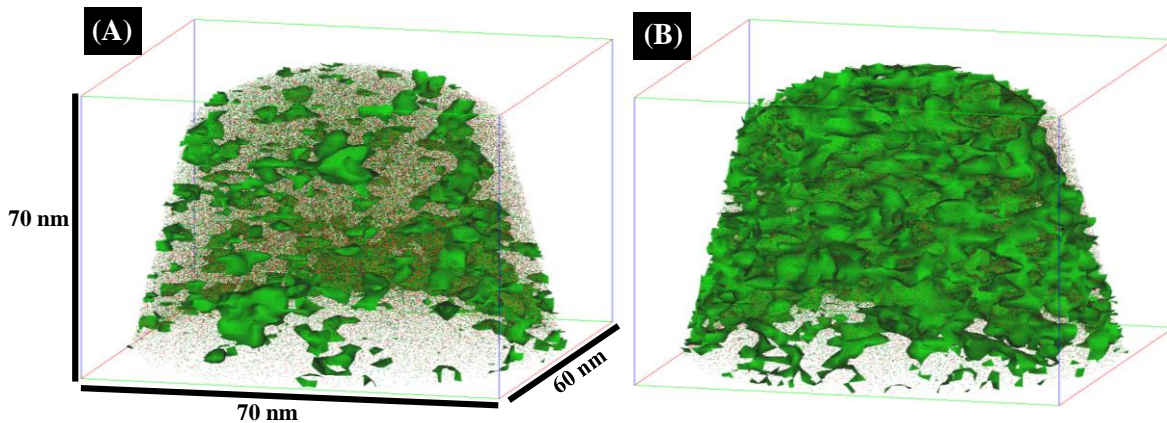


Figure 4-21 48 hr 400°C 3DAP reconstruction depicting a 29.09 at % Ni precipitate surface (A) and a 24.91 at % Ni Matrix surface (B).

It is interesting to note that even though only one precipitate type was evident in the (1050°C/3hrs + 400°C/48hrs) TEM results, another Ti-rich phase was discovered with atom probe tomography using a Ni-iso-surface of 23.25 at %. This Ni iso-surface was centered on a large concentration gradient, as shown in Figure 4-22. For this particular concentration gradient, the low side (precipitate) and high side (matrix) compositions were also computed, shown in Table 4-6.

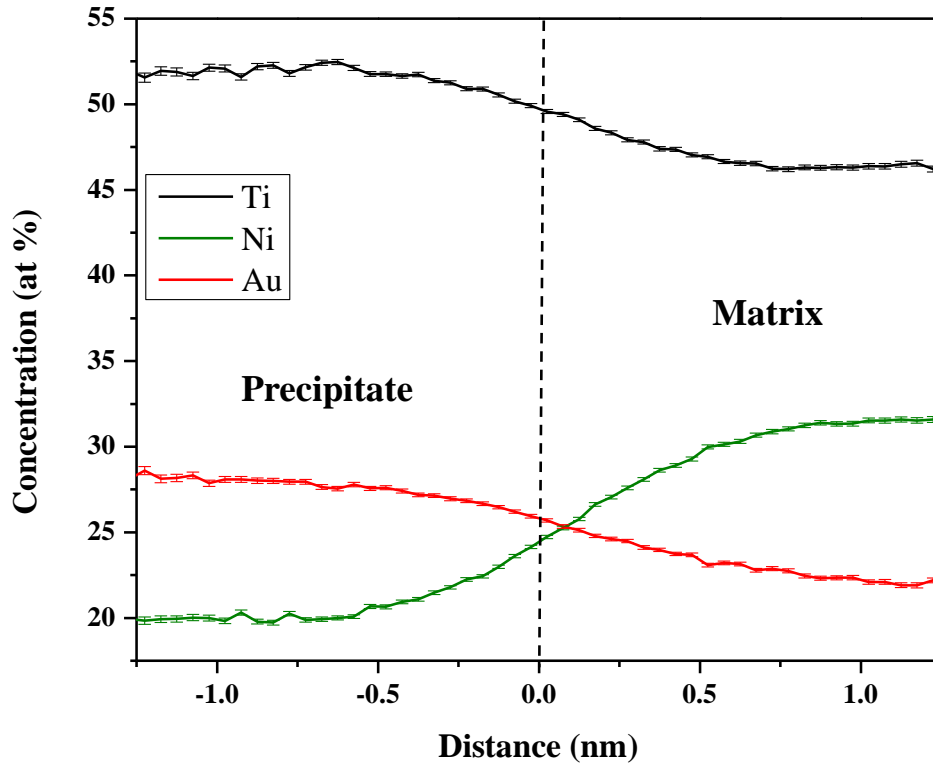


Figure 4-22 Concentration gradient from 1050°C/3hrs + 400°C/48hrs 3DAP data reconstruction centered on 23.25 at % Ni. The sides corresponding to precipitate and matrix are labeled.

Table 4-6 Average Precipitate and Matrix Composition from a 1050°C/3hrs + 400°C/48hrs Reconstruction Centered on a 23.25 at % Ni Iso-surface.

Region	Ti (at %)	Ni (at %)	Au (at %)
Precipitate	53.15 ± 0.87	20.40 ± 0.75	26.45 ± 0.62
Matrix	47.16 ± 0.05	29.15 ± 0.04	23.69 ± 0.04

The results indicated a Ti-rich precipitate phase with a Ni-rich matrix. It is interesting to note that the average precipitate composition is similar to the TEM-EDS results of the 550°C samples. However, there appears to be excess Ni and in place of Ti for the atom probe compositions. The precipitation is depicted in Figure 4-23 with a Ni-isosurface of 20.40 at %. There were clearly various size precipitates that exhibited plate-like morphology, analogous to TEM results on further aged specimens. In order to compare the compositions of the two

different sized precipitates, mass spectrum calculations were performed within each of the two precipitate surfaces. This allowed for calculation of each precipitate composition. For the large platelet, emphasized in Figure 4-21 (B), the composition was 53.08 at % Ti – 16.66 at % Ni – 30.25 at % Au. Another platelet was also analyzed for composition, Figure 4-24. The composition of this platelet was determined to be 65.51 at % Ti – 7.55 at % Ni – 26.95 at % Au. This chemistry is more consistent with the TEM-EDS results of the $Ti_2(Ni,Au)$ type precipitation found in the 400°C/168hr foils. However, a slightly higher concentration of Ni was detected via 3DAP. A cylindrical 1-D concentration profile through the smaller precipitate, normal to the flat platelet face, revealed enrichment in Ti and depletion in Ni, shown in Figure 4-25. It is important to note that only one of the 400°C/48hr data sets contained this additional Ti-rich precipitation, but the (Au,Ni) rich phase was found in all data sets.

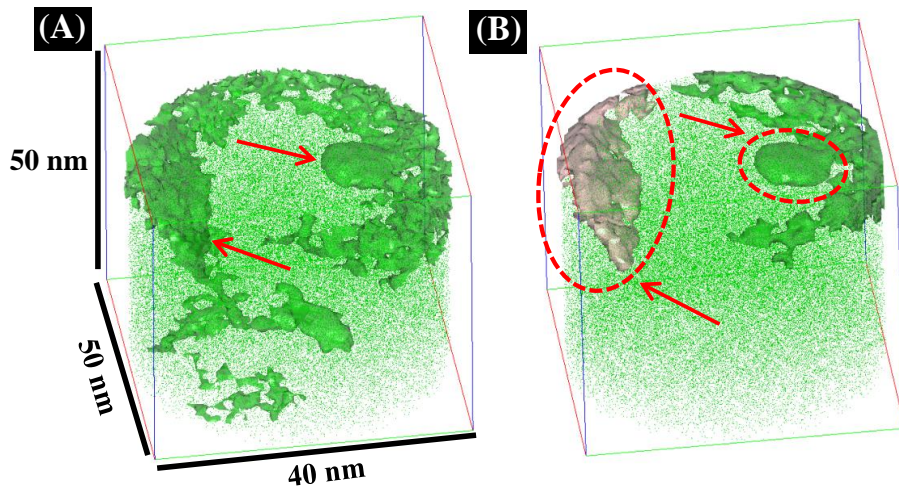


Figure 4-23 400°C/48hr 3DAP reconstruction depicting a 20.40 at % Ni precipitate surface (A) and polygon filtered image with a large platelet emphasized (B). Arrows signify the two particular platelets discussed in the text.

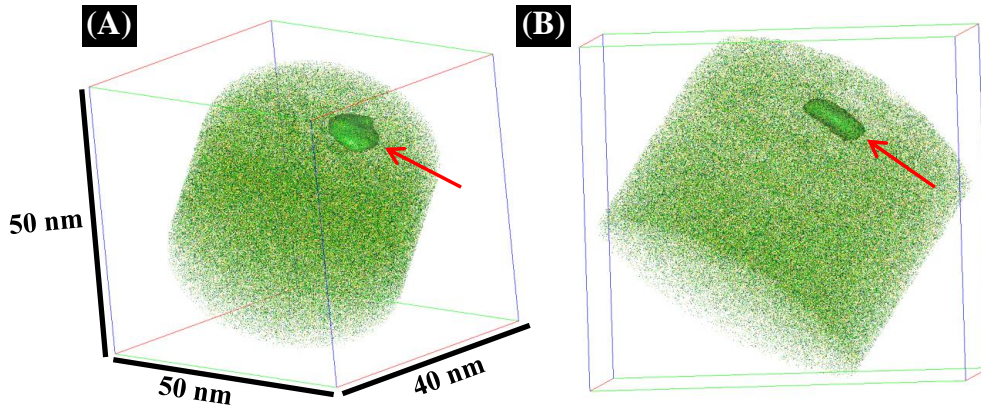


Figure 4-24 400°C/48hr 3DAP reconstruction depicting polygon filtered image consisting of a 20.40 at % Ni precipitate surface (A) with alternate side view (B).

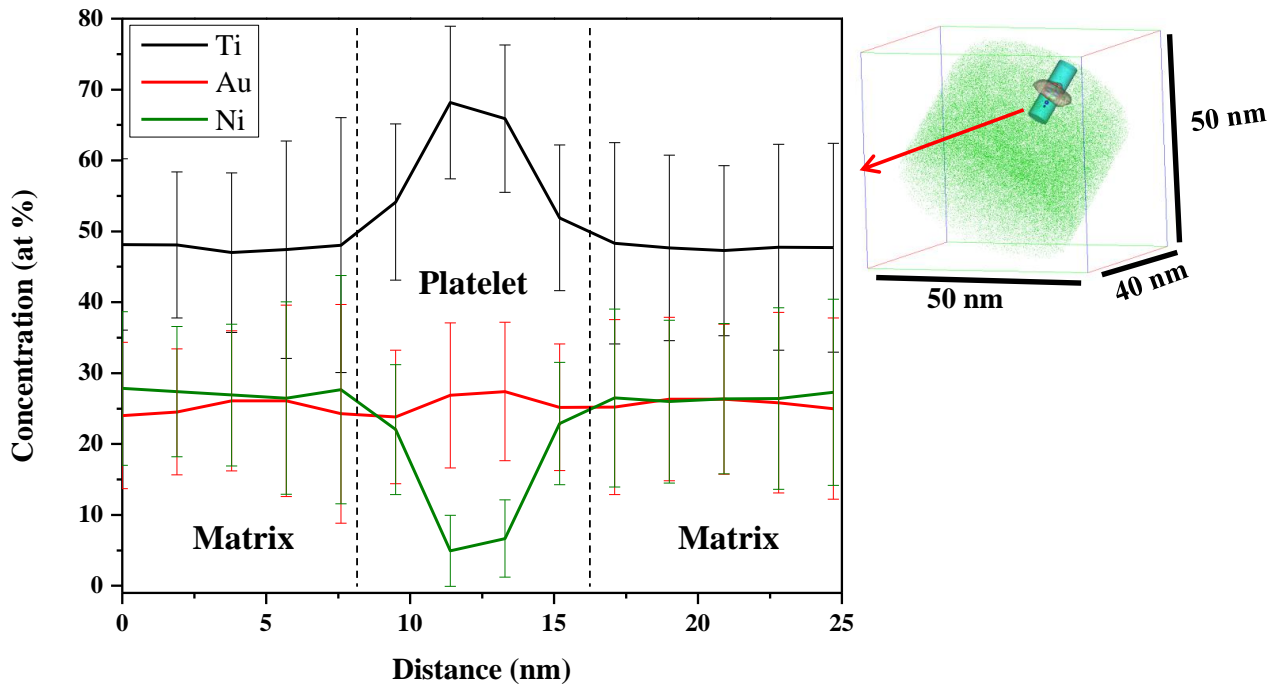


Figure 4-25 1-D cylindrical concentration profile through a $Ti_2(Ni,Au)$ platelet in 400°C/48hr data set. Regions of matrix and platelet composition are labeled. The profile is taken normal to the largest surface area of the platelet.

3DAP reconstructions were also done for the (1050°C/3hrs + 400°C/168hrs) specimens.

Data sets were again reconstructed via tip-shank profile fitting from a SE micrograph of each tip.

The average ranged compositions were consistent with EMP-WDS results, as depicted in Table 4-7. Compositional phase analysis was performed using a Ti iso-concentration surface. This surface was centered at 46.80 at % Ti on a large concentration gradient, as shown in Figure 4-26. The results were analogous to the 400°C/48hrs 3DAP results, in that the low side consisted of precipitation and the high side was considered matrix. The average precipitate and matrix compositions from each side of the concentration gradient were computed, as shown in Table 4-8. The precipitation was consistent with the $(\text{Au,Ni})_4\text{Ti}_3$ type precipitation found in previously discussed results. The matrix was slightly Ti-rich, which is expected locally near these types of precipitates.

Table 4-7 Average 3DAP and EMP-WDS Bulk Au25 Compositions for 400°C/168hrs

Element	Ranged Composition (at %)	EMP-WDS Composition (at %)	Color Code
Ti	48.87 ± 0.02	48.94 ± 0.23	
Ni	26.25 ± 0.02	26.42 ± 0.41	
Au	24.88 ± 0.03	24.64 ± 0.38	

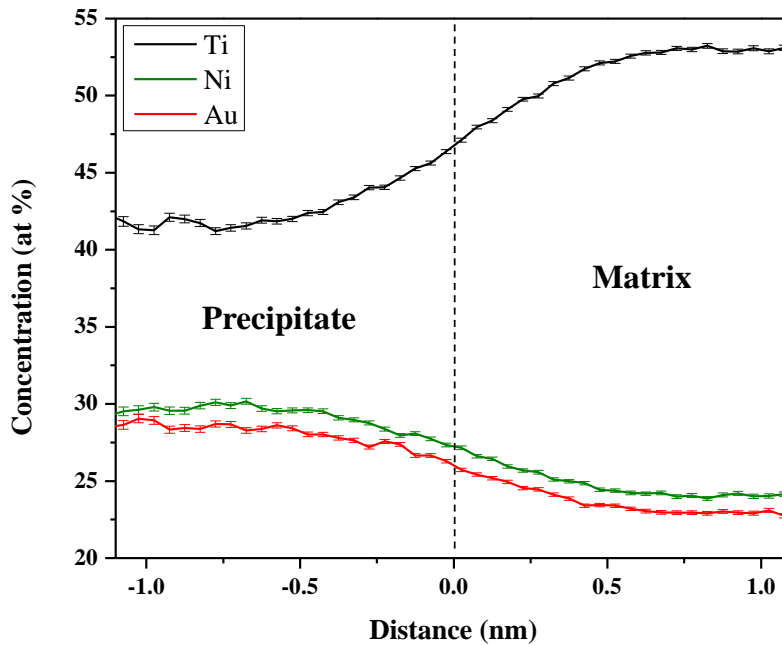


Figure 4-26 Concentration gradient from 400°C/168hrs 3DAP data reconstruction centered on 46.80 at % Ti. The sides corresponding to precipitate and matrix are labeled.

Table 4-8 Average Precipitate and Matrix Composition from a 400°C/48hr Reconstruction Centered on a 46.30 at % Ti Iso-surface.

Region	Ti (at %)	Ni (at %)	Au (at %)
Precipitate	42.58 ± 0.44	29.27 ± 0.37	28.15 ± 0.41
Matrix	51.64 ± 0.04	25.02 ± 0.05	23.33 ± 0.03

Further analysis of the 400°C/168hr data using a Ni-isosurface revealed the presence of additional Ti-rich precipitates, similar to the 48 hr 400°C data. A 24.50 at % Ni iso-surface was centered on the large concentration gradient. The average precipitate and matrix compositions were calculated, as shown in Table 4-9. The precipitates were similar to those found in 400°C/48hr data sets, but compositionally they were again much leaner in Ti and richer in Ni. However, their size and morphology is consistent with TEM results, as shown in Figure 4-27. The 21.25 at % Ni-isosurface clearly depicts two large platelets. In order to view the platelets more clearly, a filtered polygon image, where particles smaller than a particular size were removed, as shown in Figure 4-26 (B).

Table 4-9 Average Precipitate and Matrix Composition from a 400°C/168hr Reconstruction Centered on a 24.30 at % Ni Iso-surface.

Region	Ti (at %)	Ni (at %)	Au (at %)
Precipitate	51.44 ± 0.24	21.25 ± 0.21	27.32 ± 0.29
Matrix	47.16 ± 0.03	29.61 ± 0.04	23.24 ± 0.04

It is hypothesized that the variation in platelet chemistry may be due to the metastable nature of the Ti-rich precipitation. It is plausible to suggest the notion of multi-stage transformation during ageing. This could explain why all of the TEM-EDS data for the 550°C specimens consisted of only a Ti₂(Ni,Au) type stoichiometry. At the higher temperature, the Ti-

rich platelets may readily undergo several transformation steps, while at 400°C such processes may be slowed. This could explain the presence of a varying chemistry in the 400°C 3DAP data.

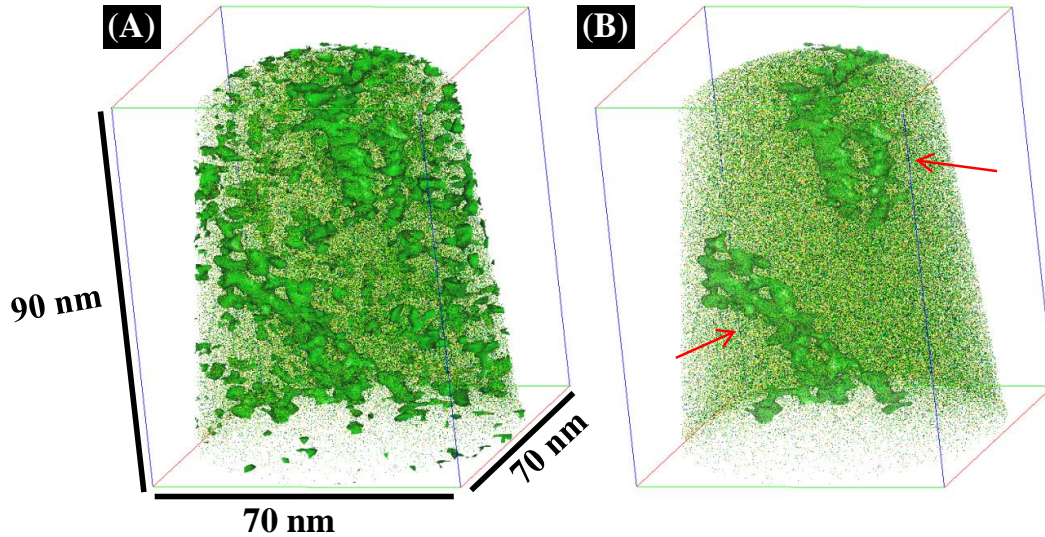


Figure 4-27 400°C/168hr 3DAP reconstruction depicting a 21.25 at % Ni precipitate surface (A) with 1000 polygon filtered image (B). Arrows indicate two large platelets.

4.3.5 XRD Results

In order to examine the crystallography of the **Au₂₅** precipitation, XRD was done using Cu-K α radiation on bulk specimens. A comparison of XRD spectra for the solution annealed and selected 400°C aged samples is shown in Figure 4-28. The B2 peaks are labeled along with Ti₂Pd as a reference. This phase was used in place of Ti₂Ag since an indexed XRD data card was not available. However, Ti₂Pd has the same I4/mmm space group as Ti₂Ag and Pd has a similar atomic radii to Au and Ag [43]. It is interesting to note the peak evolution during ageing at 400°C. Most of the additional peaks, not associated with the B2 matrix, tend to lie in Ti₂Pd peak positions. This could indicate that the Ti-rich platelets found via TEM in the 400°C specimens also have the tetragonal I4/mmm symmetry. It is then hypothesized that the unidentified peaks in Figure 4-28 not identified as matrix or Ti₂Pd correlate to the (Au,Ni)₄Ti₃ type precipitates discussed in the previous sections. This will be addressed in greater detail in

the discussion section. Only relevant Ti_2Pd peaks were identified, and additional peaks were listed on the reference card.

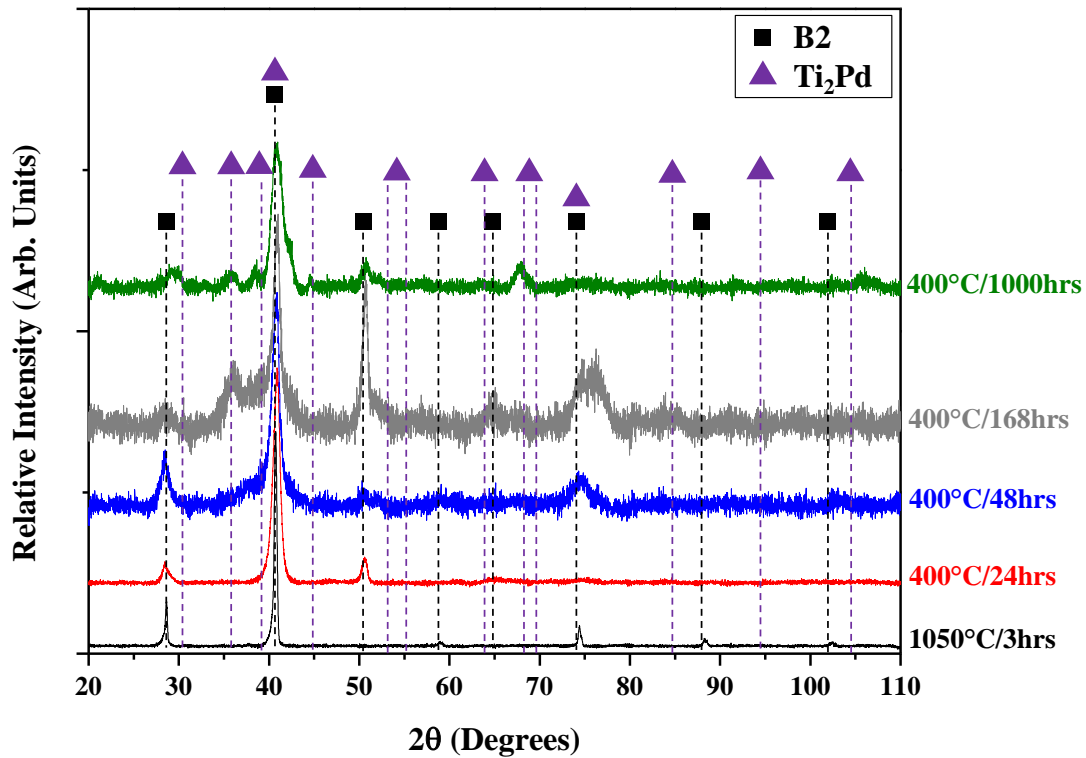


Figure 4-28 XRD spectra of the 400°C heat treated **Au₂₅** specimens using Cu-K α radiation. The B2 matrix and Ti_2Pd (I4/mmm) peaks are identified. All identified peaks are thought to correlate to $(Au,Ni)_4Ti_3$ (see discussion section).

This same methodology was applied to the 550°C XRD data as well, as shown in Figure 4-29. However, in this case it was appropriate to identify more Ti_2Pd peaks. It is interesting that all unidentified peaks in the 400°C spectra were also found in the 550°C spectra. There were also more peaks associated with the Ti-rich phase, as well as additional unidentified peaks. In order to clearly show the unidentified peaks thought to associate with $(Au,Ni)_4Ti_3$, XRD spectra for both over-aged cases were plotted, shown in Figure 4-30. Precipitate crystallography will be addressed further in the discussion section.

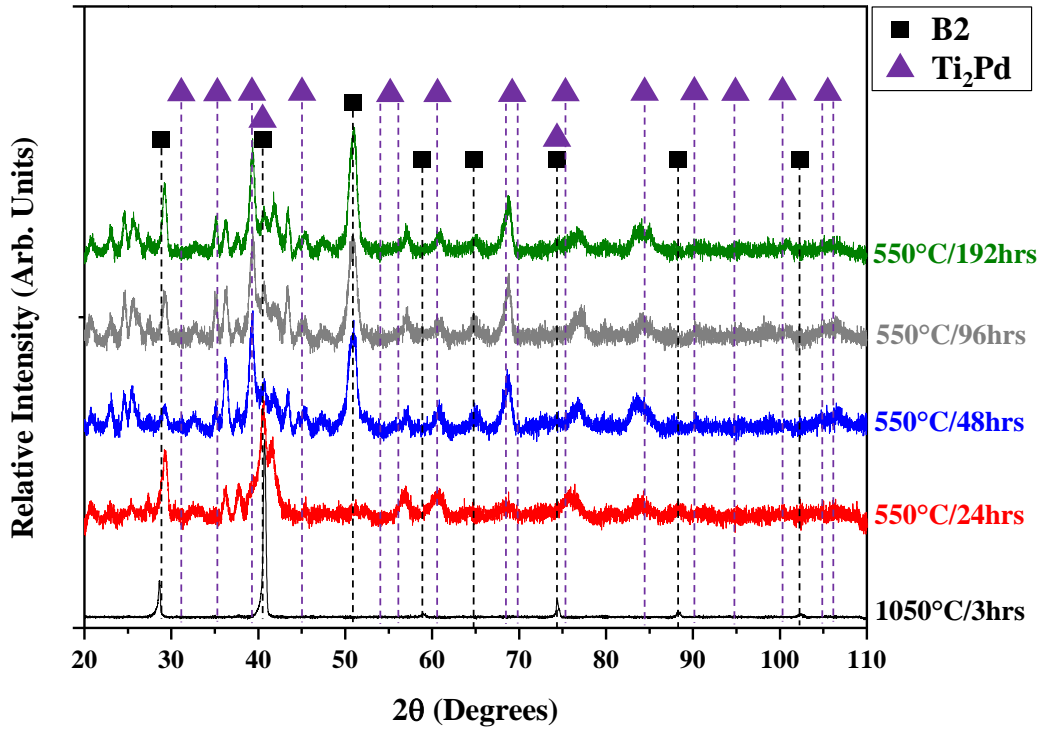


Figure 4-29 XRD spectra of the 550°C heat treated **Au₂₅** specimens using Cu-K α radiation. The B2 matrix and relevant Ti₂Pd (I4/mmm) peaks are identified. All identified peaks are thought to correlate to (Au,Ni)₄Ti₃ (See discussion section).

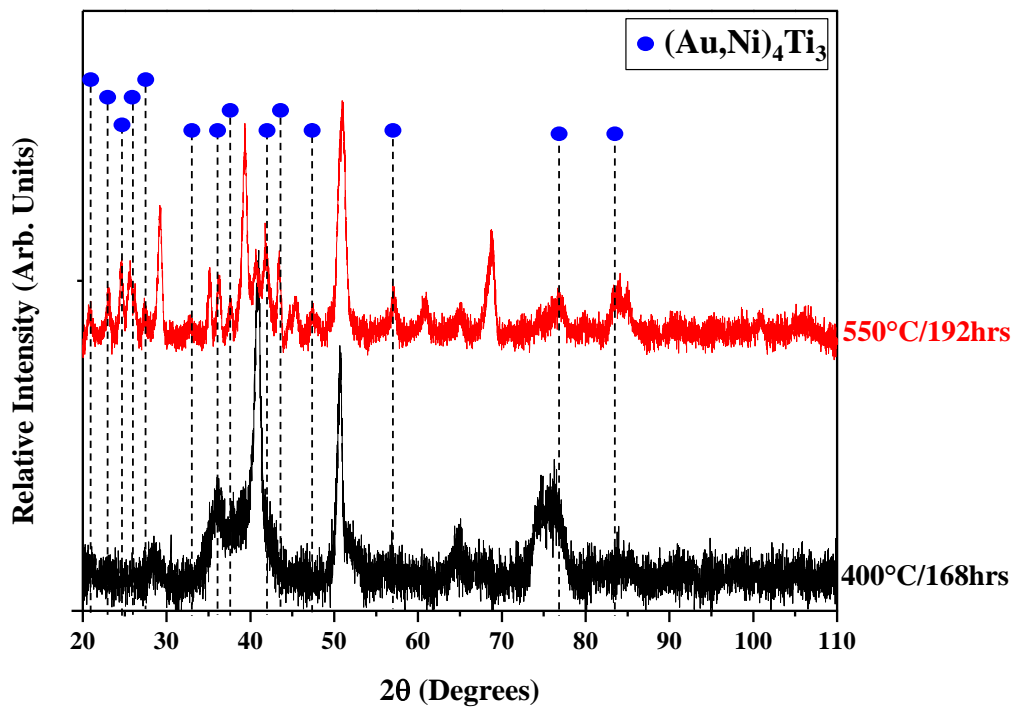


Figure 4-30 XRD spectra of the 400°C and 550°C heat treated **Au₂₅** specimens using Cu-K α radiation. Only the peaks thought to be correlated to (Au,Ni)₄Ti₃ are labeled.

4.3.6 DSC Results

Differential scanning calorimetry was performed on several 400°C and 550°C aged specimens. Also, as a reference point, DSC was done in the as-cast condition. The results of the as-cast state are shown in Figure 4-31. The as-cast DSC results indicate that the **Au25** alloy does undergo a martensitic transformation. The martensitic and austenitic temperatures were approximately 135°C and 175°C, respectively, which is quite high in comparison to other shape memory systems. However, the onset of thermal hysteresis indicates phase transformation instability.

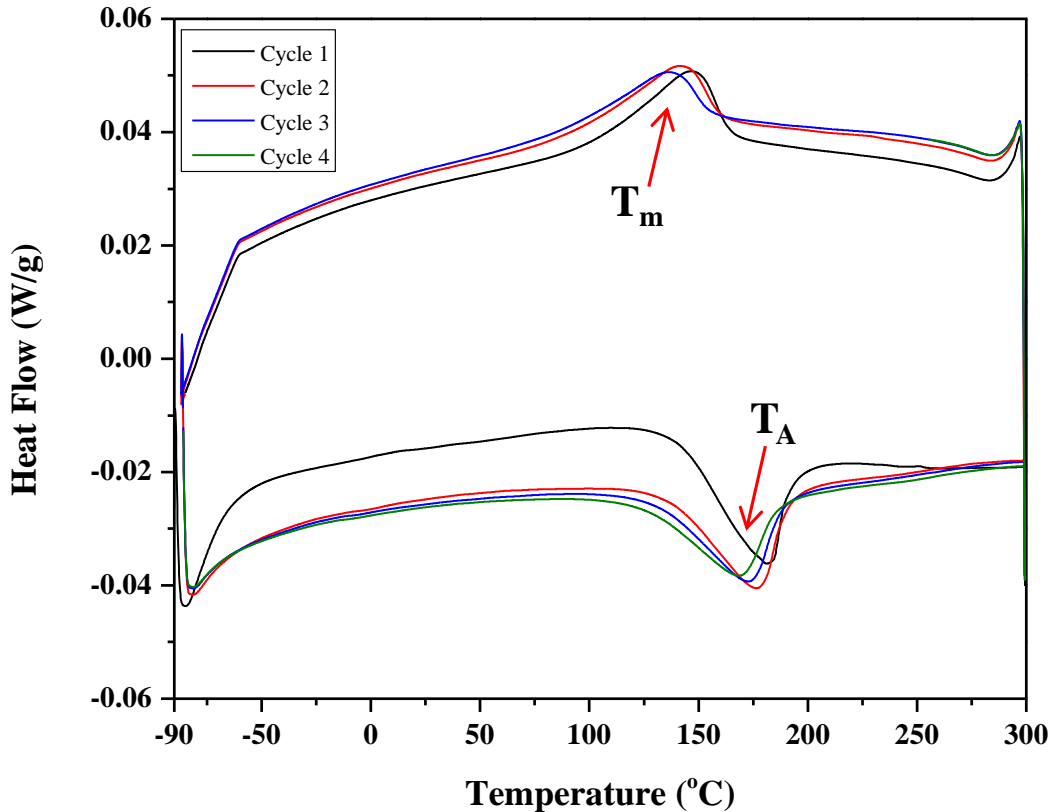


Figure 4-31 Several DSC cycles of **Au25** as-cast specimen from -90 to 300 °C. T_m and T_A labels represent martensitic transformation temperature and austenitic transformation temperature, respectively.

In order to examine the effect of precipitation on the transformation temperature and stability, DSC was performed on the peak and over-aged cases for both temperatures. For the 400°C specimens, no clear transformation peaks were detected via DSC, shown in Figure 4-32. The DSC results of the 400°C specimens did not reveal a martensitic transformation for the peak-aged 48 hr and over-aged 168 hr samples. This may suggest that the precipitation observed at 400°C may act to suppress or pin the martensite from forming upon cooling. It is also known that precipitate spacing and volume fraction may also influence transformation phenomena [44,45]. Therefore, DSC of the 1000 hr 400°C sample was also done. This was to examine the transformation behavior of a much further coarsened microstructure. However, no clear transformation peaks were observed.

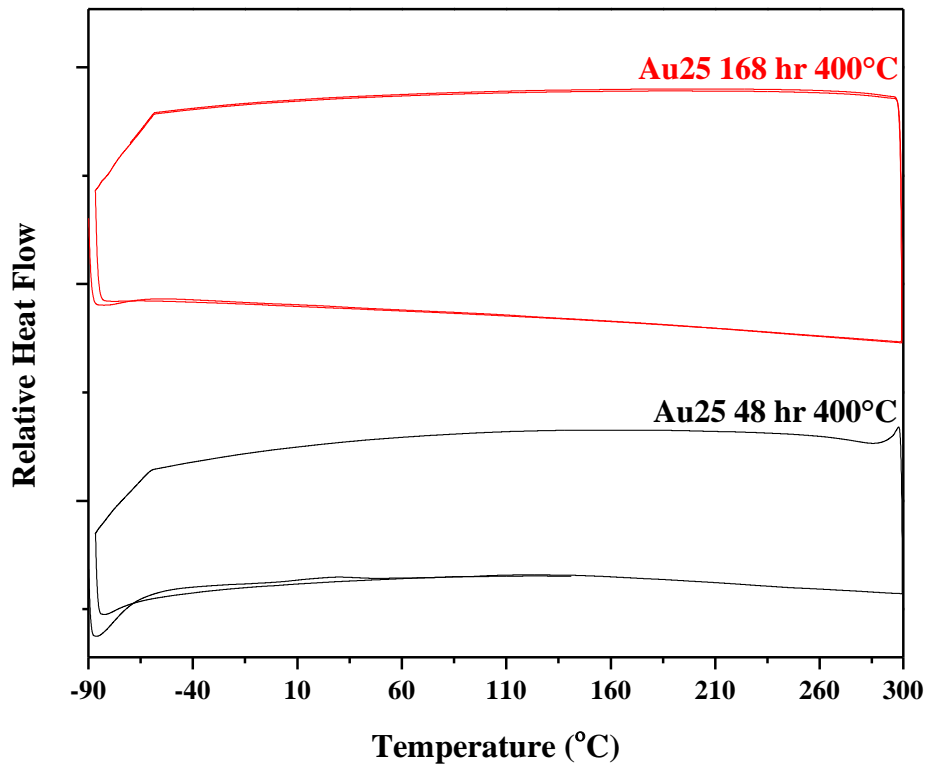


Figure 4-32 DSC cycles of 400°C peak and over-aged **Au25** specimens from -90 to 300 °C.

DSC was also performed on the 550°C peak-aged and over-aged specimens. The results are depicted in Figure 4-33. It is interesting to note that no clear transformation peaks were evident in the 550°C samples as well. However, it is hypothesized that the precipitation behavior in the 550°C samples is analogous to the 400°C samples. Thus, since no martensitic transformation was detected in the 400°C samples, it was not expected in the 550°C aged specimens.

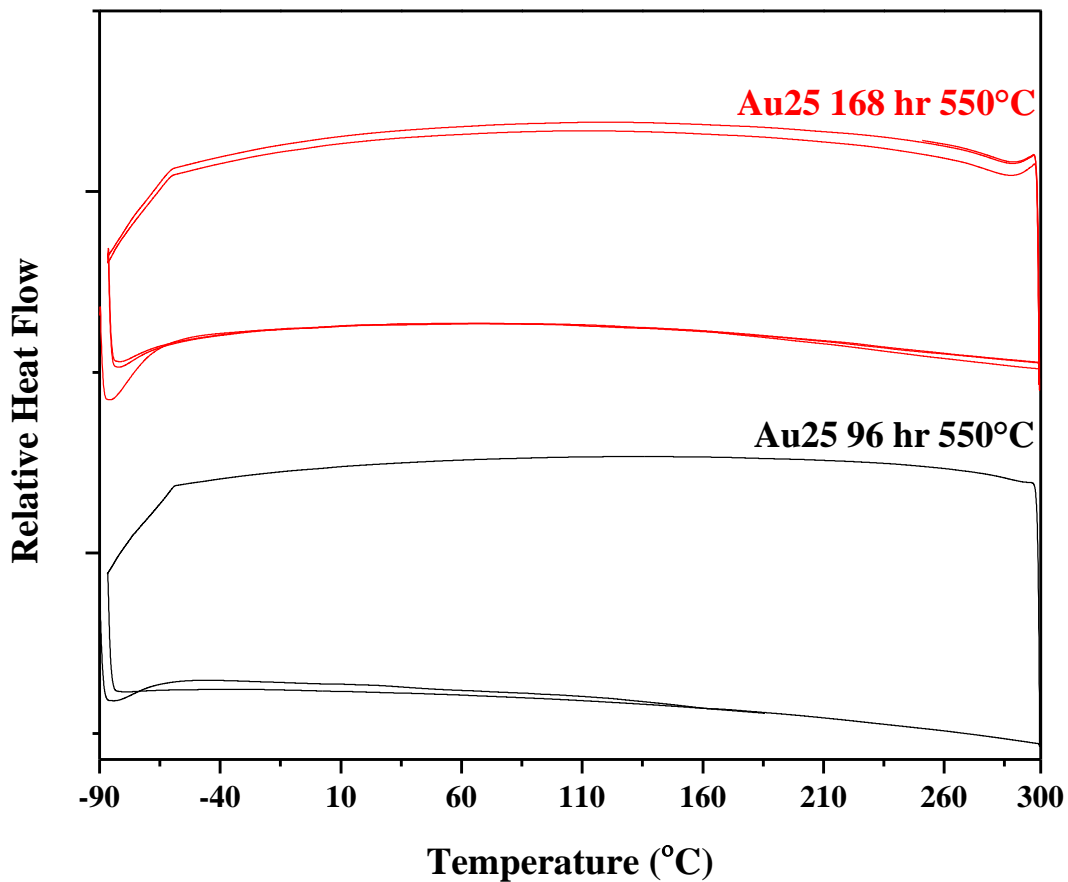


Figure 4-33 DSC cycles of 550°C peak and over-aged **Au25** specimens from -90 to 300 °C.

4.4 1050°C Furnace Cooled Microstructure and Properties

For a greater understanding of the phase equilibria in the **Au25** alloy, a specimen was also heat treated at 1050°C for 3 hrs followed by furnace cooling. The microstructure was first

examined via scanning electron microscopy, as shown in Figure 4-34. Backscatter imaging of the furnace cooled **Au25** alloy revealed a microstructure rich in bright, alternating platelets. There also appeared to be a variation in platelet size of approximately 10 μm to $< 1\mu\text{m}$ in length. It is hypothesized that the bright platelets are analogous to those found in the backscattered images of the as-cast **Au25** alloy.

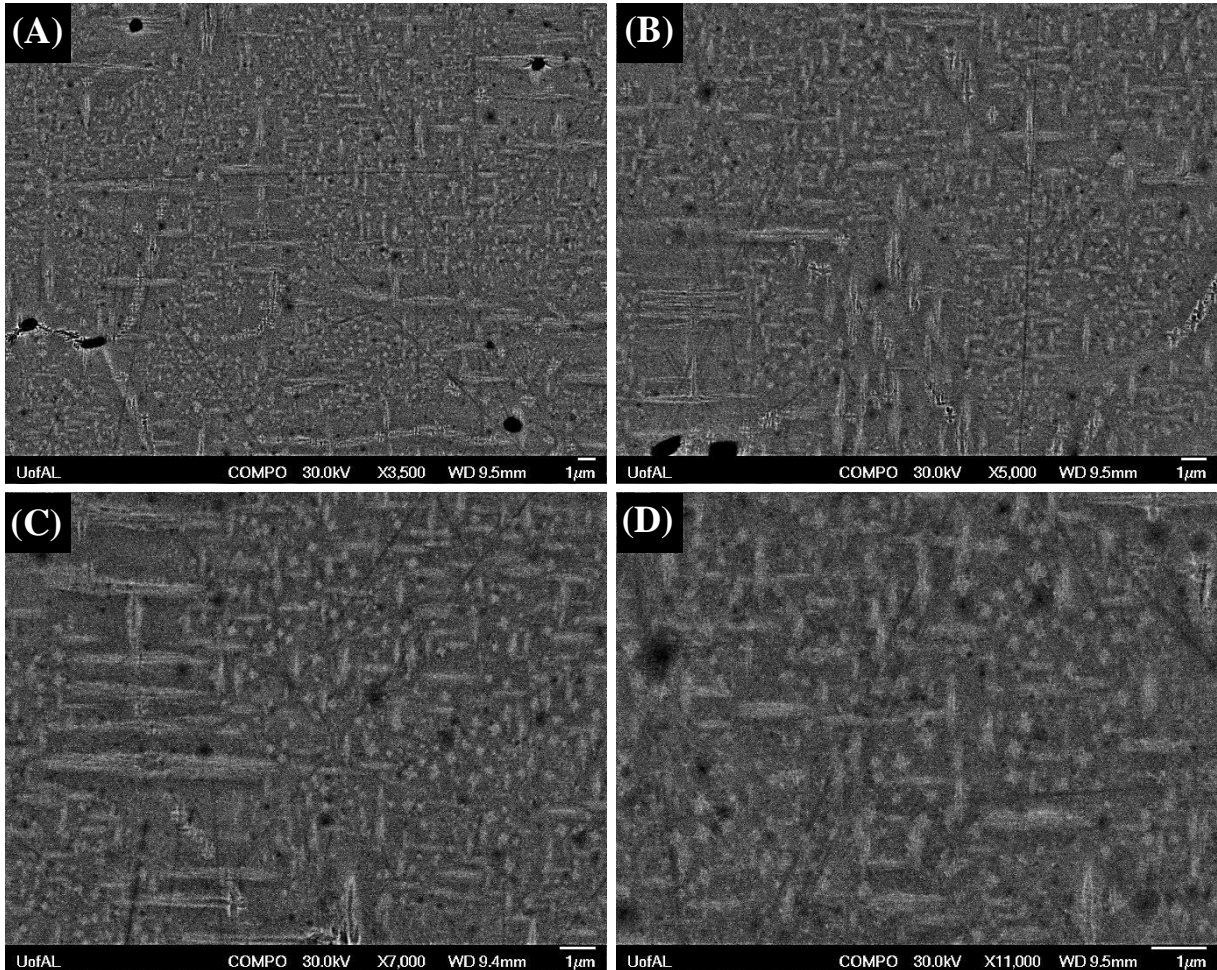


Figure 4-34 BSE images of the **Au25** 1050°C furnace cooled specimen with increasing magnification (A), (B), (C), (D), respectively.

It is thought that these precipitates correlate to the $(\text{Au,Ni})_4\text{Ti}_3$ type nano-scale precipitation found in the aged specimens. However, a chemistry difference between the matrix and platelets was not detected via EDS. The furnace cooled specimen also contained the

$\text{Ti}_4(\text{Ni,Au})_2\text{O}$ oxide inclusions discussed previously, which were verified with EDS. XRD was used to examine the crystallography of the furnace cooled microstructure. For a comparison, the furnace cooled XRD spectra was plotted along with the peak-aged 550°C specimen, as shown in Figure 4-35. For a frame of reference, the furnace cooled spectra was labeled with the B2 matrix peaks, relevant Ti_2Pd peaks, and the additional unidentified peaks that were hypothesized to correlate to the $(\text{Au,Ni})_4\text{Ti}_3$ type precipitates discussed previously. However, three additional peaks around 80 degrees were present in the furnace cooled sample, but not in the 550°C peak-aged specimen. These peaks are thought to associate with the $(\text{Au,Ni})_4\text{Ti}_3$ type precipitation, since they did not correlate to the matrix or Ti-rich platelet reference peaks and the microstructure was considerably coarsened. The furnace cooled spectra was dominated by the peaks thought to correlate with $(\text{Au,Ni})_4\text{Ti}_3$ type precipitates. This may indicate that the bright platelets detected via BSE imaging are the same bright phase found at the nano-scale in the aged specimens. Further discussion on the crystallography of the $(\text{Au,Ni})_4\text{Ti}_3$ phase will be examined in the discussion section.

The furnace cooled specimen was also subjected to DSC testing. Interestingly, the DSC scans revealed the presence of a martensitic transformation, as shown in Figure 4-36. The martensitic and austenitic transformation temperatures were approximately 160°C and 200°C , respectively. This indicates that the furnace cooled specimen exhibited a higher martensitic transformation temperature than the as-cast condition. However, the onset of thermal hysteresis again suggests transformation instability. This will be addressed further in the discussions section.

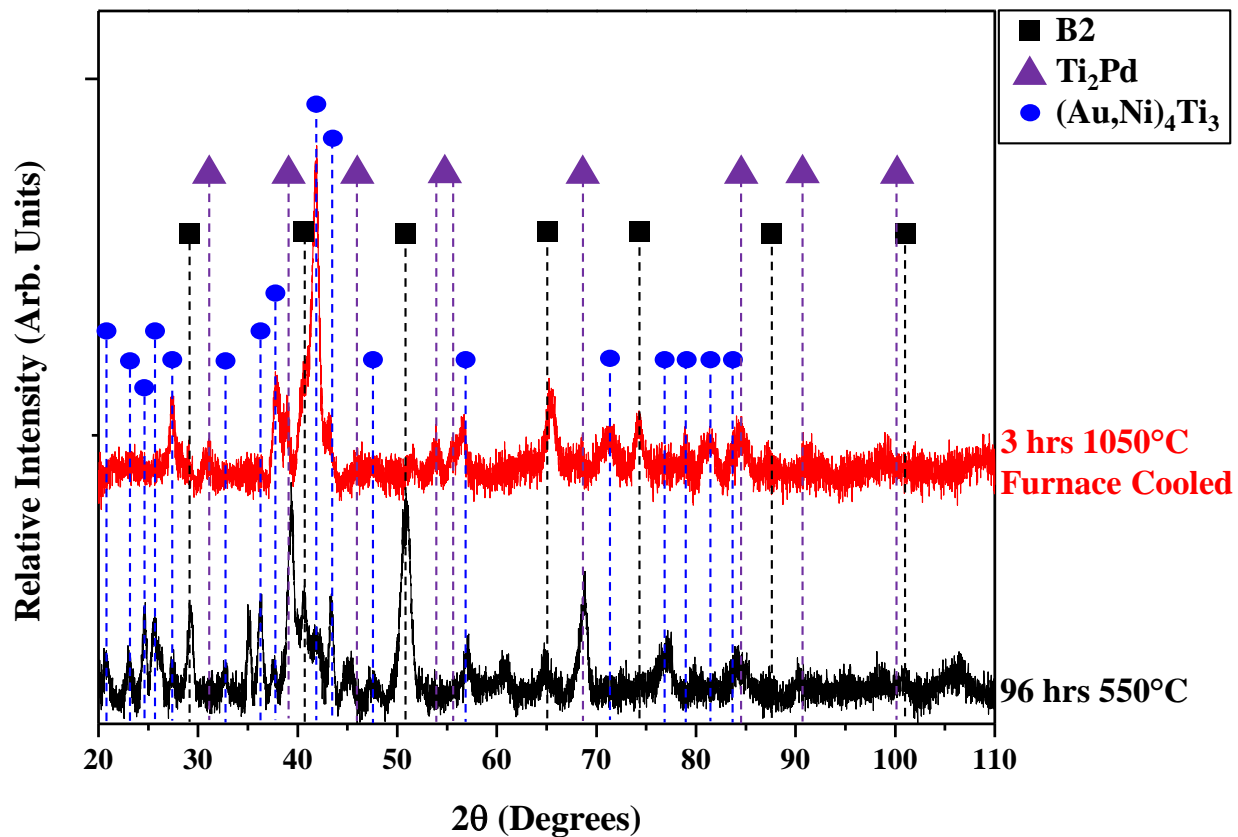


Figure 4-35 XRD spectra of the 1050°C furnace cooled and 550°C/96hrs **Au₂₅** specimens using Cu-K α radiation. Labels are indicative of the B2 matrix phase, the Ti_2Pd phase (analogous to the proposed $Ti_2(Ni,Au)$ type), and peaks thought to be associated with the $(Au,Ni)_4Ti_3$ phase (see discussion section).

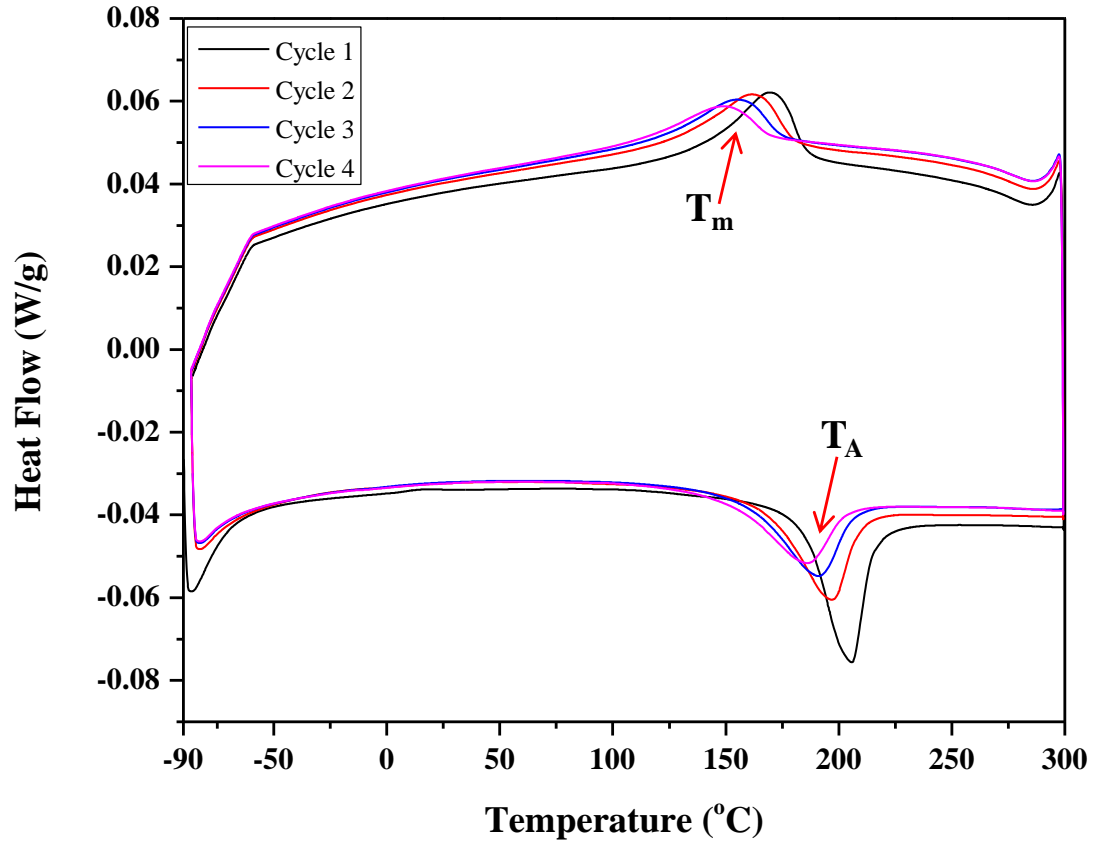


Figure 4-36 Several DSC cycles of **Au25** furnace cooled specimen from -90 to 300 °C. T_m and T_A labels represent martensitic transformation temperature and austenitic transformation temperature, respectively.

CHAPTER 5: CHARACTERIZATION OF TI 2:1 AND AU 4:3 ALLOYS

In an effort to better identify the precipitation behavior in the **Au25** alloy, arc-melted buttons of the two precipitate phases found in the aged specimens were produced.

5.1 Ti 2:1 Alloy

The first precipitate button was based on the results of the 550°C TEM-EDS data from the Ti-rich platelet phase. This alloy was named Ti 2:1. An average composition was computed from all TEM-EDS data scans and a target composition, analogous to the $Ti_2(Ni,Au)$ type stoichiometry, was used. SEM-EDS was utilized to determine the average composition of the as-cast state, as shown in Table 5-1 along with the target composition. The SEM-EDS revealed a slight deviation of chemistry that could have resulted from the arc-melting process. The composition was slightly Au-rich and Ti-lean with respect to the target values.

Table 5-1 Average SEM-EDS and Target Compositions of Ti 2:1 alloy

Average SEM-EDS		Target	
Bulk Composition (at %)		Composition (at %)	
Ti	63.87 ± 0.13	Ti	66.00
Ni	2.76 ± 0.12	Ni	3.50
Au	33.39 ± 0.09	Au	30.50

BSE imaging was also done on the as-cast Ti 2:1 alloy, as shown in Figure 5-1. It is clear from the BSE images of the Ti 2:1 as-cast specimen that there were two main phase regions.

Both regions were inspected via SEM-EDS. The bright region consisted of 55.76 at % Ti – 4.61 at % Ni – 39.63 at % Au, which is expected to correlate with B2 phase. The dark region had an average composition of 69.91 at % Ti – 0.41 at % Ni – 29.69 at % Au, which is thought to be similar to Ti_3Au . It is also interesting to note that there were dark plate-like precipitates found in the bright regions with an average composition of 59.00 at % Ti – 3.29 at % Ni – 37.71 at % Au, as verified with SEM-EDS.

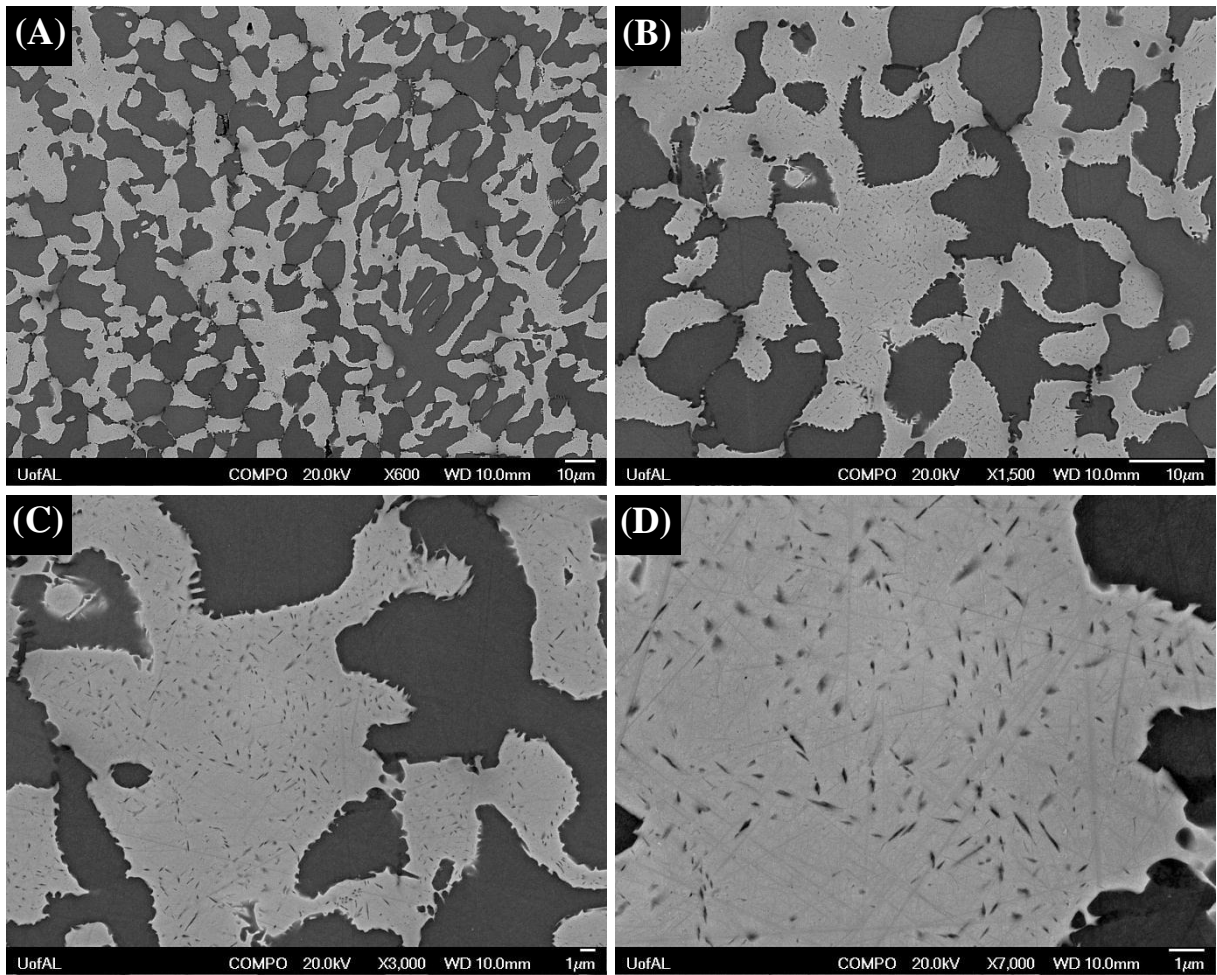


Figure 5-1 BSE images of the **Ti 2:1** as-cast specimen with increasing magnification (A), (B), (C), (D), respectively.

To examine the influence of heat treatment, the Ti 2:1 alloy was subjected to 550°C for 96 hrs, followed by water quenching. This correlates to the peak ageing condition for the 550°C

Au25 specimens. The microstructure consisted of the same two main phases, yet ageing promoted further precipitation in the bright regions, as shown in Figure 5-2. The bright and dark region compositions were examined via SEM-EDS and the results were consistent with the as-cast state. Further EDS compositional analysis was attempted within the bright regions to identify the darker precipitation, but was unsuccessful due to the complex nature of phases present. Some of the precipitation within the bright region also resembled martensite plates, which is plausible if the bright regions are in fact a Ti-Ni-Au B2 phase.

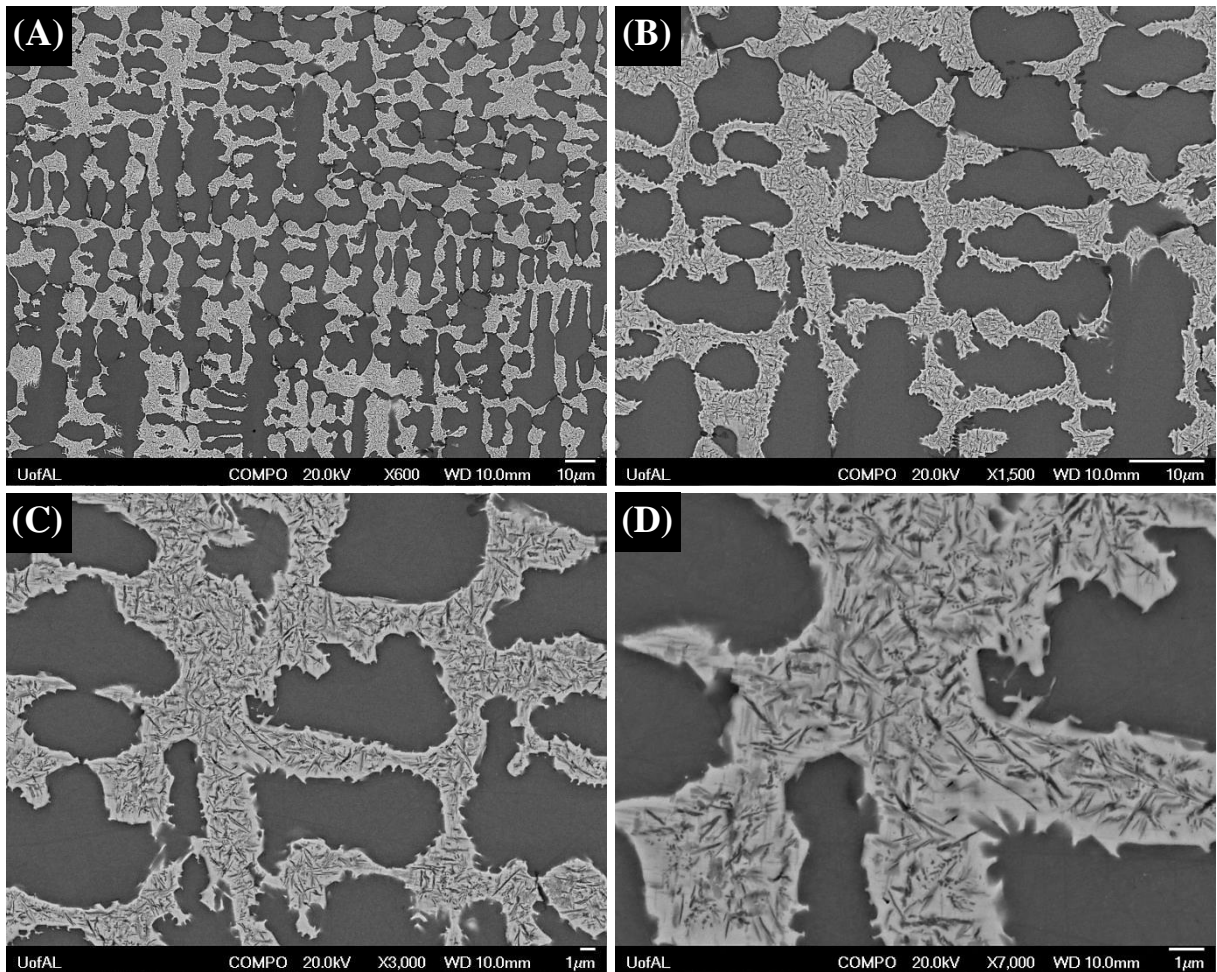


Figure 5-2 BSE images of the **Ti 2:1** 550°C/96hr specimen with increasing magnification (A), (B), (C), (D), respectively.

In order to examine the crystallography of the Ti 2:1 alloy, XRD was done on the as-cast and 96 hr 550°C samples, as shown in Figure 5-3. For a frame of reference, B2 phase peaks, Ti₂Pd peaks, and Ti₃Au peaks were identified. Interestingly, these three phases tended to fit the spectra quite well. However, there was one unidentified peak which occurred at ~ 26°. However, this could be related to the Ti-rich platelets, since Ti₂Pd is only a reference. It is plausible to suggest the presence of these three phase types in the Ti 2:1 microstructure based on the binary Ti-Au phase diagram and SEM-EDS results. All of the B2 peaks overlapped with another phase, which complicates determining its actual presence. The XRD peaks did not seem to change much with ageing. However, there were several Ti₃Au peaks that disappeared with ageing, which may be related to the precipitation mechanism within the alloy. Future transmission electron microscopy is necessary to fully understand the complex microstructure.

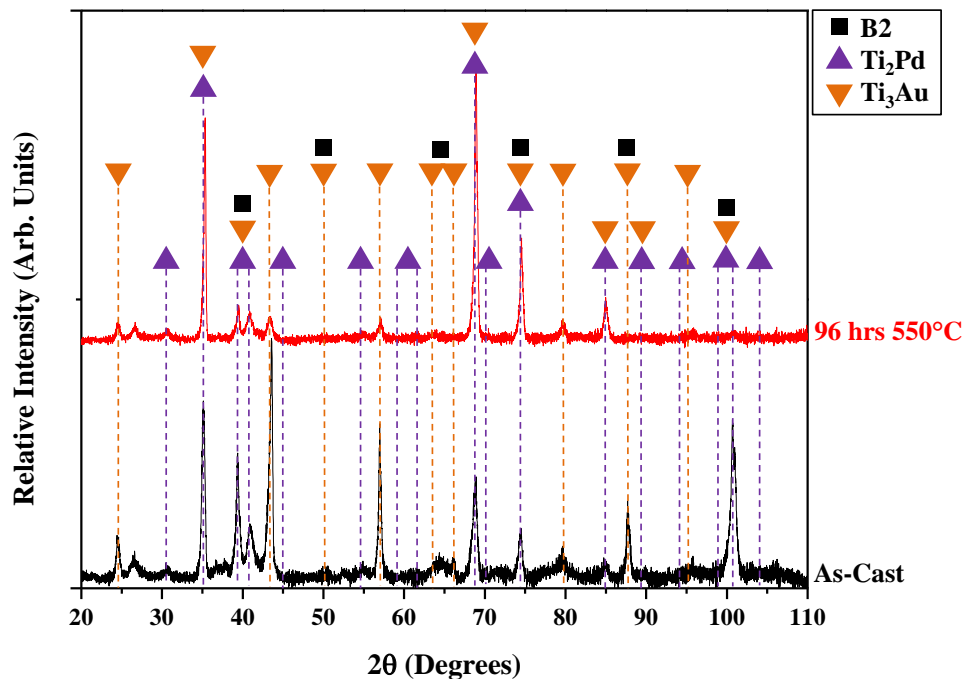


Figure 5-3 XRD spectra of the as-cast and 550°C/96hrs Ti 2:1 specimens using Cu-K α radiation. Labels are indicative of the B2 phase, the Ti₂Pd phase (analogous to proposed Ti₂(Ni,Au) type), and Ti₃Au phase.

5.2 Au 4:3 Alloy

The second precipitate button was based on the results of the 550°C TEM-EDS data and 3DAP identification of the (Au,Ni)₄Ti₃ precipitates. This second precipitate alloy was named Au 4:3. An average composition was computed from all TEM-EDS data scans and a target composition analogous to the (Au,Ni)₄Ti₃ type stoichiometry was used. SEM-EDS was utilized to determine the average composition of the as-cast state, as shown in Table 5-2 along with the target composition. The SEM-EDS results indicated a small deviation from target composition values. However, these discrepancies could have resulted from the arc-melting process. The composition was slightly Ni-rich and Au-lean with respect to the target values.

Table 5-2 Average SEM-EDS and Target Compositions of Au 4:3 alloy

Average SEM-EDS		Target	
Bulk Composition (at %)		Composition (at %)	
Ti	41.68 ± 0.14	Ti	41.70
Ni	25.33 ± 0.11	Ni	27.40
Au	32.79 ± 0.13	Au	30.90

BSE imaging was performed on the as-cast Au 4:3 alloy, as shown in Figure 5-4. Similar to the Ti 2:1 alloy, BSE imaging of the as-cast Au 4:3 specimen revealed two main phases. SEM-EDS was used to examine the chemistry of the two main bright and dark regions. The dark area consisted of 47.05 at % Ti – 25.49 at % Ni – 27.46 at % Au, which may correlate to a Ti-Ni-Au B2 phase. The bright region composition was 32.06 at % Ti – 22.02 at % Ni – 45.92 at % Au, which resembles a (Au,Ni)₂Ti type phase. There were also bright alternating platelets found in the dark regions of the sample. SEM-EDS revealed an average composition of 40.27 at % Ti

– 25.27 at % Ni – 34.57 at % Au. This composition is very similar to that of the $(\text{Au,Ni})_4\text{Ti}_3$ type precipitates found in the aged **Au25** specimens via TEM-EDS. Also, their morphology as depicted in Figure 5-4 (D) is consistent with TEM results of the aged **Au25** specimens.

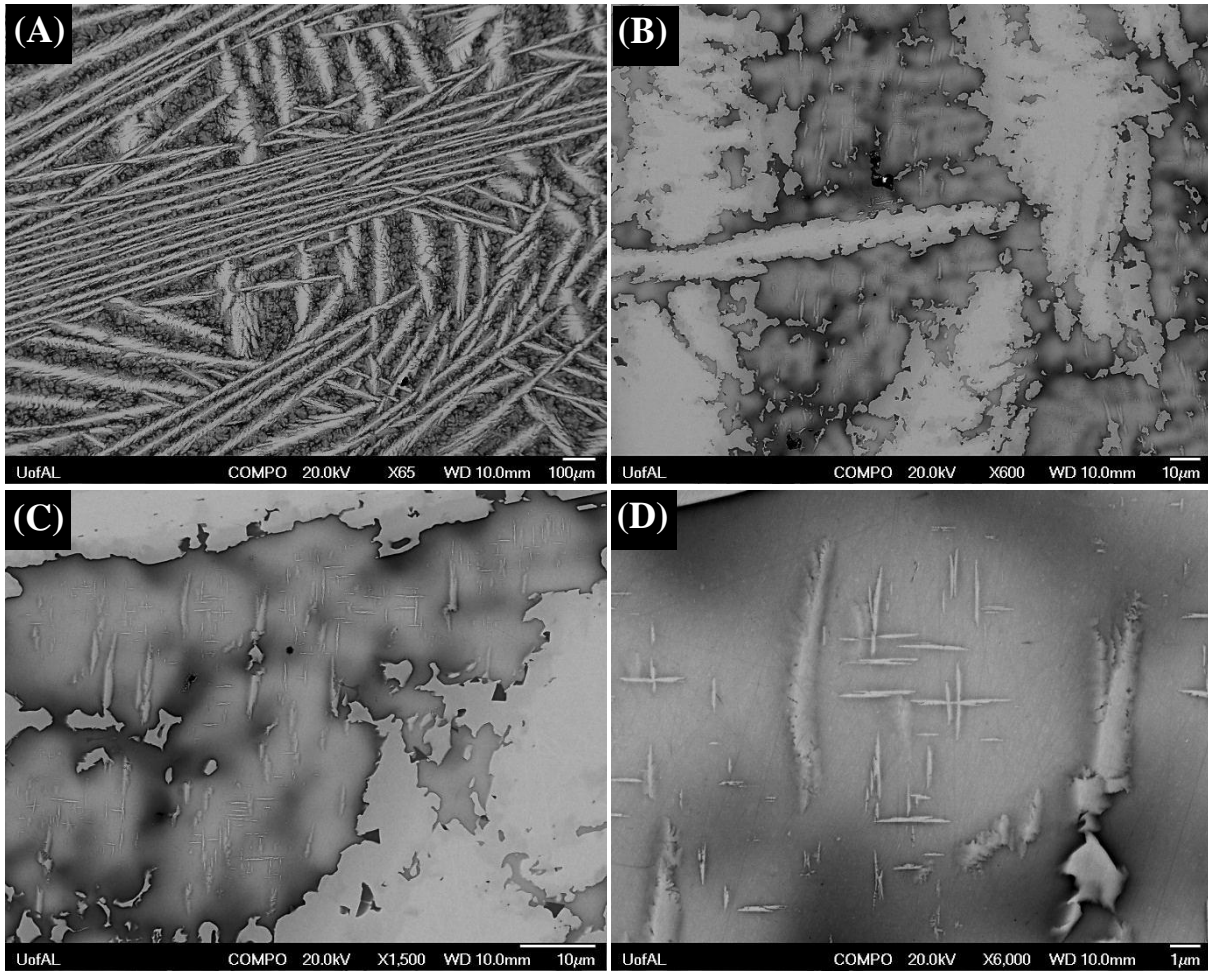


Figure 5-4 BSE images of the **Au 4:3** as-cast specimen with increasing magnification (A), (B), (C), (D), respectively.

In order to examine the influence of ageing on the Au 4:3 as-cast microstructure, samples were aged at 550°C for 96 hrs, followed by water quenching. Again, this ageing condition correlates with the peak-aged condition for the 550°C **Au25** alloy. BSE imaging of the Au 4:3 aged specimen is shown in Figure 5-5. BSE imaging revealed that ageing at 550°C promoted the

growth and further coarsening of the bright platelet phase within the dark regions. The chemical composition of the main bright and dark phases, along with the bright platelets, was verified via SEM-EDS and the results were consistent with the as-cast condition. It is interesting to note that there was also a fine-scale precipitation in the dark regions near interfaces with the main bright regions, Figure 5-5 (D). However, this could also be due to (Au,Ni) depletion resulting from the bright platelet precipitation.

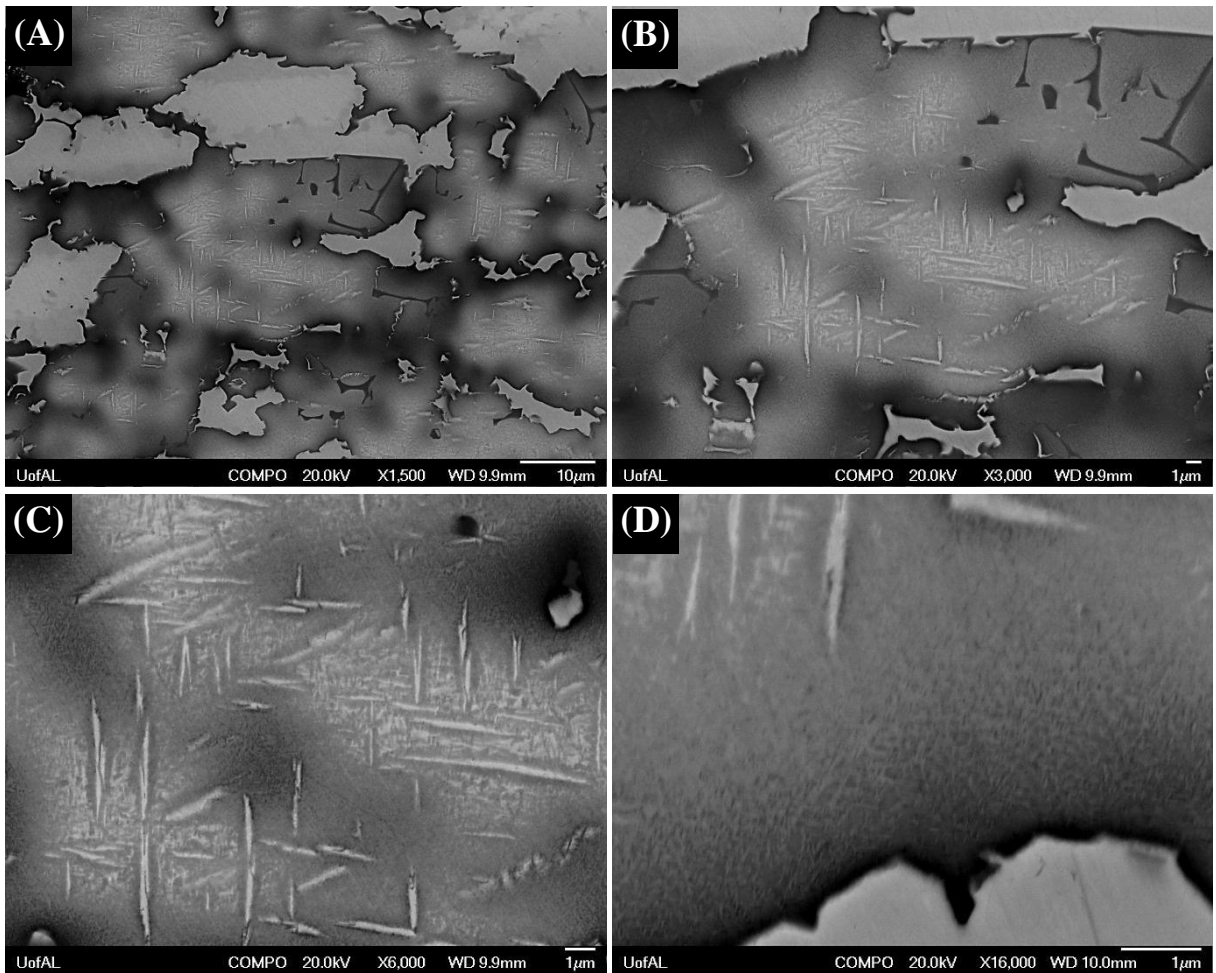


Figure 5-5 BSE images of the **Au 4:3** 550°C 96 hr specimen with increasing magnification (A), (B), (C), (D), respectively.

XRD was done on the as-cast and 550°C aged Au 4:3 alloys in order to examine the crystallography of phases present, as shown in Figure 5-6. XRD spectra of the as-cast and 550°C aged Au 4:3 samples were plotted together for comparison. For a frame of reference, the B2 peaks, Au₂Ti peaks, and reflections thought to be associated with (Au,Ni)₄Ti₃ are identified. The selection of these particular phases was based upon the SEM-EDS results. It is important to note that several peaks, not associated with the three phases, were also present. Specifically, these peaks were approximately 39°, 67°, and 98°. It is hypothesized that these particular peaks could be associated with some other form of nano-scale precipitation not evident in BSE micrographs, or they could be additional peaks associated with some other nano-scale precipitation product not detectable via SEM. However, it is also possible that these reflections correlate to the (Au,Ni)₄Ti₃ phase and were just not visible in other XRD results. The peak locations and crystallography of the (Au,Ni)₄Ti₃ phase will be addressed in great detail in the discussion section.

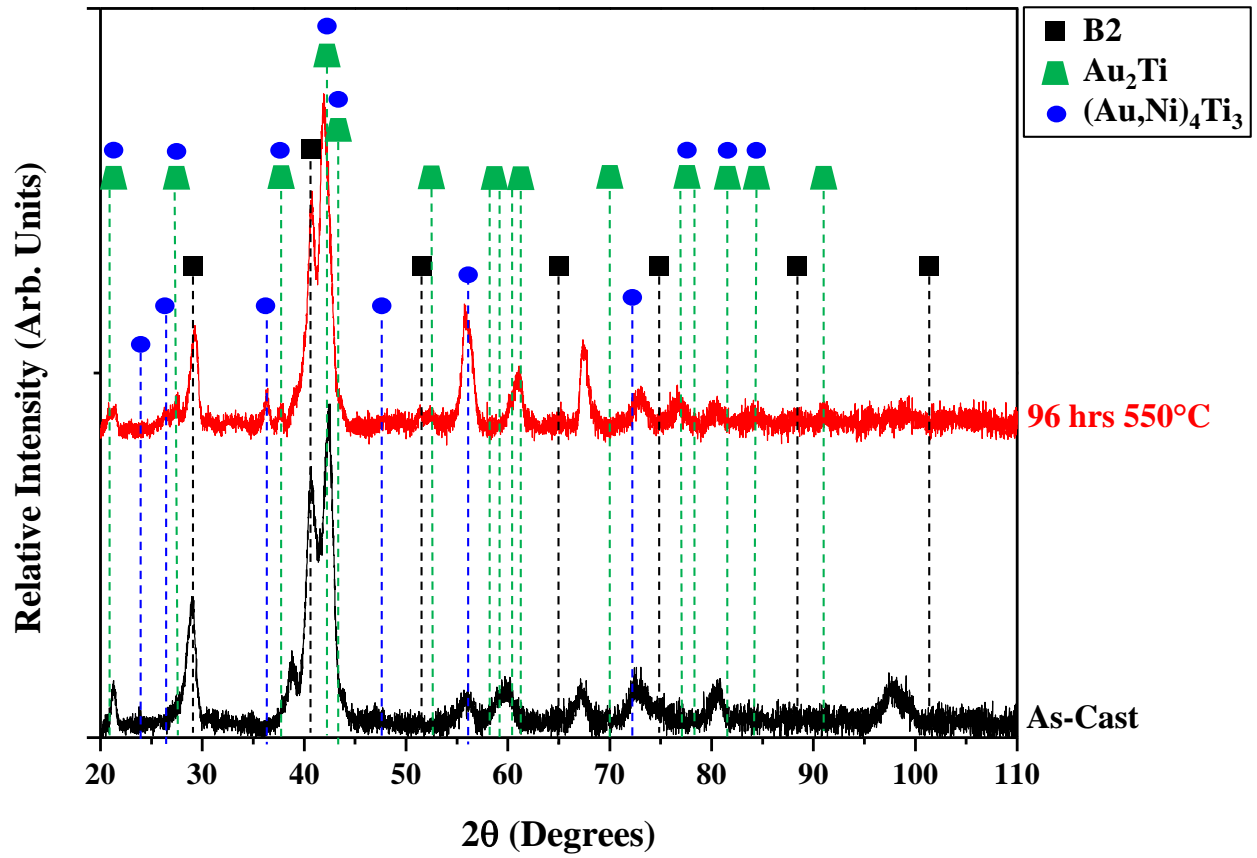


Figure 5-6 XRD spectra of the as-cast and 550°C 96 hr Au 4:3 specimens using Cu-K α radiation. Labels are indicative of the B2 phase, the Au₂Ti phase, and peaks thought to associate with (Au,Ni)₄Ti₃ (see discussion section).

CHAPTER 6: DISCUSSION

6.1 Au25 Alloy

The analysis of the **Au25** alloy indicated the presence of both Ti-rich and (Au,Ni)-rich precipitation in the aged specimens. The proposed phases are $Ti_2(Ni,Au)$ and $(Au,Ni)_4Ti_3$. The crystallography of each phase will be examined and discussed relative to experimental results.

6.1.1 $Ti_2(Ni,Au)$ Phase

Throughout this thesis, the Ti-rich precipitation found in the **Au25** aged specimens was assumed to be $Ti_2(Ni,Au)$, as described with a tetragonal $I4/mmm$ symmetry. This structure is analogous to Ti_2Pd , Ti_2Ag , and Ti_2Cu [37-43,46,47]. A closer literature examination revealed that Ti_2Cu and Ti_2Pd can both form in a B2 matrix [46,48]. The morphology and SADP of Ti_2Pd in a $Ti_{51.2}Pd_{27}Ni_{21.8}$ alloy is shown in Figure 6-1 [48].

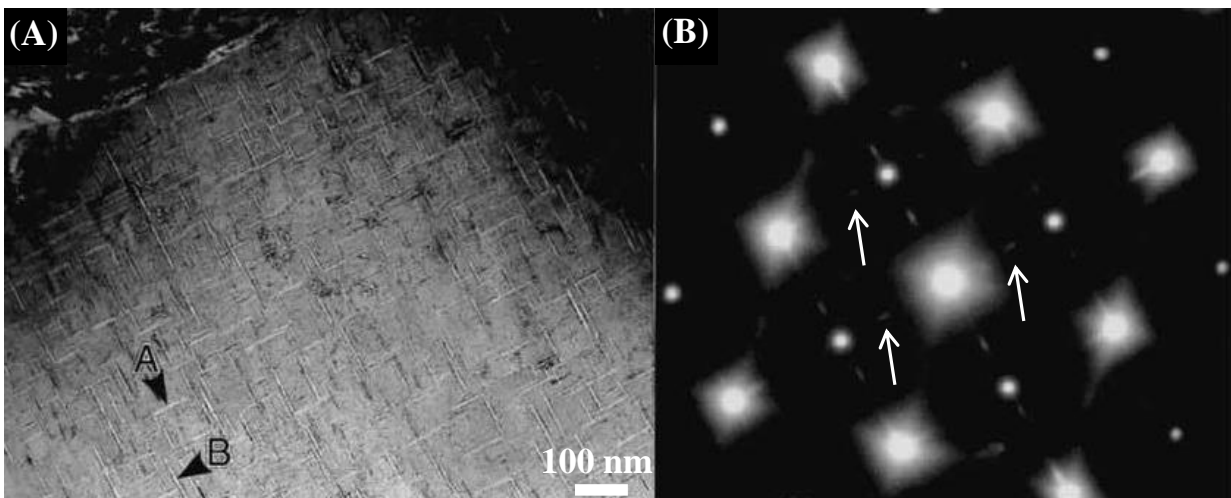


Figure 6-1 TEM bright field of $Ti_{51.2}Pd_{27}Ni_{21.8}$ heat treated for 1 hr at 773 K (A) and SADP down the $[100]_{B2}$ direction showing additional Ti_2Pd streaking (B). Labels “A” and “B” show two platelet variants. Adapted from reference [48].

The morphology and size of the Ti₂Pd platelets is consistent with the Ti₂(Ni,Au) type found in the aged **Au25** specimens, Figure 6-1 (A) and Figure 4-11 (A), respectively. It is also interesting to note that both systems contain two orthogonal platelet variants with their habit plane parallel to the <100>_{B2} direction. It is also clear from the SADP, Figure 6-1 (B), that the Ti₂Pd platelets create additional streaking between superlattice and main reflections, which is consistent with the additional streaks in the **Au25** aged alloy, Figure 4-11 (B). The proposed orientation relationship in the Ni-Ti-Pd system was the following [48]:

$$[001]_{B2} \parallel [001]_{Ti2Pd}$$

$$(001)_{B2} \parallel (002)_{Ti2Pd}$$

$$(010)_{B2} \parallel (002)_{Ti2Pd}$$

Single Crystal TM was used to simulate these orientation relationships [30]. First, the Ti₂Pd unit cell was created in Crystal Maker TM using lattice parameters a = 3.09 Å, c = 10.04 Å, and I4/mmm symmetry [29,43]. The constructed cell was then placed in Single Crystal TM and both orientations of the platelets were simulated, as shown in Figure 6-2. Using the orientation relationship above, [100] and [010] Ti₂Pd SADPs were simulated, Figure 6-2 (A) and (B), respectively. Weighted reciprocal lattices were used for all simulations in order to better compare with experimental results. The two Ti₂Pd platelet variants were then stacked on top of each other and superimposed onto a [100] oriented B2 matrix, Figure 6-2 (C). This simulation matched the literature and experimental results of the **Au25** 400°C/168hrs specimen quite well. Streak locations were in between superlattice and primary B2 reflections, which is consistent with the simulations, as shown in Figure 6-2 (D). Thus, it is plausible that the Ti-rich platelets in the aged **Au25** samples exhibit a tetragonal I4/mmm symmetry as well. Simulations also matched other systems found in literature dealing with Ti₂Cu in a B2 matrix [46].

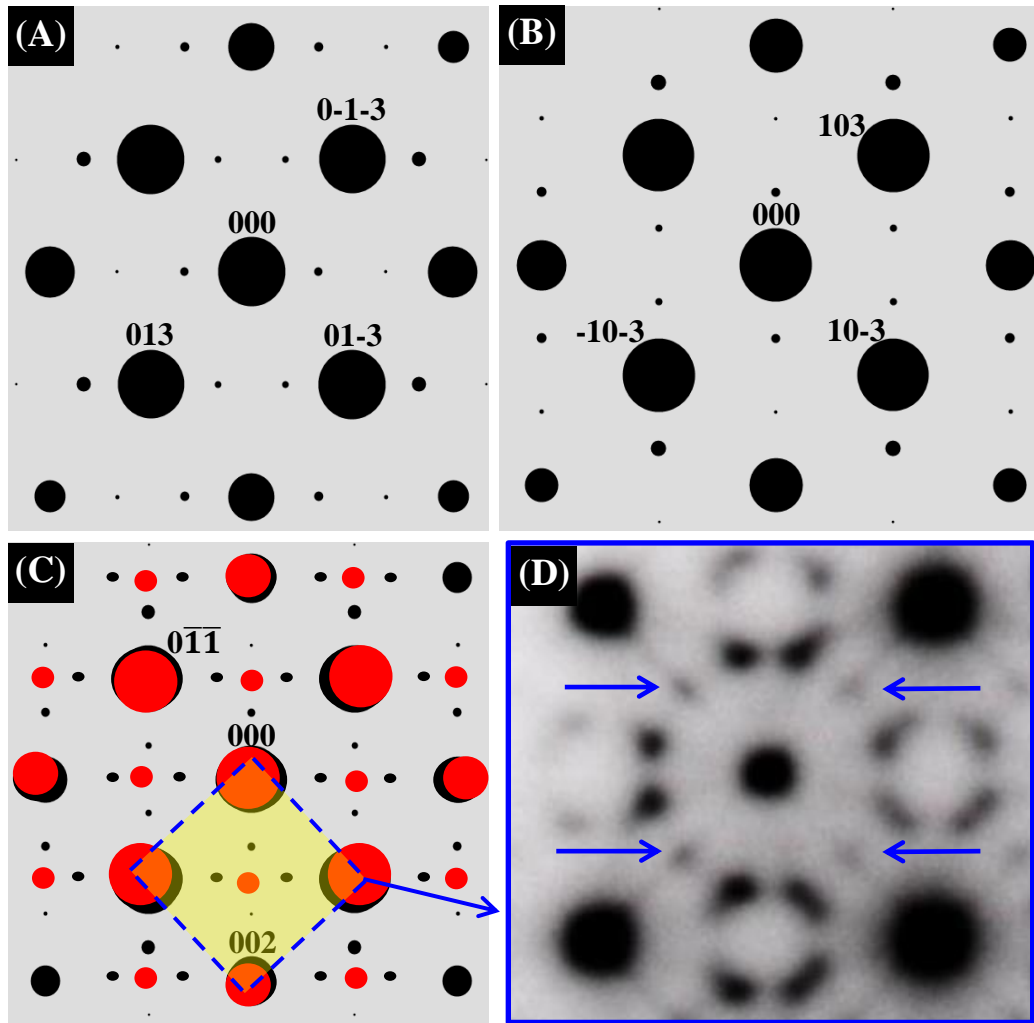


Figure 6-2 Simulated SADPs with weighted reciprocal lattice for the two Ti_2Pd variants $[100]_{\text{Ti}_2\text{Pd}}$ (A) and $[010]_{\text{Ti}_2\text{Pd}}$ (B). The indices in (A) and (B) correlate to Ti_2Pd . (C) depicts the two variants stacked atop of a $[100]$ oriented B2 phase, as shown with red spots and weighted reciprocal lattice. The labels in (C) denote cubic B2 indices. Lastly, (D) shows a SADP section from the **Au25** $400^\circ\text{C}/168\text{hrs}$ sample down the $\langle 100 \rangle_{\text{B}_2}$ direction. Arrows in (D) point out streaks between superlattice and main reflections.

The $I4/mmm$ structure designation for the Ti-rich platelets is also consistent with XRD results since Ti_2Pd was referenced and fit all XRD spectra containing the Ti-rich platelet phase. However, actual peak locations could vary slightly since the c/a ratio and lattice ordering may be

different. Further clarification of the proposed crystallography was made in the 550°C **Au25** aged specimens. TEM-EDS revealed a composition near Ti_2Au , with a small amount of dissolved Ni, which is consistent with the stoichiometry of the Ti_2Pd phase. Also, two zone axes were found on a $Ti_2(Ni,Au)$ platelet that correlated to simulated Ti_2Ag SADPs, Figure 4-17. The difference between the experimental angle and theoretical angle of the two zones was less than a degree.

In terms of compositional chemistry, there appeared to be inconsistencies with the 3DAP results of the 400°C **Au25** aged specimens and the TEM-EDS of the 550°C specimens. This may suggest a multi-stage precipitate transformation mechanism. It is quite possible that the metastable Ti-rich platelet phase may complete a series of compositional changes with ageing, as does the Ni_4Ti_3 phase in the binary Ni-Ti system [4]. This would explain the variation in platelet composition found in the 400°C 3DAP results, but not found in the TEM-EDS 550°C results. This may also correlate to the difference in hardening behavior at both temperatures, Figure 4-5. Since both microstructures were considered to be the same, it was not expected that the 550°C would take longer to age-harden. However, if there are compositional changes during ageing at higher temperatures, than that could explain such behavior. Future atom probe tomography of the 550°C **Au25** aged specimens is underway to exploit this discrepancy.

6.1.2 (Au,Ni)₄Ti₃ Phase

It was found that ageing the **Au25** alloy at both 400°C and 550°C promoted the growth of a finely dispersed, nano-scale $(Au,Ni)_4Ti_3$ phase. This phase is similar to the Ni_4Ti_3 precipitation found in Ni-rich Ti-Ni alloys [3,4,9,33]. It is hypothesized that its existence stems from insufficient cooling during quenching, which leaves a small amount of $(Au,Ni)_4Ti_3$ in the matrix. This is consistent with SADPs from the 1050°C/3hr solution treated specimen, Figure 4-4, which

revealed additional precipitation in the matrix. Further ageing at 400°C and 550°C promoted the growth and coarsening of this phase, as depicted in SADPs, Figures 4-10, 4-11, 4-12, and 4-13. The composition was also verified via TEM-EDS and 3DAP iso-surface analysis, Tables 4-2, 4-4, and 4-7. However, the crystallography of the phase was never addressed. SADPs from the (1050°C/3hrs + 400°C/168hrs) **Au25** alloy were compared to those found in literature. Interestingly, two FCC systems, Au - (1-3 at %) Ti and Cu - (1-6 at %) Ti, were found to have very similar precipitation signatures within SADPs, as shown in Figure 6-3 [49,50].

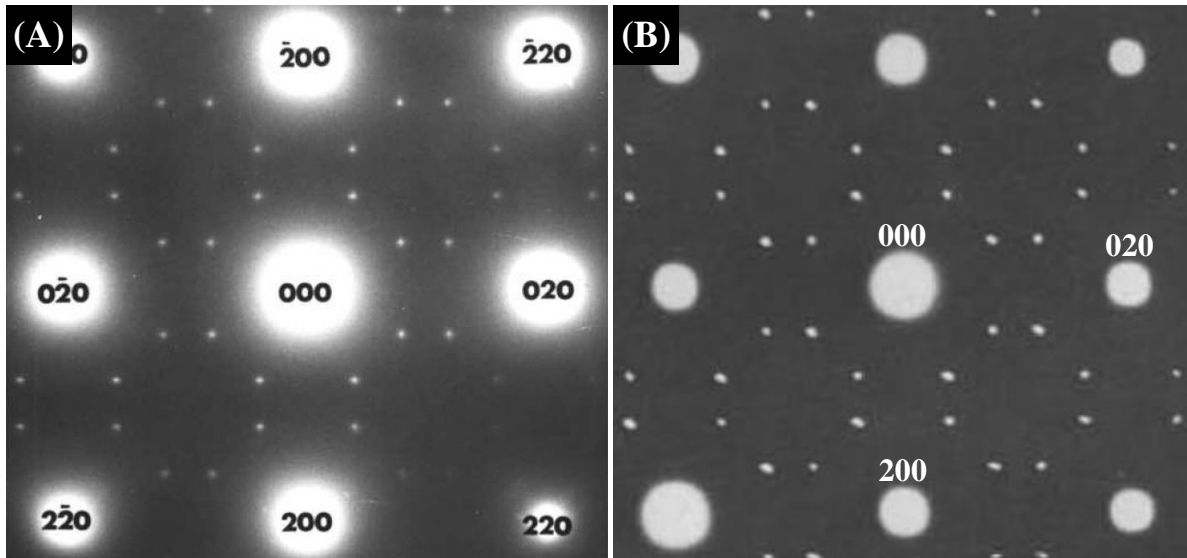


Figure 6-3 SADP in Cu-Ti alloy showing two variants of $D1_a$ structure down $[001]_{\text{FCC}}$ with FCC indices (A) and SADP in Au-Ti alloy depicting same two variants of $D1_a$ structure down $[001]_{\text{FCC}}$ with FCC indices (B). Adapted from references [49,50].

It is interesting to note that in both of these FCC systems, two variants of a tetragonal $D1_a$ structure were found, with the following orientation relationship [49,50]:

$$[001]_{\alpha\text{-FCC}} \parallel [001]_{D1a}$$

$$(120)_{\alpha\text{-FCC}} \parallel (110)_{D1a}$$

The additional precipitate spots in these electron diffraction patterns were quite similar to those found in one **Au₂₅** specimen that was aged at 650°C for 48hrs, Figure 6-4. This was the only specimen aged at 650°C and it was done to try and coarsen the precipitates.

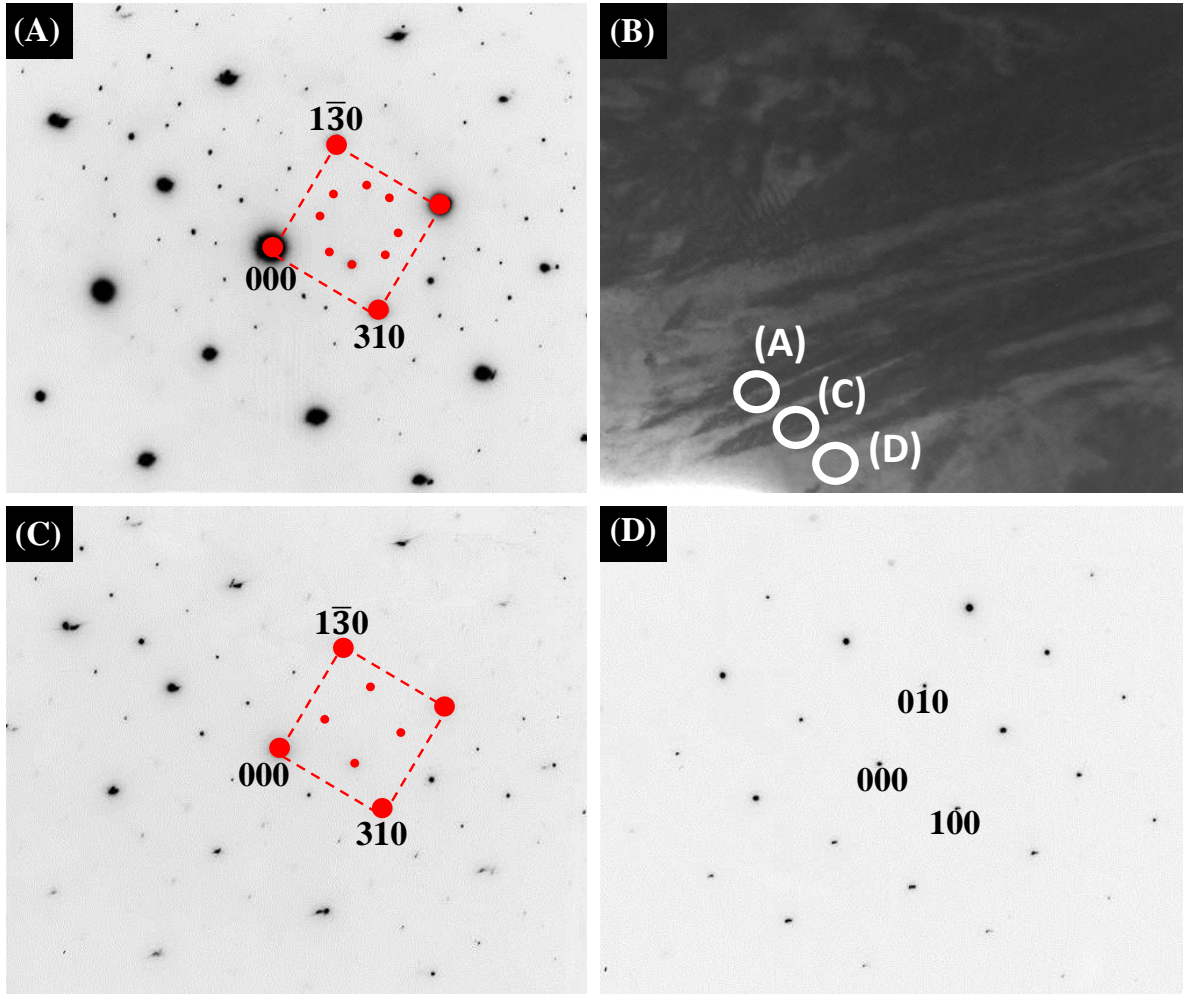


Figure 6-4 TEM-BF image of **Au₂₅** aged 650°C/48hrs oriented down the $[100]_{B2}$ (B) with corresponding SADPs from regions (A), (C), and (D). Indices in (D) represent cubic B2. Indices in (A) and (C) correspond to $[001]$ oriented D1a type structure. (C) depicts in red one D1a variant oriented $[001]_{D1a}$. (A) depicts two stacked D1a variants.

Interestingly, as was shown in Figure 6-3, the **Au₂₅** 650°C/48hr specimen contained precipitates that appeared to have tetragonal D1a symmetry, Figure 6-4 (A) and (C). Three

different regions were selected for SADPs, as shown in Figure 6-4 (B), and each was oriented $[100]_{B2}$. A B2 matrix was captured in Figure 6-4 (D). Moving slightly up, as shown in Figure 6-4 (B), a SADP was captured that indexed as one variant of the D1a structure type described previously, shown in Figure 6-4 (C). Moving further up the specimen, another SADP was taken consisting of two different D1a variants stacked atop of each other, Figure 6-4 (A). Both variants appear to be aligned with $[001]_{D1a} // [100]_{B2}$ and $[00\bar{1}] // [100]_{B2}$. The lattice parameters $a = b = 9.71 \text{ \AA}$ were calculated for this D1a type structure from the SADP in Figure 6-4 (C). These refined parameters were used in further simulations of the D1a, Au_4Ti prototype.

In conjunction with the **Au25** 400°C SAPDs, Au_4Ti ($D1_a$) with refined lattice parameters $a = b = 9.71 \text{ \AA}$ and $c = 4.00 \text{ \AA}$ was modeled in Crystal MakerTM and SADPs of interest were simulated using Single CrystalTM. Au_4Ti was used since it exhibits the $I4/m$, $D1_a$ type structure that was found in the literature and matched well with the experimental SADPs, Figure 6-3 (B) [49]. Two $D1_a$ variants were simulated and rotated about the c-axis to fit the $[100]_{B2}$ direction, as shown in Figure 6-5.

The simulated diffraction patterns were oriented in the following manner:

$$[001]_{D1a} // [100]_{B2} \text{ and } (310)_{D1a} // (011)_{B2}$$

$$[00\bar{1}]_{D1a} // [100]_{B2} \text{ and } (310)_{D1a} // (011)_{B2}.$$

The second $D1_a$ variant was obtained by taking a mirror reflection of the first variant. It is important to note that a slightly different orientation relationship was obtained, but this could be due to the difference in the matrix structure. Within the **Au25** alloy, a B2 matrix is assumed, which could cause the planar relationship to differ in comparison to an FCC matrix. However, the simulated patterns fit the experimental results quite well. Both the Ti-rich and Au-rich precipitate simulations were then combined and stacked atop of a simulated B2 matrix, as shown

in Figure 6-6. The simulated results appeared consistent with the experimental SADPs. This suggests that the $(\text{Au,Ni})_4\text{Ti}_3$ phase exhibits symmetry similar to a $D1_a$ type symmetry.

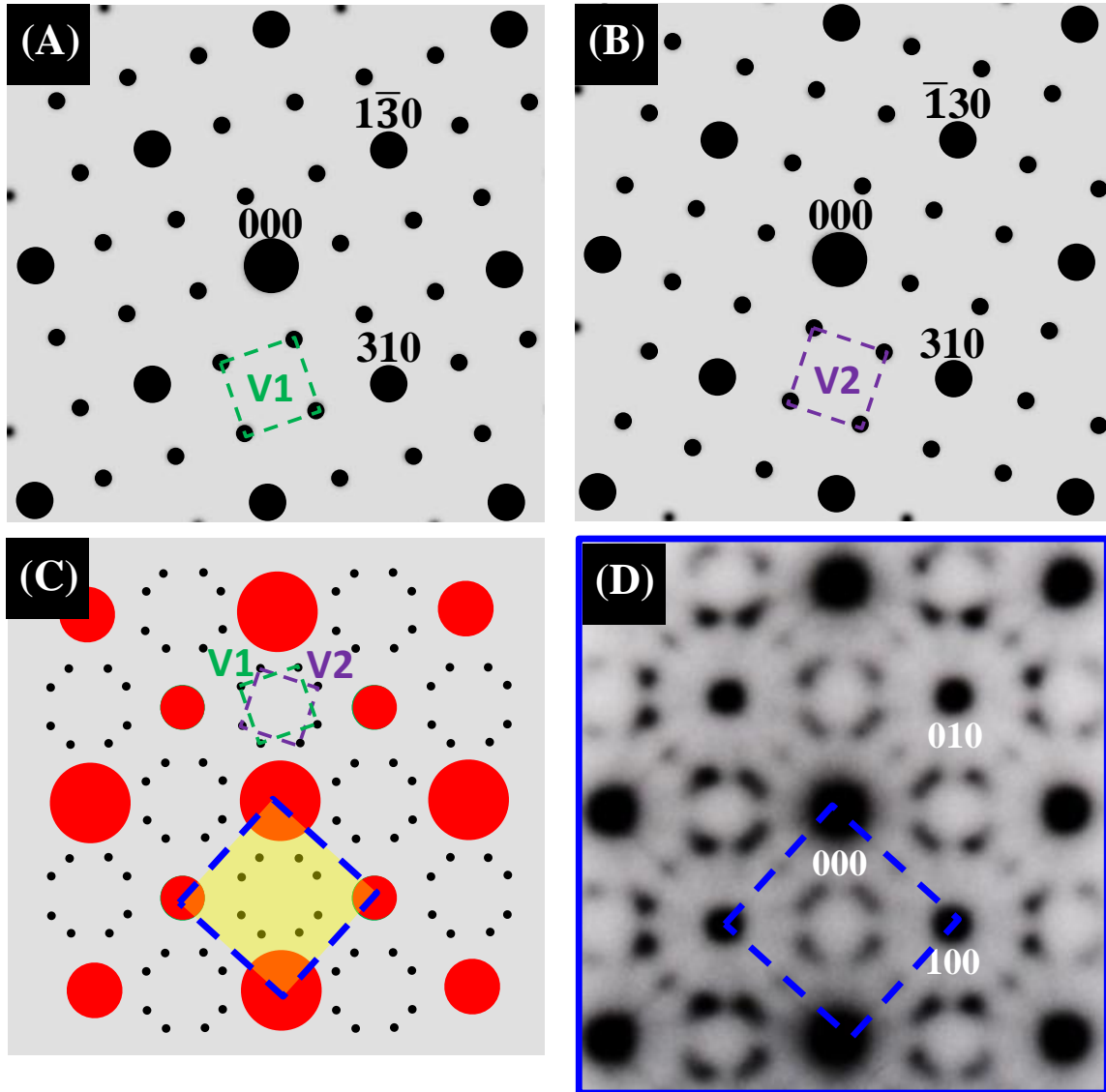


Figure 6- 5 Simulated SADPs with weighted reciprocal lattice for two $D1_a$ variants (A) and (B), respectively, with $[001]_{D1a} \parallel [100]_{B2}$. The indices in (A) and (B) correlate to $D1_a$ structure. (C) depicts the two variants stacked atop of a $[100]$ oriented B2 matrix, as shown with red spots. In (C) both $D1_a$ variants are labeled. Lastly, (D) shows a SADP from the **Au25** $400^\circ\text{C}/168\text{hr}$ sample down the $[100]_{B2}$ direction.

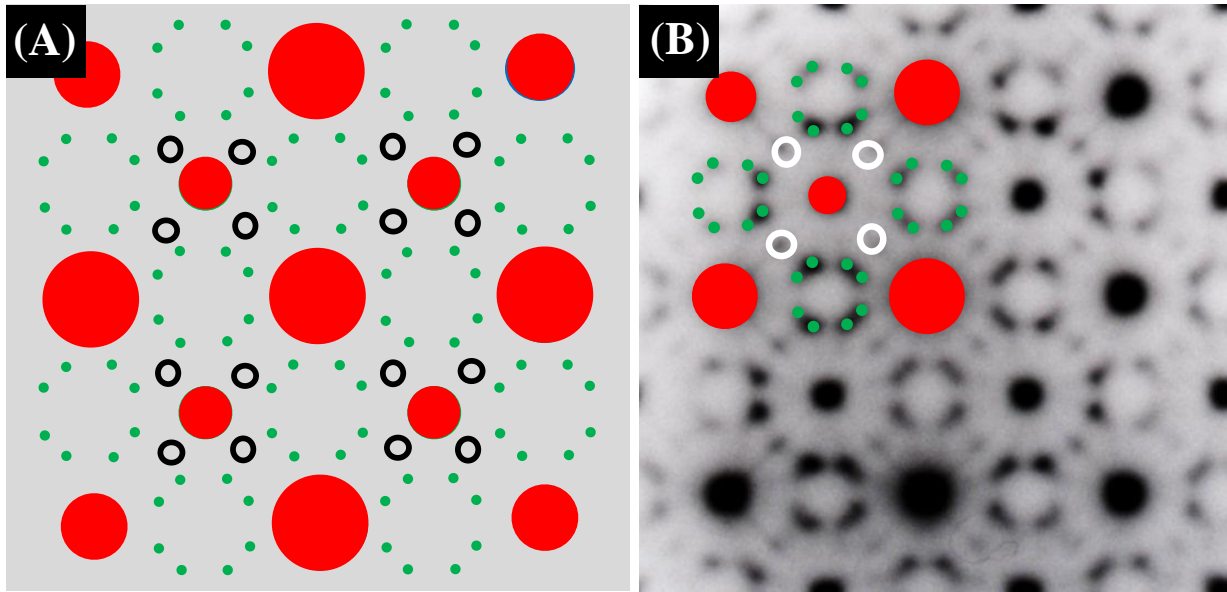


Figure 6-6 Simulated SADPs with weighted reciprocal lattice for two D1a variants (Green), two tetragonal I4/mmm variants (open circles), and B2 matrix (Red) (A). The same phases are then stacked on a $\langle 100 \rangle_{B2}$ SADP from the **Au25** 400°C 168hr specimen.

Using the established orientation relationship for each precipitate and its variants, SADPs were simulated for the $[110]_{B2}$ and $[111]_{B2}$ directions. The results are depicted in Figures 6-7 and 6-8, respectively. As circled in Figure 6-7, there are key areas of comparison that show good matching for the $[110]_{B2}$ direction. For the $[111]_{B2}$ direction, the simulation does not contain all of the extra spots in the experimental SADP, as shown in Figure 6-8. However, the apparent asymmetry of the pairs of spots surrounding the matrix spots does correlate well to the asymmetric angular values measured in the experimental SADP. The extra spots may represent additional precipitate variants within the matrix. However, it is also plausible to suggest that the $(Au,Ni)_4Ti_3$ may exhibit symmetry similar to the D1a type, but may occupy the unit cell in a slightly different way. This could create additional spots in certain directions. Further electron microscopy is needed to justify this claim.

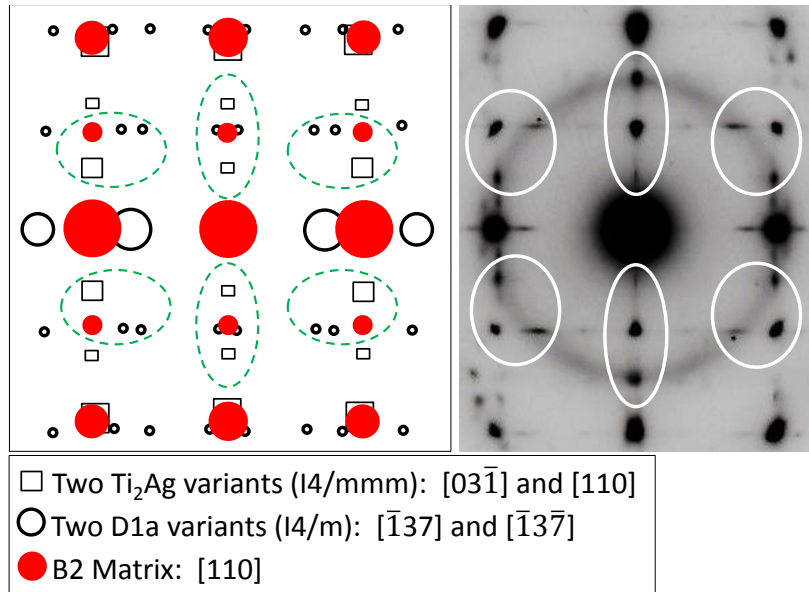


Figure 6-7 Simulated SADPs with weighted reciprocal lattice for two D1a variants, two tetragonal $I4/mmm$ variants, and $[110]$ oriented B2 matrix. The simulations are then compared to a $[110]_{\text{B2}}$ SADP from the **Au25** 400°C 168hr specimen. Specific areas of comparison are circled in the simulation and corresponding locations in the experimental SADP.

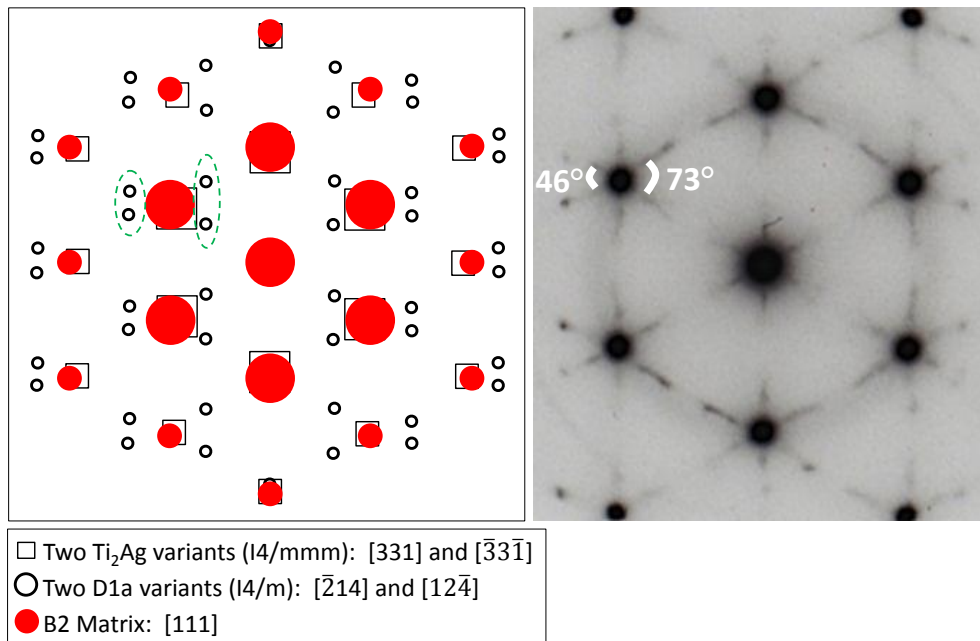


Figure 6-8 Simulated SADPs with weighted reciprocal lattice for two D1a variants, two tetragonal $I4/mmm$ variants, and $[111]$ oriented B2 matrix. The simulations are then compared to a $[111]_{\text{B2}}$ SADP from the **Au25** 400°C 168hr specimen. Interestingly, the asymmetry of the two circled pairs of dots is also viewed in the experimental SADP showing asymmetric angular measurements.

These proposed structures were then compared to the XRD spectra of the 400°C/168hrs and 550°C/168hrs samples. As shown in Figure 6-9, the two spectra are shown with reference peaks from a B2 phase, a Ti₂Pd (I4/mmm) phase, a Au₄Ti (D1_a) phase, and all unidentified peaks thought to associate with the (Au,Ni)₄Ti₃ precipitates. It is interesting to note that many of the Au₄Ti peaks are in similar positions as the (Au,Ni)₄Ti₃ proposed peaks. This correlates with the symmetry near the D1_a structure. However, their mismatch could be due to the c/a ratio difference, which can cause systematic peak shifts and different atom placements in the unit cell. It is also important to observe that many of the Au₄Ti peaks overlap with B2 and Ti₂Pd peaks. This could suggest that there exists (Au,Ni)₄Ti₃ peaks that overlap as well. Further TEM work is necessary to further evaluate the precipitate structures.

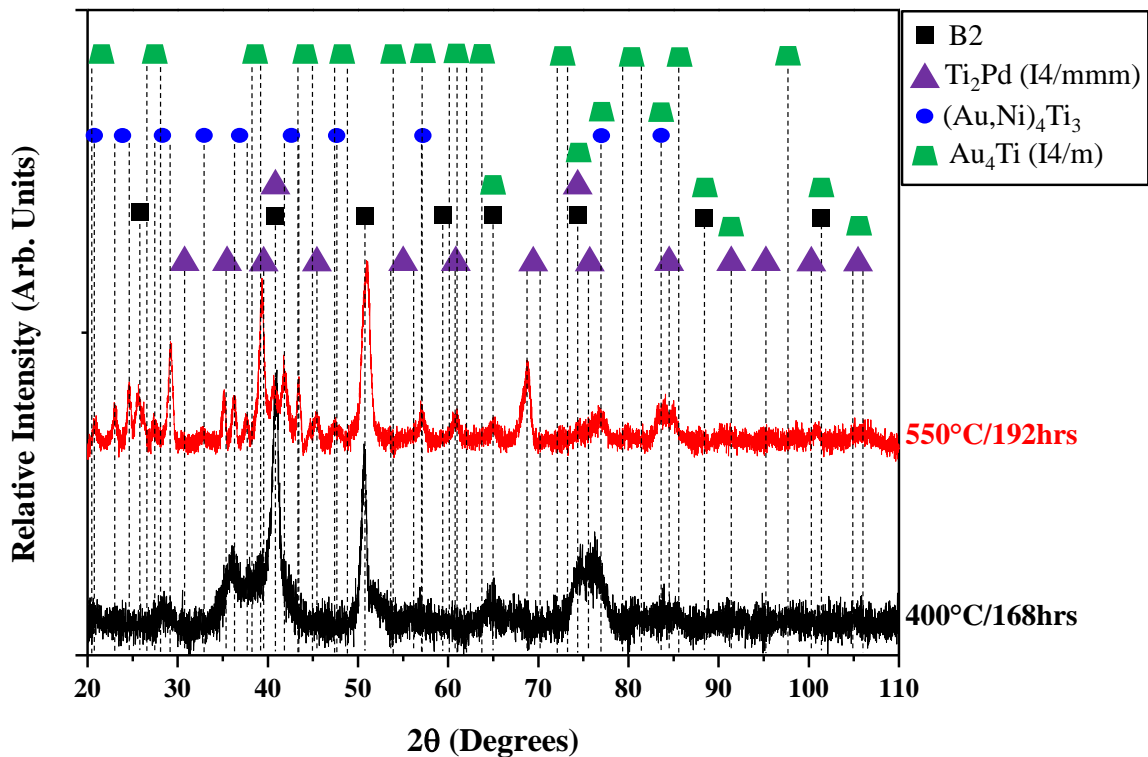


Figure 6-9 XRD spectra of the 400°C/168hrs and 550°C/96hrs **Au25** specimens using Cu-K α radiation. Labels are indicative of a B2 phase, a Ti₂Pd (I4/mmm) phase, a Au₄Ti (D1_a) phase, and peaks previously thought to associate with (Au,Ni)₄Ti₃.

6.1.3 Proposed Precipitation Mechanism

In the Ni-rich **Au25** alloy, (Au,Ni) rich precipitation was expected. This is consistent with similar shape memory alloy systems [3,4,6,7,18]. The onset of Ti-rich precipitation was not an anticipated result. However, it is proposed that the $(\text{Au,Ni})_4\text{Ti}_3$ precipitation could create Ti-rich regions locally, since they pull excess Au and Ni from the matrix. It is hypothesized that these (Au,Ni) depleted regions create a driving force for further Ti-rich precipitation with ageing. This type of precipitation mechanism is similar one found in literature [51]. This type of methodology is shown in Figure 6-10. Initially, a distribution of $(\text{Au,Ni})_4\text{Ti}_3$ populates the matrix, Figure 6-6 (A). This is consistent with the as-cast **Au25** SEM results. Again, it is hypothesized that a small fraction of the 4:3 phase remains after solution annealing due to insufficiencies in watering quenching time [5]. In terms of local composition, it is proposed that this (Au,Ni) rich phase creates a Ti-rich region surrounding each precipitate. Further ageing at 400°C and 550°C is thought to coarsen existing 4:3 precipitates and also nucleate more. This then creates a homogeneous distribution of Ti-rich regions throughout the matrix. However, it is proposed that the Ti-rich concentration within these regions reaches a point of maximum solubility, where a driving force for Ti-rich precipitation then becomes active. Therefore, prolonged ageing promotes the growth and further coarsening of the Ti-rich phase.

6.1.4 Transformation Behavior and Hardness

DSC results of the **Au25** alloy indicated evident martensitic transformation in the as-cast and 1050°C furnace cooled conditions, Figures 4-30 and 4-35, respectively. It is also interesting to note that the transformation temperature increased with furnace cooling. However, for all 400°C and 550°C aged specimens tested, no phase transformations were present, Figures 4-31 and 4-32, respectively.

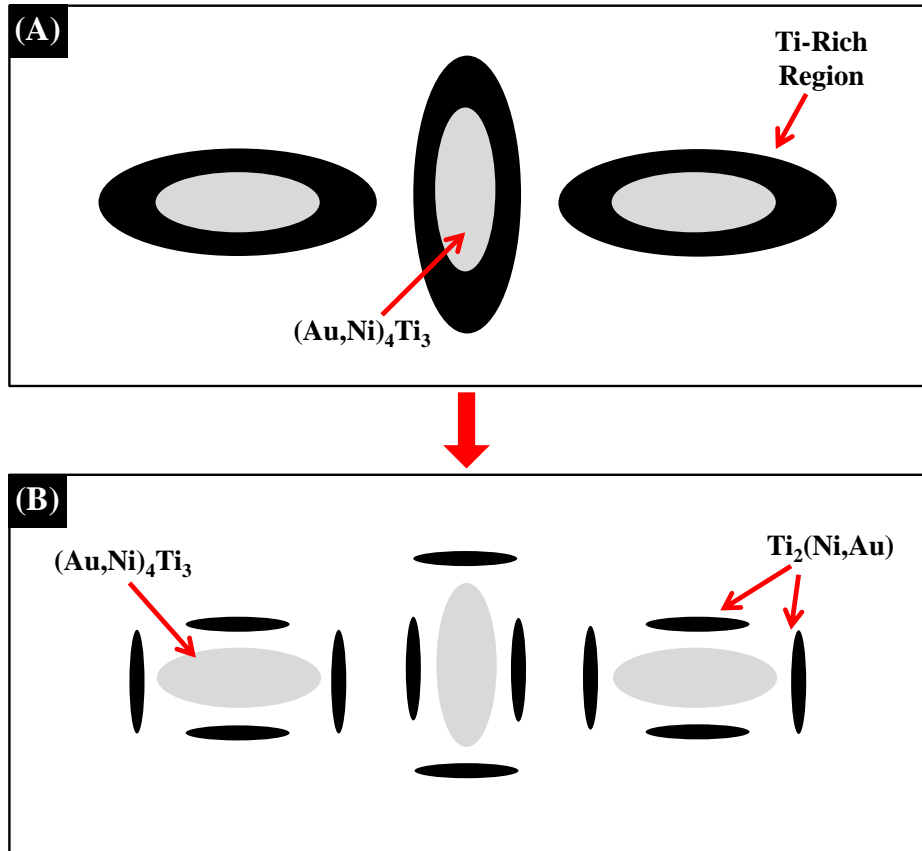


Figure 6-10 Proposed precipitation mechanism of $(\text{Au,Ni})_4\text{Ti}_3$ and $\text{Ti}_2(\text{Ni,Au})$ in the **Au25** alloy from the initial as-cast state (A) to further aged state (B). Adapted from reference [51].

It is proposed that the onset of Ti-rich precipitation in the aged specimens may act to suppress martensite from forming upon cooling. Although there is no TEM data for the as-cast and furnace cooled **Au25** samples, SEM suggests a matrix dominated by bright platelets in both cases, Figures 4-1 (B) and 4-33, respectively. These platelets are hypothesized to correlate to the $(\text{Au,Ni})_4\text{Ti}_3$ plates found in all of the aged specimens. The increase in transformation temperature with furnace cooling corresponds to the coarsening of the $(\text{Au,Ni})_4\text{Ti}_3$ phase. This creates a Ti-rich matrix, which is known to increase martensitic transformation temperatures in Ti-Ni-based shape memory alloys [3,4,6,7,12,18,52].

In the as-cast and furnace cooled states, it is proposed that the Ti-rich precipitation does not readily occur due to non-optimal kinetics. For one, the as-cast state was allowed to cool in arc melter, which does not allow much time for the proposed Ti-rich precipitation mechanism to occur. Secondly, the furnace cooled specimen was cooled slower, but only over the course of several hours / temperature steps, which is thought to only coarsen the $(\text{Au,Ni})_4\text{Ti}_3$ phase. It is hypothesized that these two stages lock in a super saturated Ti-rich matrix. It is also hypothesized that the additional presence of Au increases the solubility of Ti in the B2 phase based on the binary Ti-Au phase diagram. This would explain the presence of martensitic transformation in the as-cast specimen and the increase in transformation temperature in the furnace cooled sample.

In terms of the aged specimens, there was much more time and possibly a higher driving force for the nucleation and growth of a Ti-rich phase. Thus, specimens at 400°C and 550°C contained a distribution of Ti-rich platelets. It is proposed that the nucleation and growth of the Ti-rich precipitation tends to lean the matrix of Ti to near equiatomic or slightly Ni-rich chemistries. Interestingly, it is known that decreased Ti concentrations within the matrix of Ti-Ni-based SMAs tends to decrease the martensitic transformation temperature [3,4,6,7,9,53]. Thus, it is plausible to suggest that the Ti-rich precipitation in the **Au25** aged samples suppresses the martensite by increasing the Ni content in the matrix, which ultimately stabilizes the high temperature austenite phase. The precipitate volume fraction and spacing within the matrix may also act to pin the martensite from forming. However, DSC scans of the 1000 hr 400°C aged specimen did not reveal any martensitic transformation. Further 3DAP studies on severely aged-specimens, accompanied by DSC data, is needed to justify this claim.

Even though martensitic transformation was not detected via DSC in the aged specimens, it is interesting to note the high hardness that **Au25** alloy exhibits, Figure 4-5. This suggests that the precipitation has a beneficial impact on the structural behavior. It would be interesting to try further mechanical tests to examine how the alloy accommodates various states of stress.

6.2 Ti 2:1 Alloy

In order to examine the crystallography of the proposed $Ti_2(Ni,Au)$ phase, an arc-melted button was made, Table 5-1. The microstructure was quite interesting in both the as-cast and 550°C aged cases, Figures 5-1 and 5-2, respectively. Based on the SEM-EDS results, there appeared to be two main phases, Ti_3Au and Ti-Ni-Au B2. Also, within the B2 phase there were dark Ti-rich platelets, which exhibited a chemistry similar to the platelets found in the aged **Au25** samples. Ageing promoted the growth of the dark platelets within the B2 region. XRD data matched well with the three proposed phases, using Ti_2Pd as a reference for $Ti_2(Ni,Au)$, Figure 5-3. Further TEM analysis is underway to clarify the crystallography of each of the phases.

6.3 Au 4:3 Alloy

In the same manner, an arc-melted button of the $(Au,Ni)_4Ti_3$ stoichiometry was made, Table 5-2. Interestingly, the microstructure also contained two main phases based on SEM-EDS, $(Au,Ni)_2Ti$ and Ti-Ni-Au B2, Figures 5-4 and 5-5. There were also bright platelets within the B2 phase that had a chemistry quite similar to the $(Au,Ni)_4Ti_3$ type found in the aged **Au25** samples. Ageing at 550°C promoted the growth and coarsening of the bright platelet phase within the B2 region. XRD data was then matched with peaks associated with Au_2Ti , B2 phase, and peaks thought to associate with $(Au,Ni)_4Ti_3$. It is interesting to note that the reference peaks matched the experimental spectra quite well. It is hypothesized that these bright platelets are analogous to

the $(\text{Au,Ni})_4\text{Ti}_3$ type found in the aged **Au25** alloy. However, further examination via TEM is underway to determine the crystallography of the proposed phases.

CHAPTER 7: CONCLUSIONS AND FUTURE WORK

Within this study, $\text{Ti}_{49}\text{Ni}_{26}\text{Au}_{25}$ (**Au25**) was heat treated and characterized via SEM, EDS, Vickers Hardness Tests, EMP-WDS, TEM, XRD, 3DAP, and DSC. The following conclusions were based on the culmination of experimental results:

1. $\text{Ti}_4(\text{Ni,Au})_2\text{O}$ impurities were found in each sample via SEM.
2. The as-cast **Au25** composition was verified via EPMA-WDS and results indicated less than 1 percent variance in comparison to target values. The as-cast specimen was also examined via BSE imaging, which revealed a matrix rich in bright alternating platelets. These platelets are hypothesized to be related to the Ni_4Ti_3 type precipitation found in Ni-rich Ti-Ni alloys.
3. Solution annealing of the **Au25** alloy at 1050°C for three hours was shown to promote a single B2 phase via SEM and XRD. However, TEM SADPs indicated that a small volume fraction of precipitation was still present due to additional spots not associated with the B2 matrix.
4. Further ageing of the solution annealed **Au25** alloy at 400°C and 550°C resulted in an increase in Vickers hardness. Peak hardness values were quite high and occurred at different times for the 400°C and 550°C aged specimens, 48 hr and 96 hr, respectively. However, it is assumed that the growth kinetics at 400°C are too slow to achieve true peak hardness. BSE imaging of the 400°C specimens did not reveal significant microstructural change. However, BSE imaging of the 550°C specimens

revealed the growth of a fine scale microstructure consisting of alternating dark plates and a complex, nano-scale precipitation product.

5. TEM BF and SADPs of the 400°C aged **Au25** samples revealed the presence of two different phases. STEM-HAADF imaging qualitatively suggested that the finer, nano-scale precipitation was (Au,Ni)-rich and the large platelets were Ti-rich. The precipitation in the SADPs was ultimately identified as $Ti_2(Ni,Au)$ with a tetragonal $I4/mmm$ symmetry and $(Au,Ni)_4Ti_3$ with symmetry similar to a $D1_a$ structure and tetragonal $I4/m$ symmetry. Simulated electron diffraction patterns were fitted to experimental results and the following orientation relationships were obtained:

$$[100]_{B2} \parallel [100]_{Ti_2(Ni,Au)} \text{ with } (001)_{B2} \parallel (001)_{Ti_2(Ni,Au)}$$

$$[100]_{B2} \parallel [010]_{Ti_2(Ni,Au)} \text{ with } (001)_{B2} \parallel (100)_{Ti_2(Ni,Au)}$$

$$[001]_{D1a} \parallel [100]_{B2} \text{ with } (310)_{D1a} \parallel (011)_{B2}$$

$$[00\bar{1}]_{D1a} \parallel [100]_{B2} \text{ with } (310)_{D1a} \parallel (011)_{B2}$$

6. STEM-HAADF imaging of the 550°C aged samples revealed a coarsened version of the 400°C microstructure with dark and bright alternating platelets. TEM-EDS of both phases verified the proposed $Ti_2(Ni,Au)$ and $(Au,Ni)_4Ti_3$ type stoichiometry. SADPs from two zones of a $Ti_2(Ni,Au)$ platelet were fitted to simulated Ti_2Ag ($I4/mmm$) patterns and the theoretical and experimental angles between the zone axes were calculated. It was found that the difference was less than a degree and can be attributed to a change in the c/a ratio of the tetragonal unit cell.
7. XRD spectra from the 400°C and 550°C aged samples were identified with reference patterns from Ti_2Pd and a B2 phase. Ti_2Pd was used since it exhibits the same stoichiometry and symmetry as $Ti_2(Ni,Au)$. Then, since a reference pattern for

- (Au,Ni)₄Ti₃ with similar stoichiometry and symmetry was not found, it was proposed that all other unidentified peaks correlated to the tetragonal (Au,Ni)₄Ti₃ type precipitation. However, it is important to note that other I4/m structures with different chemistries did have peaks in the same regions, such as Au₄Ti.
8. 3DAP results of the 400°C aged specimens verified the presence of two precipitate types. The first type was identified using a Ti-isosurface analysis. The composition and morphology was consistent with TEM results of the (Au,Ni)₄Ti₃ phase. The second precipitate type was identified using a Ni-isosurface analysis. Its composition seemed to vary in Ti and Ni concentration in comparison to TEM-EDS results of the 550°C specimens. However, the crystallography of the Ti-rich phase was consistent between the two temperatures. Therefore, it is plausible to suggest that this metastable phase may exhibit a multi-stage compositional change during ageing. Further atom probe tomography on the 550°C aged specimens is needed to justify this claim.
 9. DSC of the as-cast and furnace cooled **Au25** specimens revealed evident transformations with martensite start temperatures of ~ 135°C and 160°C, respectively. This increase in transformation temperature is believed to have occurred due to the coarsening of the (Au,Ni)₄Ti₃ phase in the furnace cooled sample, which ultimately increases the concentration of Ti in the matrix. Interestingly, no transformations were found in any of the **Au25** aged samples tested. It is hypothesized that this is due to the addition of Ti-rich precipitation, which depletes the matrix of Ti toward an equiatomic or Ni-rich regime, thus stabilizing the high temperature austenite phase and pinning the martensite from forming upon cooling.

However, the precipitate volume fraction and equilibrium spacing may also account for this phenomenon. Further ageing coupled with DSC is needed to exploit this claim.

In an attempt to further characterize the precipitation behavior in the **Au25** alloy, buttons of the $(\text{Au,Ni})_4\text{Ti}_3$ and $\text{Ti}_2(\text{Ni,Au})$ type phases were arc-melted. The as-cast and 550°C aged specimens were examined via SEM and XRD. The following conclusions were based on the culmination of experimental results:

1. The microstructure of the as-cast $\text{Ti}_2(\text{Ni,Au})$ alloy consisted of two main phases. SEM-EDS results indicate a Ti_3Au region and a Ti-Ni-Au B2 region. Within the B2 region, there were also dark Ti-rich platelets with a stoichiometry similar to $\text{Ti}_2(\text{Ni,Au})$. Ageing at 550°C promoted the growth of the dark platelets. XRD data correlated well when referenced with Ti_3Au , a B2 phase, and Ti_2Pd (I4/mmm). This suggests that the platelets may be analogous to the Ti-rich phase found in the aged **Au25** samples.
2. The microstructure of the as-cast $(\text{Au,Ni})_4\text{Ti}_3$ alloy also consisted of two main phases. SEM-EDS results revealed a $(\text{Au,Ni})_2\text{Ti}$ region and a Ti-Ni-Au B2 region. There were also bright platelets present in the B2 phase with a composition consistent with the proposed $(\text{Au,Ni})_4\text{Ti}_3$ type. Ageing at 550°C promoted the growth and coarsening of the bright platelet phase within the B2 region. XRD data was then correlated with Au_2Ti , a B2 phase, and the peaks thought to associate with $(\text{Au,Ni})_4\text{Ti}_3$. It is interesting to note that the reference peaks matched the experimental spectra quite well. It is hypothesized that these bright platelets are analogous to the $(\text{Au,Ni})_4\text{Ti}_3$ type found in the aged **Au25** alloy.

There is much future work to be done in order to fully understand the Ti-Ni-Au system. Specific to this project, 3DAP needs to be done on the 550°C aged **Au25** specimens to examine the potential compositional variance of the Ti-rich platelets. This would determine whether the composition varies slightly from the proposed $\text{Ti}_2(\text{Ni,Au})$ stoichiometry or if the precipitation undergoes a multi-stage compositional change during ageing. It would also address the discrepancy of the 3DAP 400°C results in comparison to the TEM-EDS 550°C results regarding the Ti-rich platelet composition.

The crystallography of the $(\text{Au,Ni})_4\text{Ti}_3$ also needs further examination. Future TEM work on the furnace cooled sample is underway, since the large coarsened platelets in its microstructure are thought to be analogous to $(\text{Au,Ni})_4\text{Ti}_3$. This would give further clarification for indexing the $(\text{Au,Ni})_4\text{Ti}_3$ phase in experimental XRD data. Furthermore, TEM analysis of the precipitate button microstructures is also underway. Such results may provide a better understanding of the precipitate morphology and crystallography.

Lastly, follow up studies on ageing versus martensitic transformation temperature needs to be done. Ageing should to be taken out to long periods of time to exploit the idea of equilibrium precipitate spacing in correlation to the pinning of martensite. Although it is hypothesized that the Ti-rich precipitation in the **Au25** alloy inhibits martensite, it is possible that the precipitation is just too closely packed in the specimens tested in the DSC.

References

- [1] J. Van Humbeeck, "Non-medical applications of shape memory alloys," *Materials Science and Engineering: A* 273–275 (1999) 134-148.
- [2] E. P. Ryklina, I. Y. Khmelevskaya, S. D. Prokoshkin, K. E. Inaekyan and R. V. Ipatkin, "Effects of strain aging on two-way shape memory effect in a nickel–titanium alloy for medical application," *Materials Science and Engineering: A* 438–440 (2006) 1093-1096.
- [3] J. Ma, I. Karaman and R. D. Noebe, "High temperature shape memory alloys," *International Materials Reviews* 55 (2010) 257-315.
- [4] K. Otsuka and X. Ren, "Physical metallurgy of Ti–Ni-based shape memory alloys," *Progress in Materials Science* 50 (2005) 511-678.
- [5] G. A. Hudish, Characterization of High Temperature Shape Memory Alloys in The Ni-Ti-Pt Ternary System, M.S., Colorado School of Mines, Golden, Colorado, 2012.
- [6] W. Cai, X. L. Meng and L. C. Zhao, "Recent development of TiNi-based shape memory alloys," *Current Opinion in Solid State and Materials Science* 9 (2005) 296-302.
- [7] K. Otsuka and X. Ren, "Recent developments in the research of shape memory alloys," *Intermetallics* 7 (1999) 511-528.
- [8] T. Quackenbush and J. Robert Mckillip, "Selected Applications of Aero propulsion Actuation and Shape Control Devices Using HTSMAs," *Metall and Mat Trans A* (2011).
- [9] K. H. Eckelmeyer, "The effect of alloying on the shape memory phenomenon in nitinol," *Scripta Metallurgica* 10 (1976) 667-672.
- [10] G. S. Firstov, J. Van Humbeeck and Y. N. Koval, "High-temperature shape memory alloys: Some recent developments," *Materials Science and Engineering: A* 378 (2004) 2-10.
- [11] J. Van Humbeeck, "Shape memory alloys with high transformation temperatures," *Materials Research Bulletin* 47 (2012) 2966-2968.
- [12] M. Zarinejad, Y. Liu and Y. Tong, "Transformation temperature changes due to second phase precipitation in NiTi-based shape memory alloys," *Intermetallics* 17 (2009) 914-919.

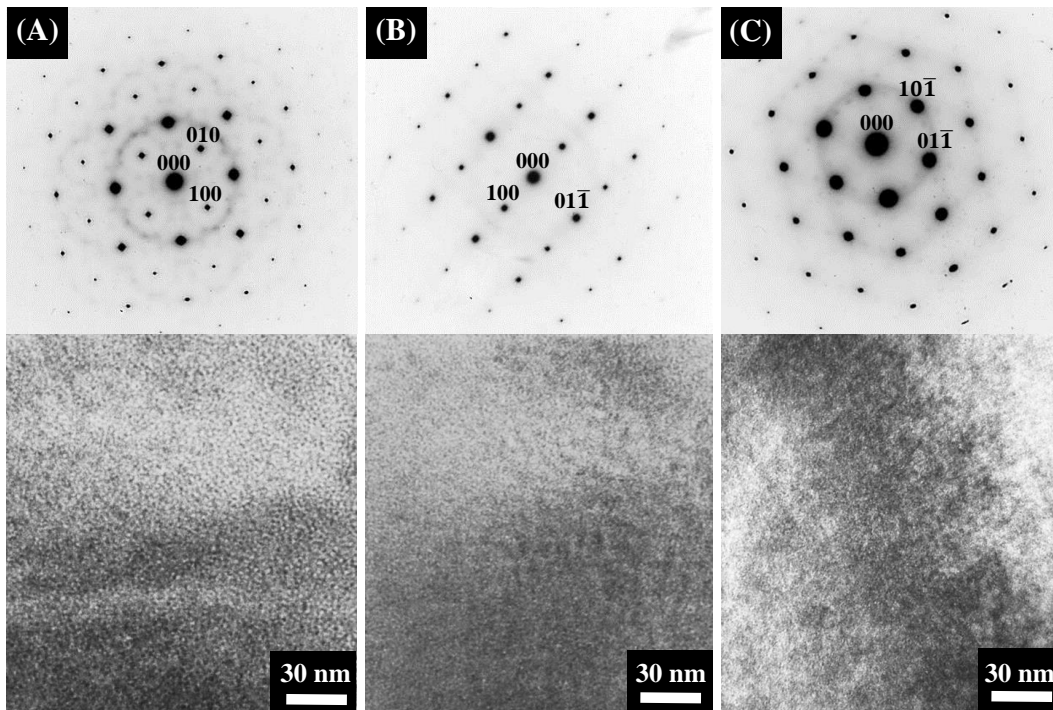
- [13] C. Declairieux, A. Denquin, P. Ochin, R. Portier and P. Vermaut, "On the potential of Ti₅₀Au₅₀ compound as a high temperature shape memory alloy," *Intermetallics* 19 (2011) 1461-1465.
- [14] H. C. Donkersloot and J. H. N. Van Vucht, "Martensitic transformations in gold-titanium, palladium-titanium and platinum-titanium alloys near the equiatomic composition," *Journal of the Less Common Metals* 20 (1970) 83-91.
- [15] W. J. Buehler, J. W. Gilfrich and R. C. Wiley, *Journal of Applied Physics* 34 (1963) 1473.
- [16] K. Otsuka and C. M. Wayman, eds., Shape Memory Materials (Cambridge University Press, New York, 1998).
- [17] K. Otsuka and K. Shimizu, "On the crystallographic reversibility of martensitic transformations," *Scripta Metallurgica* 11 (1977) 757-760.
- [18] Noebe et. al., Precipitation Hardenable High Temperature Shape Memory Alloy, US Patent Number US 7,749,341 B2, (2010).
- [19] G. Bozzolo, H. O. Mosca and R. D. Noebe, "Phase structure and site preference behavior of ternary alloying additions to PdTi and PtTi shape-memory alloys," *Intermetallics* 15 (2007) 901-911.
- [20] G. Bozzolo, H. O. Mosca and R. D. Noebe, "Site preference of ternary alloying additions to AuTi," *Journal of Alloys and Compounds* 425 (2006) 239-244.
- [21] Y. Gao, N. Zhou, F. Yang, Y. Cui, L. Kovarik, N. Hatcher, R. Noebe, M. J. Mills and Y. Wang, "P-phase precipitation and its effect on martensitic transformation in (Ni,Pt)Ti shape memory alloys," *Acta Materialia* 60 (2012) 1514-1527.
- [22] L. Kovarik, F. Yang, A. Garg, D. Diercks, M. Kaufman, R. D. Noebe and M. J. Mills, "Structural analysis of a new precipitate phase in high-temperature TiNiPt shape memory alloys," *Acta Materialia* 58 (2010) 4660-4673.
- [23] F. Yang, L. Kovarik, P. J. Phillips, R. D. Noebe and M. J. Mills, "Characterization of precipitate phases in a Ti-Ni-Pd alloy," *Scripta Materialia* 67 (2012) 145-148.
- [24] V. P. Sivokha and V. N. Khachin, "Martensitic Transformations and The Shape Memory Effect in Alloys of the TiNi-TiAu System," *Physics of Metals and Metallography* 62 (1985) 108-115.
- [25] B. Predel, "Au-Ti (Gold-Titanium)," edited by O. Madelung.
- [26] S. K. Wu and C. M. Wayman, "Martensitic transformations and the shape memory effect in Ti₅₀Ni₁₀Au₄₀ and Ti₅₀Au₅₀ alloys," *Metallography* 20 (1987) 359-376.

- [27] D. Tomus and H. P. Ng, "In situ lift-out dedicated techniques using FIB–SEM system for TEM specimen preparation," *Micron* 44 (2013) 115-119.
- [28] FEI-Company, ES Vision, (2004).
- [29] D. Palmer and M. Conley, CrystalMaker for Windows, (2010).
- [30] D. Palmer and M. Conley, SingleCrystal for Windows, (2010).
- [31] K. Thompson, D. Lawrence, D. J. Larson, J. D. Olson, T. F. Kelly and B. Gorman, "In situ site-specific specimen preparation for atom probe tomography," *Ultramicroscopy* 107 (2007) 131-139.
- [32] Cameca-Instruments-Inc, IVAS, (2012).
- [33] M. Nishida and C. M. Wayman, "Electron microscopy studies of precipitation processes in near-equiatomic TiNi shape memory alloys," *Materials Science and Engineering* 93 (1987) 191-203.
- [34] D. B. Williams and C. B. Carter, Transmission Electron Microscopy Part 2: Diffraction, Second edition (Springer, New York, 2009).
- [35] P. Schlossmacher, "Microstructural investigation of a TiNiPd shape memory thin film," *Materials Letters* 31 (1997) 119-125.
- [36] X. D. Han, R. Wang, Z. Zhang and D. Z. Yang, "A new precipitate phase in a TiNiHf high temperature shape memory alloy," *Acta Materialia* 46 (1998) 273-281.
- [37] J. L. Murray, *Bull. Alloy Phase Diagrams* 4 (1983) 278.
- [38] J. L. Murray, *Binary Alloy Phase Diagrams* 1 (1986).
- [39] K. Schubert, *Z. Metallkde* 56 (1965) 197.
- [40] M. H. Mueller and H. W. Knott, *Trans. AIME* 227 (1963) 674.
- [41] P. A. Blenkinsop and R. E. Goosey, *Sci. Technol. Appl. Titanium, Proc. Intl. Conf.* (1970) 783.
- [42] V. N. Eremenko, Y. I. Buyanov and S. B. Prima, *Sov. Powder Metall.. Met. Ceram.* 6 (1966) 494.
- [43] E. Raub and E. Roschel, "Die Titan-Palladium-Legierungen," *Z. Metallkde* 59 (1968) 112-114.

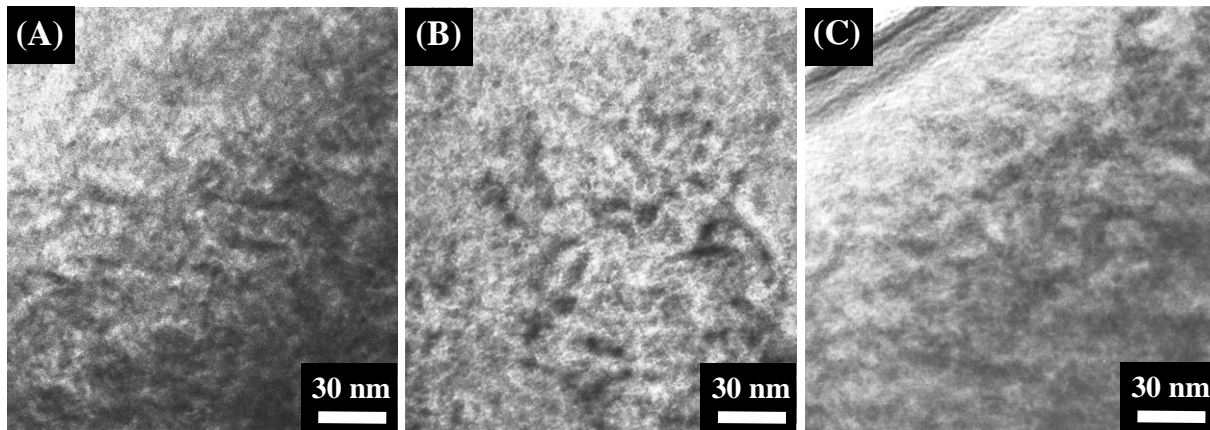
- [44] W. Tirry and D. Schryvers, "Quantitative determination of strain fields around Ni₄Ti₃ precipitates in NiTi," *Acta Materialia* 53 (2005) 1041-1049.
- [45] W. Tirry and D. Schryvers, "Linking a completely three-dimensional nanostrain to a structural transformation eigenstrain," *Nat Mater* 8 (2009) 752-757.
- [46] A. Ishida, M. Sato and K. Ogawa, "Microstructure and shape memory behavior of annealed Ti–36.8at.% Ni–11.6at.% Cu thin film," *Materials Science and Engineering: A* 481–482 (2008) 91-94.
- [47] R. Delville and D. Schryvers, "Transmission electron microscopy study of combined precipitation of Ti₂Ni(Pd) and Ti₂Pd(Ni) in a Ti₅₀Ni₃₀Pd₂₀ alloy," *Intermetallics* 18 (2010) 2353-2360.
- [48] T. Sawaguchi, M. Sato and A. Ishida, "Microstructure and shape memory behavior of Ti_{51.2}(Pd_{27.0}Ni_{21.8}) and Ti_{49.5}(Pd_{28.5}Ni_{22.0}) thin films," *Materials Science and Engineering: A* 332 (2002) 47-55.
- [49] D. P. van Heerden, T. Aboud, D. Shechtman and M. P. Shaw, "Precipitation in rapidly solidified Au-Ti alloys," *Materials Letters* 10 (1991) 425-430.
- [50] W. A. Soffa and D. E. Laughlin, "High-strength age hardening copper–titanium alloys: redivivus," *Progress in Materials Science* 49 (2004) 347-366.
- [51] M. Imran Khan, H. Y. Kim, T.-h. Nam and S. Miyazaki, "Formation of nanoscaled precipitates and their effects on the high-temperature shape-memory characteristics of a Ti₅₀Ni₁₅Pd₂₅Cu₁₀ alloy," *Acta Materialia* 60 (2012) 5900-5913.
- [52] H. Chen and H. Kubo, "Martensitic phase transformations and shape memory alloys," *Current Opinion in Solid State and Materials Science* 1 (1996) 349-354.
- [53] W. Cai, C. Tan, T. Shen and X. Tian, "First-principles study on alloying effect on martensitic transformation behavior of TiNi alloy," *Journal of Alloys and Compounds* 438 (2007) 30-33.

APPENDIX

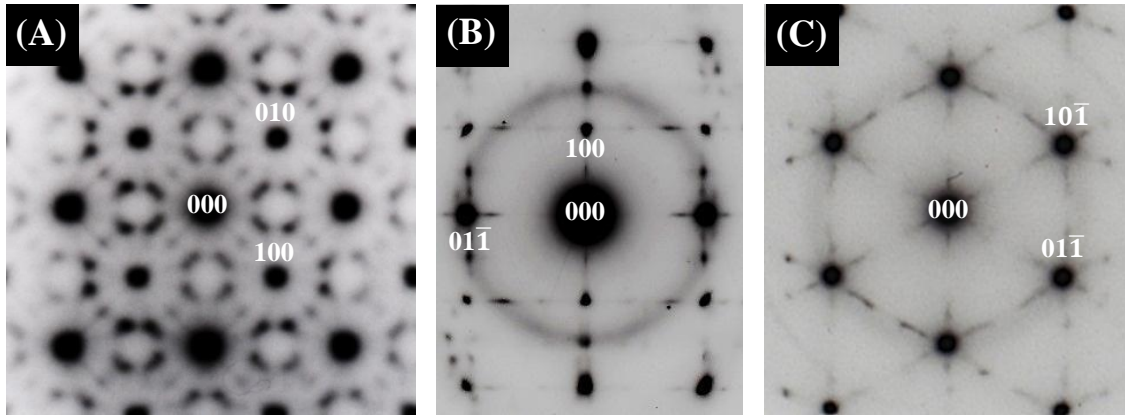
Additional TEM Work



Additional TEM bright field images and corresponding SADP of the 1050°C solution treated **Au25** alloy down the $\langle 100 \rangle_{B_2}$ (A), $\langle 110 \rangle_{B_2}$ (B), and $\langle 111 \rangle_{B_2}$ (C).



Additional TEM bright field images of the 48 hr 400°C **Au25** alloy down the $\langle 100 \rangle_{B_2}$ (A), $\langle 110 \rangle_{B_2}$ (B), and $\langle 111 \rangle_{B_2}$ (C).



Additional SADPs of the 168 hr 400°C **Au25** alloy down the $\langle 100 \rangle_{B2}$ (A), $\langle 110 \rangle_{B2}$ (B), and $\langle 111 \rangle_{B2}$ (C).

Status Primary QM: Indexed (I) Pressure/Temperature: Ambient Chemical Formula: Ti₂Pd
 Empirical Formula: Pd Ti₂ Weight %: Pd52.63 Ti47.37 Atomic %: Pd33.33 Ti66.67 ANX: NO₂
 Compound Name: Titanium Palladium

Radiation: CuKα1 : 1.5406Å d-Spacing: Calculated Intensity: Calculated I/Ic: 9.55

SYS: Tetragonal SPGR: I4/mmm (139)
 Author's Cell [AuthCell a: 3.090(10)Å AuthCell c: 10.054(80)Å AuthCell Vol: 96.00Å³ AuthCell Z: 2.00
 AuthCell MolVol: 48.00] Author's Cell Axial Ratio [c/a: 3.254] Dcalc: 6.995g/cm³ Dstruc: 6.99g/cm³
 SS/FOM: F(30) = 999.9(0.0001, 30)

Space Group: I4/mmm (139) Molecular Weight: 202.20
 Crystal Data [XtlCell a: 3.090Å XtlCell b: 3.090Å XtlCell c: 10.054Å XtlCell : 90.00° XtlCell : 90.00°
 XtlCell : 90.00° XtlCell Vol: 96.00Å³ XtlCell Z: 2.00]
 Crystal Data Axial Ratio [c/a: 3.254 a/b: 1.000 c/b: 3.254]
 Reduced Cell [RedCell a: 3.090Å RedCell b: 3.090Å RedCell c: 5.481Å RedCell : 106.37°
 RedCell : 106.37° RedCell : 90.00° RedCell Vol: 48.00Å³]

Crystal (Symmetry Allowed): Centrosymmetric

SG Symmetry Operators:

Seq	Operator										
1	x,y,z	4	x,y,-z	7	x,-y,z	10	y,-x,-z	13	y,x,z	16	y,x,-z
2	-x,-y,-z	5	-x,y,z	8	-x,-y,-z	11	y,-x,z	14	-y,-x,-z		
3	-x,-y,z	6	x,-y,-z	9	-y,x,z	12	-y,x,-z	15	-y,-x,z		

Atomic Coordinates:

Atom	Num	Wyckoff	Symmetry	x	y	z	SOF	IDP	AET
Pd	1	2a	4/mmm	0.0	0.0	0.0	1.0		14-b
Ti	2	4e	4mm	0.0	0.0	0.34	1.0		14-b

Pearson: tI6.00 Prototype Structure: Zr₂Cu Prototype Structure (Alpha Order): CuZr₂

LPF Prototype Structure: CuZr₂tI6.139 LPF Prototype Structure (Alpha Order): CuZr₂

Subfile(s): Primary Pattern, LPF Pattern, Metals & Alloys, Inorganic Entry Date: 01/05/2005

Last Modification Date: 01/13/2011 Former PDF's #: 01-072-2906, 03-065-2641, 03-065-8327

Cross-Ref PDF #'s: 00-018-0957 (Primary), 01-077-9426 (Alternate), 04-001-3128 (Alternate)

References:

Type Reference

Primary Reference Calculated from LPF using POWD-12+.

Structure "A Family of Intermediate Phases Having the Si₂Mo-Type Structure". Nevitt M.V., Downey J.W. Trans. Met. Soc. AIME 224, 194 (1962).

Database Comments:

ANX: NO₂. LPF Collection Code: 527104. Sample Preparation: STARTING MATERIALS:Ti,Pd. Compound Preparation: arc-melted. Sample annealed at 1173 K for 72 h in evacuated tube, water-quenched. Temperature of Data Collection: 293 K. Minor Warning: No R factor reported/abstracted. Unit Cell Data Source: Powder Diffraction.

d-Spacings (43) - 04-004-2395 (Fixed Slit Intensity) - Cu K1 1.54056Å

2	d(Å)	I	h	k	l	*	2	d(Å)	I	h	k	l	*	2	d(Å)	I	h	k	l	*
17.6281	5.027000	246	0	0	2		74.1615	1.277540	190	2	1	3		106.8450	0.959191	8	3	1	2	
30.2338	2.953650	180	1	0	1		75.6010	1.256750	5	0	0	8		114.3325	0.916730	6	3	0	5	
35.6917	2.513500	20	0	0	4		85.1179	1.138880	21	2	1	5		114.6380	0.915159	26	2	2	6	
39.6405	2.271740	999	1	0	3		85.3971	1.135870	56	2	0	6		114.9934	0.913346	2	1	1	10	
41.2852	2.184960	437	1	1	0		89.6712	1.092480	24	2	2	0		115.5093	0.910743	4	3	1	4	
45.2128	2.003860	73	1	1	2		89.9937	1.089400	11	1	1	8		123.0083	0.876462	7	1	0	11	
54.3924	1.685370	52	1	0	5		92.3624	1.067560	6	2	2	2		124.9116	0.868749	46	2	1	9	
54.7335	1.675670	77	0	0	6		94.3122	1.050560	38	1	0	9		128.8596	0.853915	5	3	2	1	
55.6946	1.649010	18	1	1	4		97.4856	1.024640	4	3	0	1		131.7167	0.844108	45	3	1	6	
59.8100	1.545000	113	2	0	0		100.0175	1.005400	1	0	0	10		133.6688	0.837833	5	0	0	12	
62.8766	1.476820	23	2	0	2		100.4918	1.001930	3	2	2	4		133.9300	0.837019	2	3	0	7	
68.4786	1.369020	24	2	1	1		101.3410	0.995819	4	2	1	7		136.1645	0.830293	45	3	2	3	
70.8035	1.329660	111	1	1	6		102.9557	0.984550	33	3	0	3		138.2096	0.824504	5	2	2	8	
71.6366	1.316230	8	2	0	4		104.0534	0.977144	32	3	1	0								
72.5134	1.302460	5	1	0	7		104.3863	0.974937	8	2	0	8								

ICDD data card for referenced Ti₂Pd phase.